Fermilab

FERMILAB-THESIS-1999-08

MEASUREMENT OF THE BOTTOM QUARK PRODUCTION CROSS SECTION IN PROTON-ANTIPROTON COLLISIONS AT A CENTER-OF-MASS ENERGY 630 GeV USING MUONS WITH ASSOCIATED JETS

by

Kevin Patrick Davis

A Dissertation Submitted to the Faculty of the

DEPARTMENT OF PHYSICS

In Partial Fulfillment of the requirements
For the Degree of

DOCTOR OF PHILOSOPHY

In the Graduate College

THE UNIVERSITY OF ARIZONA

1 9 9 9

STATEMENT BY AUTHOR

This dissertation has been submitted in partial fulfillment of requirements for an advanced degree at The University of Arizona and is deposited in the University Library to be made available to borrowers under rules of the Library.

Brief quotations from this dissertation are allowable without special permission, provided that accurate acknowledgement of source is made. Requests for permission for extended quotation from or reproduction of this manuscript in whole or in part may be granted by the head of the major department or the Dean of the Graduate College when in his or her judgement the proposed use of the material is in the interests of scholarship. In all other instances, however, permission must be obtained from the author.

SIGNED: _____

ACKNOWLEDGEMENTS

When I began writing this monolithic document, I believed wholeheartedly that the Acknowledgements section was self-serving and useful only for easily inserting phrases like "duck-billed platypus" to win friendly wagers made at the Users Center. Now, nearing completion, I realize that this section allows me to give credit and thanks to those who most deserve them, and to truly mean it.

First and foremost, I thank my advisor, Dr. Ken Johns, for giving me this opportunity and helping me see it through until the end. I would also like to thank Arizona postdocs Dr. Dave Fein and The Nefarious Dr. Nang for sitting in as advisors-by-proxy when Ken was away. Thank you to all the members of the B-physics group at DØ who always knew where to poke the holes, especially F. Stichelbaut, A. Zieminski, A. Maciel, R. Jesik, D. Zieminska, and D. Denisov. In addition, I am grateful to all the former Arizona students and postdocs, Dave, Ajay, E. J., Alex, and Rama, for helping me get started at Fermilab. Thanks also to Levan, Rob, and Pete, who had occasion to suffer my occasional PAW-inspired profanity in the trailers. The whole crew at Arizona really helped me grow professionally, and for every bit of their effort, I am grateful.

I would also like to thank those who supported me throughout my life and helped me grow personally as well as professionally. I wouldn't be the person I am today if I'd never played in Death Squad and Lost Dog with Nigel and Hub. I'm a better person because of their friendship. Thanks to those who have managed to live with me and become great friends in the process: Woody, DeSoto, and Chiss. Thanks to my friends at Arizona and BGSU, too numerous to mention here. Thanks also to those who have made Fermilab a more interesting place: Ree-otch, Sam, Cap'n Yuri, Flory, Roo, and Lin, and the entire FSU house. Kudos also go to Megaman Johnny, who earned his title by going above and beyond to help me put the finishing touches on this document. A special thanks to N for keeping me calm, remaining by my side, and loving me through all this.

Lastly, thanks to my parents, Pat and Pat, who started me on this path so long ago. Thank you for teaching me that I can do anything I set my mind to and that attitude is everything. Special thanks to my sister, Shannon, for never doubting and always being there as a friend.

It is to all of you that I owe this honor. Thank you.

To all y'all,

Yee-haw!

TABLE OF CONTENTS

LIST OF FIGURES

LIST OF TABLES

ABSTRACT

We have measured the b-quark production cross section for $|y| < 1$ using a sample of muons with associated jets collected with the DØ detector in $p\overline{p}$ collisions at $\sqrt{s} = 630$ GeV at the Fermilab Tevatron. The measured b-quark cross section is consistent in shape with $\mathcal{O}(\alpha_s^3)$ QCD predictions, but exceeds them in normalization by roughly a factor of 2.5.

CHAPTER 1

INTRODUCTION TO HIGH ENERGY PHYSICS

High energy physics (HEP), or elementary particle physics (EPP), is the study of the elementary particles in nature and their interactions. At the atomic level, matter is divisible into protons, neutrons, and electrons; quarks are currently considered to be the fundamental, or indivisible, constituents of protons and neutrons. The six known quarks are called, in order of increasing mass, up, down, strange, charm, bottom, and top.

The two heaviest quarks, bottom and top, were discovered at Fermilab relatively recently (1977 and 1995 respectively). They are of special interest, because heavy quark production theories can be treated perturbatively, and the cross sections can be expressed as a convergent power series in the strong coupling constant.

The bottom quark is experimentally identifiable and has a relatively large cross section at Tevatron energies. Measurements of bottom quark production test the current description of QCD, as well as providing insight into other heavy flavor production processes, such as charm and top.

The bottom quark production cross section has been measured at Fermilab at $\sqrt{s} = 1.8$ TeV [1][2][3][4], and all measurements exceed theoretical predictions by approximately a factor of 2.5. In addition, the UA1 collaboration measured bottom quark production at $\sqrt{s} = 630$ GeV [5]. The UA1 measurement exhibited somewhat better agreement with the theoretical predictions available at the time.

This dissertation, which presents an independent measurement of bottom quark

production for a center-of-mass energy $\sqrt{s} = 630$ GeV, is arranged in nine chapters and three appendices. The remainder of Chapter 1 provides an introduction to high energy physics theory, including a brief discussion of QED and QCD, as well as outstanding problems with the theory. Chapter 2 deals with the more specific topic of heavy quark production within the framework of QCD. Monte Carlo simulation of the theoretical predictions are discussed in Chapter 3. The DØ detector is described in detail in Chapter 4. Chapter 5 provides a description of the data sample acquisition and selection, while Chapter 6 discusses the techniques used to separate signal from background in the data sample. Chapter 7 discusses the unsmearing of the muon momentum spectrum. Chapter 8 presents final measured cross sections, and Chapter 9 provides a brief discussion of the results, including a comparison to previous measurements.

The three appendices include parenthetical information not discussed in the chapters. Appendix A provides a description of the coordinate systems and conventions used in the analysis. Appendix B provides a discussion of the error analysis techniques that are used to estimate the uncertainty on the measurement. The locations of the various pieces code used to perform the analysis are listed in Appendix C.

1.1 High Energy Physics, Historically

Particle physics is often said to have begun in ancient Greece. Democritus, a student of Leucippus, was one of the earliest philosophers to suggest that if matter is successively divided into smaller and smaller pieces, eventually a piece will exist that can not be subdivided. This smallest indivisible piece of matter was called *atomos* by

Democritus, a word from which modern man derived the modern term *atom*.

Until J. J. Thomson discovered the electron, demonstrating that the atom was indeed not fundamental, particle physics remained largely the same as it was in 400 B. C. Since Thomson's discovery, however, particle physics has developed at an astonishing rate.

When P. A. M. Dirac's relativistic wave equation was unsuccessful at describing the magnetic properties of the proton, and all attempts at building an electron-proton model of the atom failed, it became clear that the explorations of particle physics had not come to an end. In 1932, the neutron and the positron (anti-electron) were discovered by Chadwick and Anderson respectively, adding to the confusion.

Shortly thereafter, Hideki Yukawa proposed a new massive particle, the meson. When the muon was discovered in cosmic rays in 1932, it was mistaken for Yukawa's meson. This idea was discarded in the late 40s when Cecil Powell found the pion.

High energy electron experiments performed by Richard Hofstadter suggested that nucleons, the collective term for protons and neutrons, had internal structure that electrons did not have. This suggestion led to Murray Gell-Mann's hypothesis, called the *Eight-fold Way* [6]. The Eight-fold Way introduced *quarks*, fractionally charged point-like particles that could bind together into baryons (three-quark bound states) and mesons (two-quark bound states). The properties of the proton and neutron were explained by two of Gell-Mann's quarks, the up (u) and the down (d). The postulation of quarks came just in time to explain the "zoo" of particles that were being found at the time.

To probe more and more deeply into the substructure of matter, particle physicists had to use accelerators of increasing energy. Elementary particle physics developed

$\begin{pmatrix} \nu_e \\ e \end{pmatrix}$	$\begin{pmatrix} \nu_\mu \\ \mu \end{pmatrix}$	$\begin{pmatrix} \nu_\tau \\ \tau \end{pmatrix}$	Leptons
$\begin{pmatrix} u \\ d \end{pmatrix}$	$\begin{pmatrix} c \\ s \end{pmatrix}$	$\begin{pmatrix} t \\ b \end{pmatrix}$	Quarks

Table 1.1: The three generations of quarks and leptons

into high energy physics, each discovery bringing about more unanswered questions. The sections that follow detail our present knowledge.

1.2 Leptons, Quarks, and the Fundamental Forces

It is currently believed that the whole of nature consists of twelve fermions (half-integral spin), their antiparticles (opposite charge), and the gauge bosons (integral spin) that mediate the interactions between them. The twelve fermions are divided into six leptons, which experience only the electromagnetic, weak, and gravitational forces, and six quarks, which can interact additionally via the strong interaction. Quarks and leptons are further subdivided into three generations (Table 1.1). Each new generation is identical in charge to its predecessor on the left; but the masses differ (increasing mass to the right).

1.2.1 Leptons and Quarks

The charged leptons (e, μ, and τ) were the first fermions to be discovered because observations of their interactions are not obscured by the strong force. The muon discovery paper was published in 1937 [7], and the discovery of the tau, for which Martin Perl received the Nobel Prize in 1995, was announced in 1975 [8].

Each charged lepton has an associated neutrino that, until the summer of 1998,

Lepton	**Electric Charge**	**Mass (MeV/c^2)**	**Lifetime (s)**
e	-1	.511	stable
μ	-1	106	2.2×10^{-6}
τ	-1	1777	291×10^{-15}
ν_e	0	< 15 eV/$\mathbf{c}^2$	stable
ν_μ	0	< 0.19	stable
ν_τ	0	< 18	stable

Table 1.2: The properties of the leptons.

when SuperKamiokande presented evidence of a nonzero neutrino mass difference between ν_μ and ν_τ, was assumed to be massless. The electron neutrino was postulated to describe the continuous energy spectrum in neutron β-decay by Enrico Fermi in 1934 [9]. Evidence for the muon neutrino and the tau neutrino was subsequently discovered, although the tau neutrino has yet to be directly observed. SuperKamiokande presented exciting evidence of a nonzero neutrino mass difference between ν_μ and ν_τ, due to the observation of neutrino oscillations in atmospheric neutrinos [10]. Some fundamental properties of the leptons are given in Table 1.2. Charges are given in units of proton charge.

Quarks, the remaining fundamental fermions, were far more difficult to discover, as they interact via the strong nuclear force. The strong force binds quarks into hadronic matter; as a consequence, quarks are not observable as free particles. The three lightest quarks, up (u), down (d), and strange (s), were proposed in 1964 by Gell-Mann and Zweig to explain the properties of the hadrons that had been observed. The discovery of the J/ψ ($c\bar{c}$ bound states, also called charmonium) and the Υ ($b\bar{b}$ bound states, also called bottomonium) mesons provided evidence for the existence of three quark doublets. The final known member of the quark family, the top quark, was discovered at Fermi National Accelerator Laboratory in 1995 [11][12]. Some

Quarks	Name	Electric Charge	Mass
d	down	$-\frac{1}{3}$	5-15 (MeV/c^2)
u	up	$+\frac{2}{3}$	2-8 (MeV/c^2)
s	strange	$-\frac{1}{3}$	100-300 (MeV/c^2)
c	charm	$+\frac{2}{3}$	1.0-1.6 (GeV/c^2)
b	bottom	$-\frac{1}{3}$	4.1-4.5 (GeV/c^2)
t	top	$+\frac{2}{3}$	180 (GeV/c^2)

Table 1.3: Known properties of the quarks.

fundamental properties of the observed quarks are given in Table 1.3.

1.2.2 Fundamental Forces

The fundamental fermions experience interactions via four forces: the electromagnetic force, the weak nuclear force, the strong nuclear force, and gravitation. Each force is mediated by the exchange of a gauge boson between fermions. The electromagnetic interaction affects all charged fermions and is mediated by the exchange of photons. The strong interaction affects only quarks and is mediated by gluon exchange. The weak nuclear force is mediated by the massive W and Z bosons and affects all fermions. Gravitation, the weakest of the four fundamental forces, arises from the exchange of a spin 2 graviton and only mediates interactions between massive fermions. Properties of the four fundamental forces and their mediating gauge bosons are presented in Table 1.4. Masses are given in GeV/c^2.

1.2.3 Feynman Diagrams

Richard Feynman developed a system of graphically representing particle interactions that allowed physicists to not only visualize the interactions but perform difficult calculations in a straightforward manner. In Feynman diagrams, time increases to

Force	**Gauge Boson**				**Typical Coupling Strength**	**Fermions Affected**
	Name	Mass	Charge	Spin		
Strong	Gluon (g)	0	0	1	$\tilde{}1$	quarks
Electro−Magnetic	Photon (γ)	0	0	1	$\frac{1}{137}$	charged
Weak	$W^{\pm}$ Z	80 91	± 1 0	1 1	$\tilde{}10^{-5}$	all
Gravity	Graviton (G)	0	0	2	$\tilde{}10^{-38}$	massive

Table 1.4: The four fundamental forces of nature.

the right. The basic component lines of any Feynman diagram are shown in Figure 1.1. All fermions are denoted with a solid straight line, while the gauge bosons are denoted with a variety of lines. In some Feynman diagrams, the fermion lines use arrows to show the direction in time of the particle. Anti-fermions are drawn as fermions moving to the left.

As an example, Figure 1.1 depicts electron-positron annihilation. The electron and positron at the left annihilate into a photon, which then emits an electron-positron pair. This interaction is also known as "time-like Bhabha scattering."

Feynman diagrams not only give a visual presentation of a process, they also prove invaluable in calculations associated with that process. Knowledge of the forms of the propagators associated with the physical process (in Figure 1.1, the photon) and the nature of the interaction vertex, allows one to write down a simple form for many physical quantities (cross sections, lifetimes, etc.). For a more thorough introduction to Feynman diagrams, the interested reader is directed to consult an elementary particle physics text (e.g. [13]).

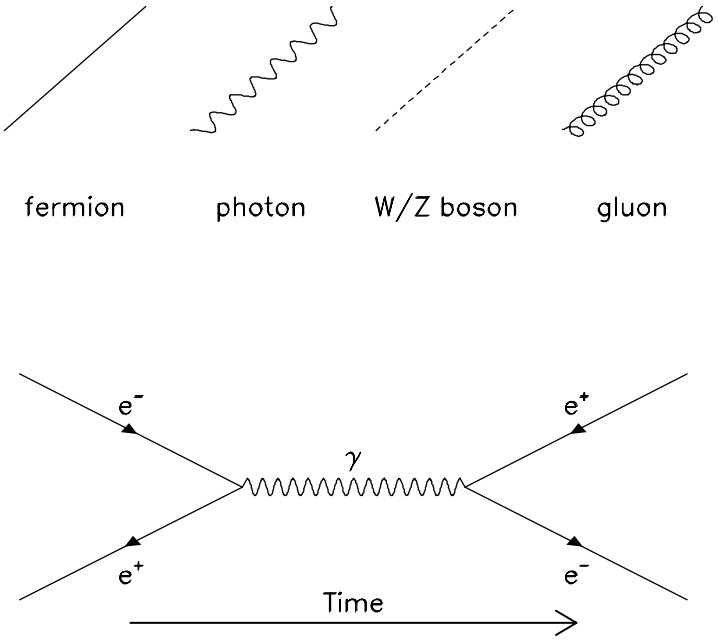

Figure 1.1: Representations of various particles in Feynman diagrams (top). Time-like Bhabha scattering is shown at bottom.

1.3 The Standard Model

The current theory of how the fundamental fermions interact is embodied in the Standard Model (SM). As a theory, the SM has enjoyed predictive power, accurately predicting cross sections, decay rates, and even the masses of the W and Z bosons. To date, no experiment has ever significantly contradicted the predictions of the SM.

The Standard Model can be understood as a union of *field theories*, each of which describes the way one of the four fundamental forces govern the behavior of particles. In a quantum field theory, particles are associated with fields, functions of space-time coordinates. Each field theory in the SM is required to be locally gauge invariant, implying that the Lagrangian description of the interaction is invariant under a local phase transformation. Requiring local invariance necessarily implies the existence of a gauge boson and its coupling to the fermions.

The Standard Model unifies the strong interaction, the weak interaction, and the electromagnetic interaction. In the SM, the electromagnetic and weak interactions may be unified under a single gauge group, but attempts to merge the electroweak (EW) gauge with the theory of strong interactions (quantum chromodynamics) have been unsuccessful. The unification of these gauge groups into a Grand Unified Theory (GUT) would eliminate many of the seemingly arbitrary parameters in the SM, which include particle masses and coupling strengths. Because no successful GUT has been developed, the electroweak and strong interactions are more conveniently considered separately.

1.3.1 Electroweak Theory

A fundamental part of the Standard Model, quantum electrodynamics (QED) is perhaps the most easily understood field theory. The Lagrangian that describes QED is invariant under local gauge transformations of the electron field $\psi(x)$ and the photon field $A_\mu(x)$ for all space time points x. These transformations are of the form

$$\psi(x) \rightarrow e^{ie\Lambda(x)}\psi(x) \tag{1.1}$$

$$A_\mu(x) \rightarrow A_\mu(x) + \partial_\mu\Lambda(x). \tag{1.2}$$

Here, $\Lambda(x)$ is arbitrary, and e is the familiar electron-photon coupling strength. The exact local gauge invariance of the Lagrangian requires a massless gauge boson. As a result of local gauge invariance, QED is also *renormalizable*, indicating that all unphysical infinities can be eliminated through a cancellation procedure.

The phase factor $e^{i\Lambda(x)}$ belongs to the symmetry group $U(1)$. $U(1)$ is an Abelian unitarity group in one dimension, because the generator of $U(1)$ commutes with itself. In general, however, the gauge groups in the SM are more complicated. Both the electroweak and QCD theories use non-Abelian groups, resulting in self-coupling gauge bosons.

Because the fundamental fermions are arranged in doublets, they can be described as a two-component field $\psi = (\psi_1, \psi_2)$, where the indices indicate a doublet from Table 1.1. A two-component field allows introduction of gauge transformations Λ, where Λ is a 2×2 hermitian matrix. This two dimensional matrix suggests an $SU(2)$ symmetry, where $SU(2)$ is the special unitarity group in two dimensions. $SU(2)$ transformations permit changing one member of the doublet through non-zero off-diagonal terms. Requiring local gauge invariance results in the introduction of three

massless gauge bosons.

Unifying the $SU(2)$ group with $U(1)$ results in another theory, $SU(2) \otimes U(1)$, the Glashow-Salam-Weinberg theory of electroweak interactions. This combined theory is designed to be invariant under two types of transformations, each of which is described by the coupling of a weak current to a vector boson:

- **Weak Isospin, T**, the generator of the $SU(2)_L$ group, and
- **Weak Hypercharge, Y**, the generator of the $U(1)$ group. The hypercharge is related to the isospin and electric charge by the relation

$$Q = T_3 + \frac{1}{2}Y, \tag{1.3}$$

  where T_3 is the third component of weak isospin.

For this group of transformations, only left-handed fermions may transform under both $SU(2)_L$ and $U(1)_Y$ (right-handed neutrinos have yet to be discovered). Right-handed fermions are limited to transformations under $U(1)$.

The local gauge invariance of $SU(2)_L \otimes U(1)_Y$ transformations requires the introduction of four massless gauge bosons – three W_μ for $SU(2)_L$, and one B_μ for $U(1)_Y$. The short range of the weak interaction, however, requires the existence of three massive bosons ($W^\pm, Z^0$). To reconcile this contradition, the Higgs mechanism [14] is employed.

The Higgs mechanism introduces four scalar fields φ_i into the electroweak Lagrangian. Conventionally, the fields are arranged into an isospin doublet with $Y = 1$:

$$\varphi = \begin{pmatrix} \varphi^+ \\ \varphi^0 \end{pmatrix} \tag{1.4}$$

with

$$\begin{aligned} \varphi^{+} &= \tfrac{1}{\sqrt{2}}\left(\varphi_1 + i\varphi_2\right) \\ \varphi^{\mathbf{0}} &= \tfrac{1}{\sqrt{2}}\left(\varphi_3 + i\varphi_4\right) \end{aligned} \quad . \tag{1.5}$$

Choosing the vacuum expectation value to be

$$\langle\varphi\rangle_{\mathbf{0}} = \frac{1}{\sqrt{2}} \begin{pmatrix} 0 \\ \\ v \end{pmatrix} \tag{1.6}$$

will spontaneously break the symmetry of $SU(2)_L \otimes U(1)_Y$, giving rise to the massive gauge bosons. Note that the choice of $\langle\varphi\rangle_{\mathbf{0}}$ will remain invariant under $U(1)$ transformations for electromagnetic charge, so the photon remains massless. The resulting bosons and their masses are given by

$$\begin{aligned} W_\mu^{\pm} &= \tfrac{1}{\sqrt{2}}\left(W_\mu^1 \mp i W_\mu^2\right) && M_W^2 = \left(\tfrac{g\nu}{2}\right)^2 \\ Z_\mu &= -B_\mu \sin\theta_W + W_\mu^3 \cos\theta_W && M_Z^2 = \left(\tfrac{M_W}{\cos\theta_W}\right)^2 \\ A_\mu &= B_\mu \cos\theta_W + W_\mu^3 \sin\theta_W && M_A^2 = 0, \end{aligned} \tag{1.7}$$

where θ_W is the weak mixing angle $\left(\sin^2\theta_W = 0.23\right)$.

The Higgs mechanism not only provides mass to the W and Z bosons while keeping the photon massless; it also introduces a massive scalar particle, the Higgs boson. In addition, the Higgs mechanism is required to generate particle masses in a gauge invariant way. The mass of the Higgs is one of the few experimentally unmeasured free parameters in the Standard Model.

1.3.2 Quantum Chromodynamics (QCD)

The third fundamental force included in the Standard Model is the strong nuclear force, which acts only on quarks. The equivalent to electromagnetic charge for the strong force is called *color*. Quarks can assume one of three colors, so any particular

quark can be described by a three-component field $\psi = (\psi\,(\text{red})\,, \psi\,(\text{green})\,, \psi\,(\text{blue}))$. The three-color nature of the quarks suggests an $SU(3)$ group, where each transformation can be described as a transformation under a 3×3 hermitian matrix. The gauge theory based on the $SU(3)$ color group is called quantum chromodynamics (QCD).

Local gauge invariance of the $SU(3)$ color group requires the introduction of eight massless gauge bosons. These mediators of the strong force are eight bi-colored *gluons*. Because QCD is a non-Abelian gauge theory, the gluons couple with each other in the same fashion as vector bosons in weak interactions.

Quarks and gluons have never been observed as free particles; they are confined to colorless bound states. As the distance between two bound quarks increases, the potential energy due to the color interaction becomes very large, attempting to keep the two quarks from separating. This increase in force with increasing distance is known as *infrared slavery*. As the distance between particles decreases, the quarks begin to act like free particles, a feature of QCD called *asymptotic freedom*.

If the potential energy becomes great enough, a new pair of quarks is created. For very energetic collisions, many of these pairs may be created, resulting in a shower of particles all moving in the same direction. Each particle, called a *hadron*, is required to be colorless, and the resulting hadronic shower is called a *jet*. The entire showering process is referred to as *hadronization*.

Two types of hadrons may appear in the final state jet: mesons and baryons. Mesons consist of quark-antiquark bound states, the colors of which must result in a colorless meson (allowed color combinations include $r\overline{r}, g\overline{g}, b\overline{b}$). Baryons exist as three-quark or three-antiquark bound states, the colors of which must also combine

to exhibit no net color ($rgb, \overline{rg}\overline{b}$).

The $SU(3)$ group representing the strong force can be combined with the transformation groups of the electromagnetic and weak forces. This unification of groups results in a gauge invariant theory ($SU(3) \otimes SU(2) \otimes U(1)$) known as the Standard Model.

1.4 Using the *b*-quark to Probe QCD

The bottom quark provides us with a quantitative test of heavy flavor perturbative QCD (pQCD). Quantitative tests are made possible because b-quarks are experimentally identifiable. Furthermore, expansions in pQCD are expressed in terms of α_s, the strong coupling constant. The coupling constant runs with m_Q, getting smaller with increasing quark mass, so perturbative expansions in α_s are more stable for the massive bottom quark.

Theoretical calculations are currently available to order $\mathcal{O}(\alpha_s^3)$ (next-to-leading order, or NLO) for the inclusive b-quark production cross section. The current effort to understand heavy flavor production was prompted by the disagreement between predictions and measurements of the b-quark cross section made by the DØ and CDF collaborations at $\sqrt{s} = 1.8$ TeV. Knowing the order to which pQCD is correct for a given process increases our understanding of the reliability of QCD and catalyzes theoretical efforts to improve it.

CHAPTER 2

THEORY OF HEAVY QUARK PRODUCTION

Heavy quarks are produced in hadron-hadron interactions during collisions of a parton from each hadron. The general expression for the heavy quark production cross section in collisions between two hadrons A and B is [15]

$$d\sigma_{H_1H_2} = \sum_{i,j} \int dx_1 dx_2 d\widehat{\sigma}_{ij}\left(x_1P_1, x_2P_2, k_1, k_2, m, \mu\right) F_i^1\left(x_1, \mu\right) F_j^1\left(x_2, \mu\right) \qquad (2.1)$$

where k_1 and k_2 are the momenta of the quark and antiquark, F_i^1 are the structure functions for incoming parton i in hadron 1, m is the mass of the heavy quark, μ is the renormalization and factorization scale, and $d\widehat{\sigma}_{ij}$ is the partonic cross section for $ij \to Q\overline{Q}X$ with a partonic center-of-mass energy $\widehat{s}$. The scattering process is shown graphically in Figure 2.1.

The terms of $d\sigma$ can not be computed analytically. The structure functions and partonic cross section must be expanded in a power series of the strong coupling constant α_s:

$$d\widehat{\sigma}_{ij}\left(\widehat{s}, m, \mu\right) = \alpha_s^2\left(\mu\right) f_{ij}^{(0)}\left(\widehat{s}, m^2\right) + \alpha_s^3\left(\mu\right) f_{ij}^{(1)}\left(\widehat{s}, m^2\right) + ... \qquad (2.2)$$

$$F_i^1\left(x_1, \mu\right) = g_i^{A,(0)}\left(x_1, \mu\right) + \alpha_s\left(\mu\right) g_i^{A,(1)}\left(x_1, \mu\right) + ... \qquad (2.3)$$

where f, g, and μ depend on the scheme used for factorization and renormalization. On the right side of the expression, (0) and (1) refer to the leading order (LO) and next-to-leading order (NLO) terms respectively.

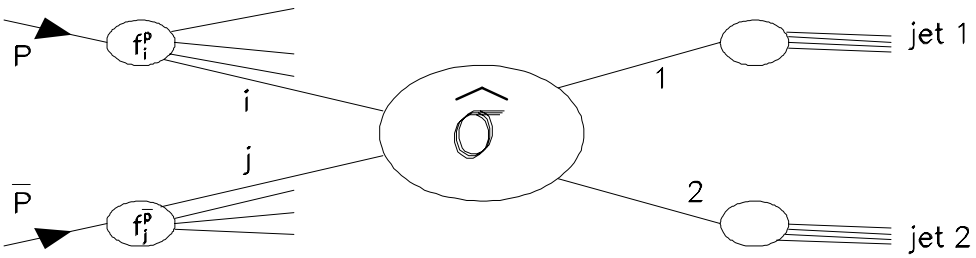

Figure 2.1: Leading order heavy quark production.

2.1 The Strong Coupling Constant

The strong coupling constant is not really a constant; it depends on the momentum transfer in the process of interest. This behavior is termed *running*. For calculations, the strong coupling constant is described at a fixed renormalization scale $\mu = Q_0$. This value is generally chosen to be evaluated at the mass of the heavy quark being produced to reflect the mass scale. The coupling's dependence on μ is determined by the renormalization group equation

$$\begin{aligned} \mu^2 \frac{\partial \alpha_s}{\partial \mu^2} &= \beta\left(\alpha_s\left(\mu\right)\right) \\ &= -b_0 \alpha_s^2\left(\mu\right) - b_1 \alpha_s^3\left(\mu\right) + \mathcal{O}\left(\alpha_s^4\left(\mu\right)\right) \end{aligned} \tag{2.4}$$

where

$$b_0 = \frac{11 n_c - 2 n_f}{12\pi} \tag{2.5}$$

and

$$b_1 = \frac{51 n_c - 19 n_f}{24\pi^2}. \tag{2.6}$$

In the expressions for the b coefficients, n_c is the number of colors in $SU\left(3\right)$ ($n_c = 3$), and n_f is the number of quark flavors with a mass below the renormalization scale.

Terms involving n_c correspond to 3-gluon vertex diagrams, while terms involving n_f correspond to quark loop diagrams. Solving 2.4 for leading order (terms of $\mathcal{O}(\alpha_s^3(\mu))$ and higher are neglected) yields the LO approximation for the running coupling constant:

$$\alpha_s(\mu) = \frac{\alpha_s(Q_0)}{1 + b_0 \alpha_s(Q_0) \ln\left(\frac{\mu^2}{Q_0^2}\right)}. \tag{2.7}$$

The running coupling constant should not be expected to depend on Q_0, so the expression for $\alpha_s(\mu)$ is generally rewritten in terms of the QCD mass scale, Λ, with Λ defined implicitly by

$$\ln \frac{\mu^2}{\Lambda^2} = -\int_{\alpha_s(\mu)}^{\infty} \frac{dx}{\beta(x)}. \tag{2.8}$$

Rewriting expression 2.7 results in

$$\alpha_s(\mu) = \frac{1}{b_0 \ln\left(\frac{\mu^2}{\Lambda^2}\right)}. \tag{2.9}$$

Λ is a measure of the scale at which QCD coupling approaches unity.

The structure of the leading order QCD coefficient b_0 in 2.4 requires both infrared slavery and asymptotic freedom. With three colors and six flavors, b_0 is always positive, implying that $\alpha_s(\mu)$ decreases with increasing renormalization scale. As the interaction energy becomes very large ($\mu \to \infty$), the QCD coupling goes to zero, implying that at very small distances, quarks and gluons act as free particles (asymptotic freedom). Furthermore, if the interaction distance becomes large ($\mu \to 0$), α_s becomes very large and makes any perturbation expansion meaningless, so an infinite amount of energy would be required to separate bound quarks and gluons. The requirement that quarks and gluons only exist in colorless bound states (hadrons) is termed infrared slavery, or *confinement.*

To calculate NLO dependence of the coupling on renormalization scale, terms of $\mathcal{O}\left(\alpha_s^3\left(\mu\right)\right)$ in 2.4 are included. The NLO solution for α_s becomes, in terms of the QCD mass scale

$$\alpha_s\left(\mu\right) = \frac{1}{b_0 \ln\left(\frac{\mu^2}{\Lambda^2}\right)}\left[1 - \frac{b_1}{b_0^2}\frac{\ln\left(\ln\left(\frac{\mu^2}{\Lambda^2}\right)\right)}{\ln\left(\frac{\mu^2}{\Lambda^2}\right)}\right]. \tag{2.10}$$

The choice of Λ still depends on the choice of the renormalization procedure used. All calculations contained herein use the "modified minimal subtraction" $\left(\overline{MS}\right)$ scheme [16] to define Λ to NLO.

2.2 The Parton-Parton Cross Section

The cross section expression given in 2.1 includes the partonic cross section, $d\widehat{\sigma}_{ij}$. The partonic cross section represents the cross section for the process $ij \rightarrow Q\overline{Q}X$, where i and j represent the interacting quarks or gluons, Q represents the heavy quark, and X represents anything else produced in the interaction. To obtain a next-to-leading order b-quark cross section, the partonic cross section must be calculated at LO and NLO.

2.2.1 Leading Order Contributions

Leading order, $\mathcal{O}\left(\alpha_s^2\right)$, production mechanisms for heavy quarks include gluon-gluon fusion and quark-antiquark annihilation:

$$\begin{aligned} g\left(p_1\right) + g\left(p_2\right) &\rightarrow Q\left(k_3\right) + \overline{Q}\left(k_4\right) \\ q\left(p_1\right) + \overline{q}\left(p_2\right) &\rightarrow Q\left(k_3\right) + \overline{Q}\left(k_4\right) \end{aligned} \tag{2.11}$$

Process	$\sum \left\|\overline{\mathcal{M}_{ij}}\right\|^2$
$gg \to Q\overline{Q}$	$\frac{2T_f}{D_A}\alpha_s^2 \left(\frac{C_f}{\tau_1\tau_2} - C_A\right)\left(\tau_1^2 + \tau_2^2 + \rho - \frac{\rho^2}{4\tau_1\tau_2}\right)$
$q\overline{q} \to Q\overline{Q}$	$\frac{C_f^2}{D_A}\alpha_s^2 \left(2\tau_1^2 + 2\tau_2^2 + \rho\right)$

Table 2.1: LO matrix elements. For $SU(3)_c$, $C_A = 3$, $C_f = 4/3$, $D_A = 8$, and $T_f = 1/2$.

The Feynman diagrams for these two processes are shown in Figure 2.2. Each vertex carries an associated coupling α_s. The matrix elements $\mathcal{M}_{ij}$ for the processes shown in Figure 2.2 have been calculated [17] and may be used to calculate cross sections. In Table 2.1, the matrix elements are averaged (summed) over initial (final) colors and spins, are calculated using the following ratios of scalar products:

$$\tau_1 = \frac{2p_1 \cdot k_3}{\widehat{s}} = \frac{m_Q^2 - \widehat{t}}{\widehat{s}}, \tau_2 = \frac{2p_1 \cdot k4}{\widehat{s}} = \frac{m_Q^2 - \widehat{u}}{\widehat{s}}, \rho = \frac{4m_Q^2}{\widehat{s}}, \tag{2.12}$$

where $\widehat{s}$, $\widehat{t}$, and $\widehat{u}$ are the Mandalstam variables describing the parton scattering. The partonic cross section for heavy quark production is given by

$$\frac{d\widehat{\sigma}_{ij}}{dyd^2k_T} = \frac{1}{\widehat{s}^2}\delta\left(1 - \tau_1 - \tau_2\right)\sum\left|\overline{\mathcal{M}_{ij}}\right|^2 \tag{2.13}$$

where y is the rapidity of the heavy quark in the center of mass system, and k_T is the heavy quark transverse momentum. For top and bottom quarks, this calculation should be reliable, as their masses are large enough for the perturbation expansion in α_s to be reliable.

2.2.2 Higher Order Corrections

Higher order corrections to the LO prediction for heavy quark pair production in QCD are expected to be suppressed by an additional factor of α_s, a suppression on the order of 10-20%. Heavy quark pair production, however, is an exception to this

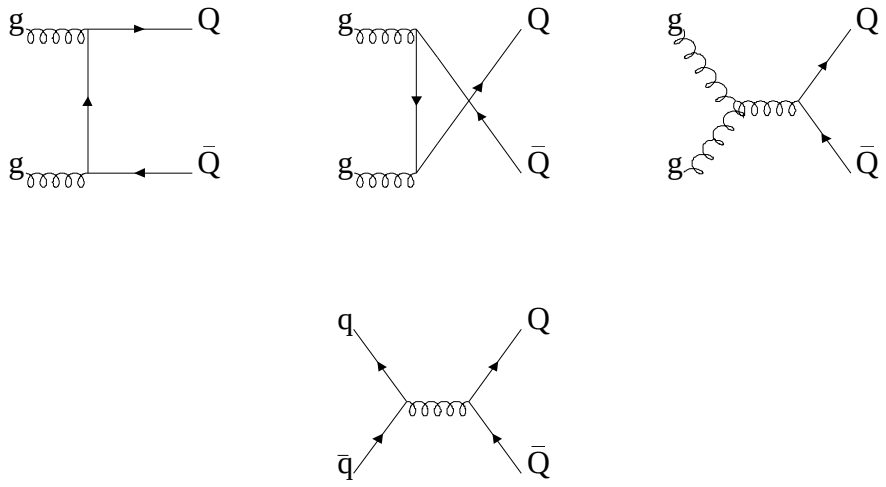

Figure 2.2: Leading order production mechanisms for heavy quarks: gluon fusion (top) and quark antiquark annihilation (bottom).

general QCD rule. The cross section for $gg \rightarrow gg$ is roughly a factor of a hundred larger than the cross section for $gg \rightarrow Q\overline{Q}$ [18]. The cross section referred to here is the partonic cross section convoluted with the structure functions (see Section 2.3), evaluated at low x. Even with the additional suppression of α_s, the production mechanism $gg \rightarrow gg^* \rightarrow gQ\overline{Q}$ (Figure 2.3) still contributes significantly to the overall production cross section. Note that the factor of a hundred is only valid for on-mass-shell gluons; the virtual gluon g^* is off-mass-shell by an amount on the order of the heavy quark mass, suppressing the virtual gluon diagram contribution.

Additional $\mathcal{O}(\alpha_s^3)$ diagrams are shown in Figure 2.3. Calculation of the b-quark cross section must include the processes

$$\begin{aligned} gg &\rightarrow Q\overline{Q}g \\ q\overline{q} &\rightarrow Q\overline{Q}g \\ gq &\rightarrow Q\overline{Q}g \end{aligned}$$

$$\begin{aligned} g\overline{q} &\rightarrow Q\overline{Q}g \\ q\overline{q} &\rightarrow Q\overline{Q} \\ gg &\rightarrow Q\overline{Q}. \end{aligned} \tag{2.14}$$

These diagrams depict processes that can give very different event topologies from those at leading order. Leading order processes produce heavy quarks back-to-back in azimuth, while NLO processes can produce very collinear heavy quark pairs that may no longer be back-to-back in phi. Figure 2.3 also depicts virtual diagrams whose interference with their LO counterparts contribute terms on the order of $\mathcal{O}(\alpha_s^3)$. These diagrams are necessary to cancel infrared and collinear singularities in the real emission diagrams [17].

2.3 Structure Functions

The remaining pieces of 2.1 to be evaluated before computing heavy quark production cross sections are the structure functions, F_i^1. The structure functions denote the probability that parton i will be found with a given momentum in hadron 1. The structure functions are evaluated at a mass scale, called the factorization scale, on the order of the momentum transfer of the hard scatter. The factorization scale is usually set equal to the renormalization scale at which α_s was calculated for convenience.

The structure functions are functions of x and Q^2, where x is the fraction of the proton the parton carries, and Q^2 is the momentum transfer. This analysis probes the structure functions at low x, where the gluon contribution to the b-quark cross section is significant at next-to-leading order.

The structure functions are generally parameterized at some scale μ_0 and evolved

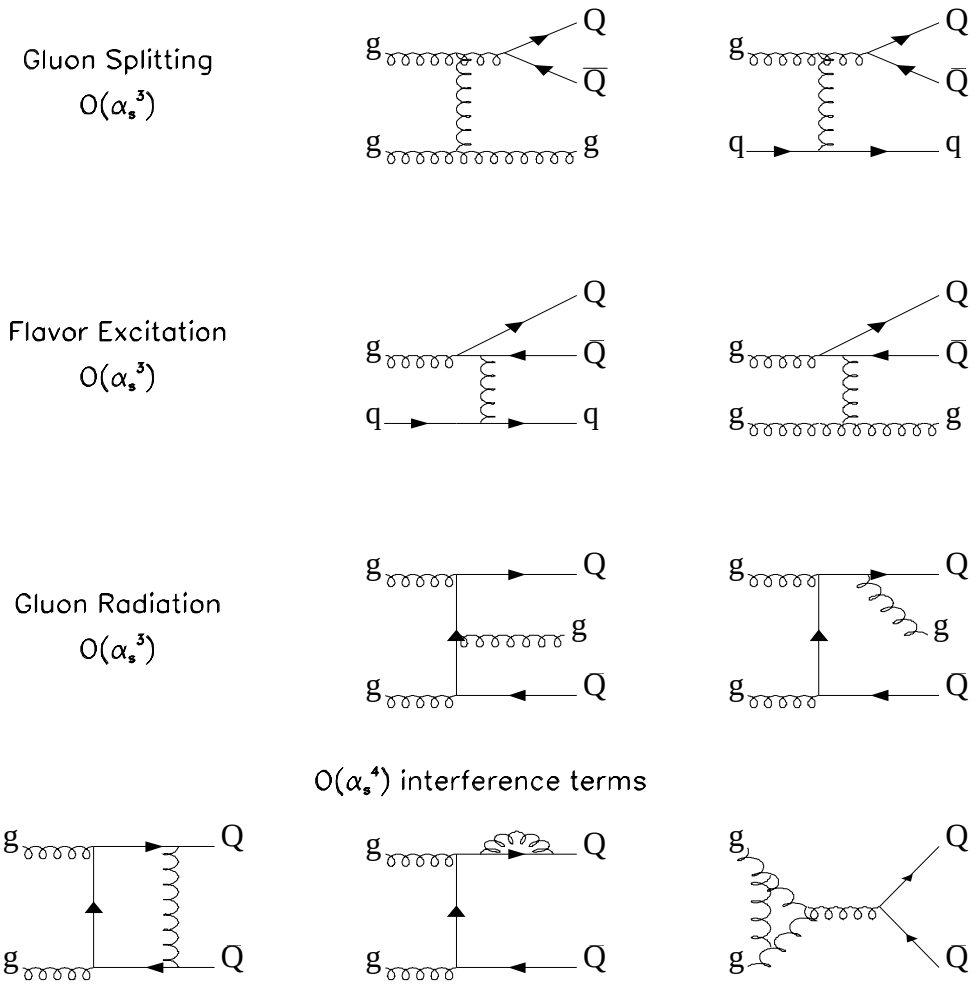

Figure 2.3: $\mathcal{O}(\alpha_s^3)$ diagrams contributing to NLO calculations include gluon splitting, flavor creation and gluon emission. Also shown are terms of $\mathcal{O}(\alpha_s^4)$ that interfere with the LO diagrams.

using the QCD mass scale Λ to some other scale μ at which experimental data are available. Fits to the data at various scales allow calculation of the best parameterizations of the structure functions. The term *parton distribution function* is used interchangeably with the term *structure function*.

2.4 Heavy Flavor Production Predictions at $p\overline{p}$ Colliders

After determining the strong coupling constant, the parton-parton cross section, and the structure functions, an inclusive b-quark production cross section can be obtained. The Nason, Dawson, and Ellis (NDE) predictions use an extension of the $\overline{MS}$ scheme for factorization and renormalization [17]. The inclusive b-quark cross section employs the following parameters in the calculation:

- The b-quark mass takes a value of 4.75 GeV/c^2. To obtain the error bands, the mass is allowed to vary in the range 4.5 GeV/c^2 $< m_b <$ 5.0 GeV/c^2.

- The renormalization and factorization scales are set equal and take on a value $\mu_0 = \sqrt{m_b^2 + p_{\rm T}^2}$. The errors due to scale dependence, which are present in any calculation to finite order in α_s, are estimated by allowing μ to vary between $\mu_0/2$ and $2\mu_0$.

- The parameter $\Lambda_{\overline{MS}}$ is taken to be 152 MeV and does not vary in this calculation.

- The parton distribution function used here, MRSR2, does not vary. This structure function is chosen for comparison because of the enhanced bottom production predicted over MRSA'.

The calculation performed in 2.1 can not be compared directly to data. In general, experimental data are sensitive only to b-quarks above a given p_{T} threshold ($p_{\mathrm{T}}^{\mathrm{min}}$) and within a selected rapidity region ($[y_{\mathrm{min}}, y_{\mathrm{max}}]$) determined by detector acceptances. Specifically, the $p_{\mathrm{T}}^{\mathrm{min}}$ is determined from Monte Carlo to be the p_{T} of the b-quark so that 90% of the $b \to \mu X$ cross section lies above this value. To facilitate the comparison between the theoretical calculation and experimental data, the prediction is rewritten in the form

$$\sigma\left(p\overline{p} \to bX; p_{\mathrm{T}}^{b} > p_{\mathrm{T}}^{\mathrm{min}}, |y_b| < y_{\mathrm{max}}\right) = \int_{-y_{\mathrm{max}}}^{y_{\mathrm{max}}} dy_b \int_{p_{\mathrm{T}}^{\mathrm{min}}}^{\infty} dp_{\mathrm{T}}^{b} \frac{d^2\sigma\left(pp \to bX\right)}{dy_b dp_{\mathrm{T}}^{b}}. \quad (2.15)$$

The resulting NLO prediction for the inclusive b-quark production cross section for $\sqrt{s} = 630$ GeV and $y_{\mathrm{max}} = 1$ is shown in Figure 2.4.

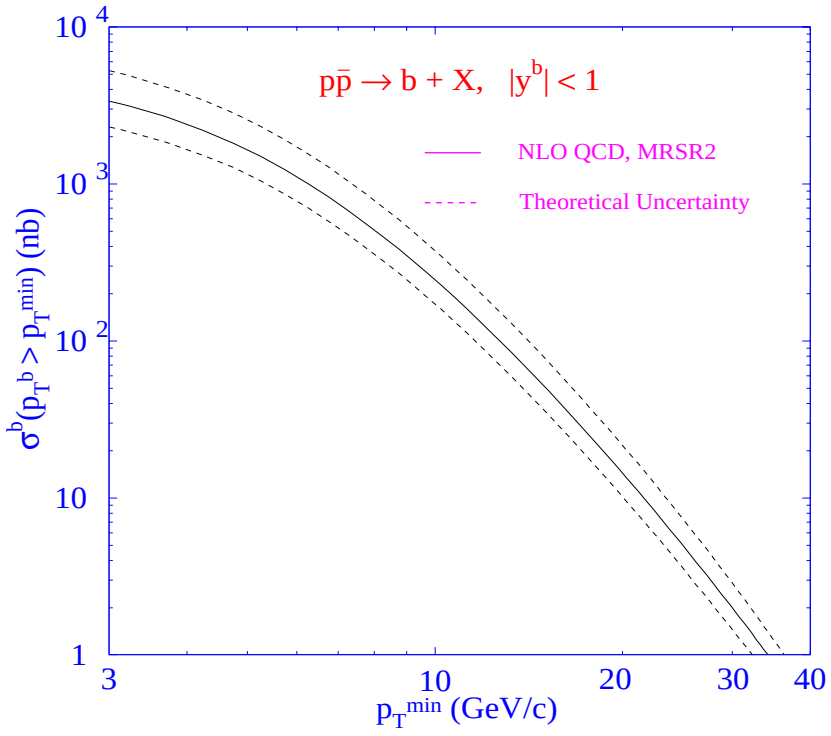

Figure 2.4: The NLO QCD prediction for the inclusive bottom quark production cross section. The prediction is generated using HVQJET, an implementation of the MNR calculation.

CHAPTER 3

MONTE CARLO SIMULATIONS

Monte Carlo event generators are invaluable tools for performing the complicated analyses in high energy physics. Monte Carlo, so named for the gambling quarter in Monaco, involves modeling various processes by using random numbers to generate physical distributions. For data analyses that have limited statistics, Monte Carlo (MC) provides a way to generate expected distributions for signal and background. Monte Carlo is also used to used to generated theoretical distributions based on previous experiments; these distributions can then be compared to the data to determine whether the theoretical predictions are correct.

This chapter serves to introduce the ISAJET Monte Carlo generator [19] and elucidate the various samples of Monte Carlo available for the analysis. Further tools that simulate the detector response to Monte Carlo events will also be explored. Future chapters will detail the manner in which the Monte Carlo events are employed.

3.1 The ISAJET Monte Carlo Generator

The Monte Carlo used in this analysis is generated using the ISAJET event generator. ISAJET produces events by first generating a primary $2 \rightarrow 2$ hard scatter according to appropriate QCD cross sections. For this analysis, the TWOJET option was used. The TWOJET option forces ISAJET to generate all $\mathcal{O}\left(\alpha_s^2\right)$ QCD processes. The cross sections from the hard scatter are then convolved with the proton structure functions:

$$\sigma = \sigma_0 \cdot F\left(x_1, Q^2\right) \cdot F\left(x_2, Q^2\right), \tag{3.1}$$

where σ_0 is the parton-parton cross section calculated from perturbative QCD, the parton structure functions are denoted $F(x_i, Q^2)$, in which x_i represent the fraction of the proton momentum that parton i carries, and Q^2 represents the momentum transfer scale.

QCD radiative corrections are then added to the initial and final states. Initial and final state particles are permitted to radiate gluons that can decay into $q\overline{q}$ pairs. This process is governed by the Altarelli-Parisi splitting functions that describe the probability that a given particle will split. The Altarelli-Parisi splitting functions are modeled using the branching approximations of Fox and Wolfram [21].

To avoid infrared and collinear singularities, each parton in the cascade is required to have an energy greater than some cutoff energy to be permitted to continue emitting quarks and gluons. Gluon radiations below this scale are assumed to be non-perturbative and are handled by the hadronization model. The default ISAJET cutoff of 6 GeV does not affect bottom quark production, because the threshold for producing a $b\overline{b}$ pair is twice the mass of the bottom quark, or 10 GeV. The cutoff will, however, affect charm production from gluon splitting and soft final state gluon radiation.

Next, partons are fragmented into hadrons. Any hadrons with lifetimes less than 10^{-12} seconds are decayed. Finally, ISAJET assumes that the remainder of the event energy enters in the form of minimum bias beam jets and adds them in.

3.1.1 Heavy Flavor Production Mechanisms

Within ISAJET, heavy flavor quarks can be produced via three mechanisms: *flavor creation* (FC), *flavor excitation* (FE), and *gluon splitting* (GS). All $2 \rightarrow 2$ processes

resulting in the production of only a $Q\overline{Q}$ pair are examples of flavor creation. FC processes represent the leading order production mechanism for heavy quarks.

Collisions in which a gluon splits into a heavy quark pair, and one of the heavy quarks scatters off another parton, are referred to as flavor excitation. Because an initial gluon splits prior to the hard scatter, an additional factor of α_s makes flavor excitation a higher order process.

In addition, heavy quarks are produced through gluon splitting. In GS, no heavy quarks are involved in the hard scatter. Instead, a final state gluon splits into a heavy quark pair. Similar to FE, the process of gluon splitting requires an additional QCD vertex, making gluon splitting a higher order process.

3.1.2 Hadronization of Heavy Quarks

After generating the hard scatter, ISAJET must form hadrons from the final state partons. This process, called *hadronization*, is modeled by the independent fragmentation ansatz originally proposed by Field and Feynman [22]. The final state quark, denoted q, creates a new $q'\overline{q}'$ pair in its color field. These new pairs are required to be created in the ratio $u : d : s = 0.43 : 0.43 : 0.14$, which reflects the strange quark's larger mass and resulting lower production probability. A new meson $\left(q\overline{q}^{'}\right)$ is formed with a fraction z of the original quark's momentum, with an averaged p_{T} of 0.35 GeV/c. The leftover quark in the process $\left(q^{'}\right)$ continues to fragment in the same fashion with a momentum of $(1-z)\,p$, where p is the original momentum of the heavy quark.

The momentum fraction z is defined as

$$\frac{E^{had} + p_L^{had}}{E^q + p^q}, \tag{3.2}$$

where p_L^{had} is the momentum of the hadron in the direction of q. ISAJET generates these fractions according to distributions from the Peterson model [23]. For heavy quarks, the fragmentation function takes the form

$$f(z) = \frac{z\,(1-z)^2}{\left[(1-z)^2 + \epsilon z\right]^2}. \tag{3.3}$$

The parameter ϵ is expected to scale with the mass of the heavy quark and is defined as

$$\epsilon_q = \frac{k_q}{m_q^2}, \tag{3.4}$$

where $k_b = 0.5$ is the default value supplied by ISAJET.

Baryons are also produced by ISAJET. These hadrons are produced by generating di-quark pairs with a probability of 0.1 instead of a single quark.

3.1.3 Decay of B Hadrons

Once the heavy quark has been hadronized, it is forced to decay. ISAJET uses the spectator $V-A$ model to decay hadrons. The light quark in the meson is considered to be only a spectator in the decay of the heavy quark, so the heavy quark is allowed to decay as a free particle (Figure 3.1). The decay occurs via the normal $V-A$ weak current. This model of semileptonic decay neglects gluon radiation, binding effects, and other perturbative and nonperturbative QCD corrections, but for the large mass of the bottom quark, these effects are expected to be negligible.

Although B mesons decay directly via the weak current to leptons, they can also produce leptons via a secondary decay. The B meson decays weakly to a D meson,

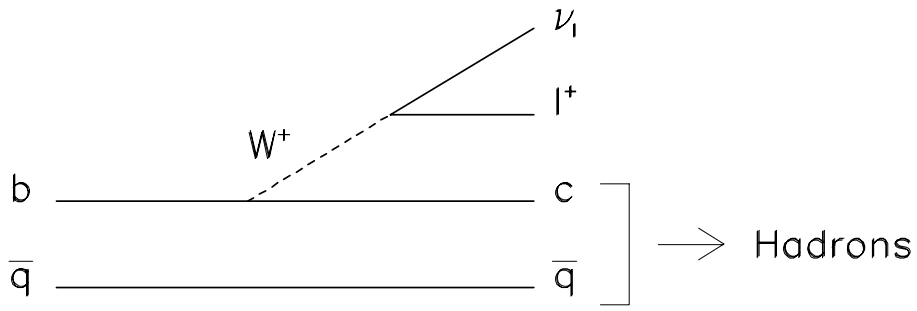

Figure 3.1: Spectator decay of a B meson. The bottom quark decays as a free particle.

and the charm quark in the D can decay semileptonically through the same weak mechanism. This decay chain is sometimes referred to as sequential decay of the B to leptons. The spectator model is expected to be less accurate for sequential decays, however, due to the lighter charm quark mass.

LEP measurements [24] have determined the inclusive semileptonic branching ratio for B mesons into muons to be

$$BR\left(B \to \mu^{\pm}\nu_{\mu}X\right) = 11.0 \pm 0.3 \pm 0.4\%. \tag{3.5}$$

ISAJET uses 12% for this branching ratio, so to ensure that its predictions are accurate, a correction factor of $\left(\frac{11}{12}\right)$ is applied to the cross section per event for every event in which a bottom quark decays directly to a muon. Because the branching ratios used by ISAJET agree with experimental measurements, no corrections are made for events in which a muon originates from the decay of a charm quark.

3.1.4 ISAJET Hard Scatter p_T

The Monte Carlo used in this analysis was generated with the ISAJET event generator package. At the heart of every event generated is a $2 \to 2$ hard scatter. The user

defines the transverse momenta of the hard scatters to be generated. In general, the momenta of the hard scatters are chosen to be between 4 and 80 GeV/c (see, for example, Table 3.1), because quarks with a transverse momentum less than 4 GeV/c do not generally produce muons that will pass through the DØ iron toroid.

Because the bottom quark production cross section falls steeply with increasing transverse momentum, this simulation of physics distributions is time-consuming and CPU intensive. To obtain large statistics in regions where the cross section for production is small, one can generate Monte Carlo in bins of hard scatter transverse momentum. The cross section per event, or ISAJET weight, is simply adjusted to result in the complete cross section when all bins are summed.

The Monte Carlo used for this analysis has also been generated with the lower threshold for hard scatter transverse momentum set somewhat higher than 4 GeV/c. Because this analysis requires the presence of a 12 GeV jet, it was determined that events generated at less than 10 GeV/c rarely satisfy the requirements placed on the data sample (see, for example, Table 3.1).

3.1.5 ISAJET Version

Monte Carlo event generators are often updated to include new physics results. These updates can include new branching fractions, new cross sections, and newly descovered energy states for a particular particle. Each successive version of a generator must be cross-checked with any Monte Carlo used in an analysis to ensure that new Monte Carlo events are not needed.

Recently ISAJET was updated to version 7.37. The new version of ISAJET includes new data from the CLEO collaboration. CLEO, with the largest collection of B

meson decay data ever produced, has done a great deal of B meson spectroscopy and published a plethora of results on various decay states. Version 7.37 of ISAJET includes the new CLEO decay table, whereas previous versions (*e.g.*, isajet 7.13) did not. The different versions must be compared to determine the magnitude of the impact on this analysis.

In Chapter 6, ISAJET Monte Carlo is used to fix the ratio of bottom sequential decay to direct bottom decay for purposes of background subtraction. In addition, the background subtraction technique relies heavily on the Monte Carlo distributions of the transverse momentum of the muon relative to its associated jet axis. In addition, the fraction of muons originating from the decay of a bottom quark is compared to the data and must also be cross-checked between versions.

ISAJET TWOJET samples were generated using versions 7.13 and 7.37. Only events containing a muon and a heavy quark were examined. The ratio of sequential decay to direct bottom decay as a function of generated muon transverse momentum is shown in Figure 3.2 for both versions. The transverse momentum of the muon relative to the direction of the nearest heavy quark is plotted for both versions in Figure 3.3. The fractions of muons originating from a bottom decay as a function of muon transverse momentum are compared in Figure 3.4. All distributions exhibit good agreement within errors between versions.

3.1.6 HVQJET

For the b-produced muon cross section and the inclusive bottom quark production cross section, the results are compared to theoretical predictions. The theoretical predictions used are obtained using HVQJET, a Monte Carlo simulation developed

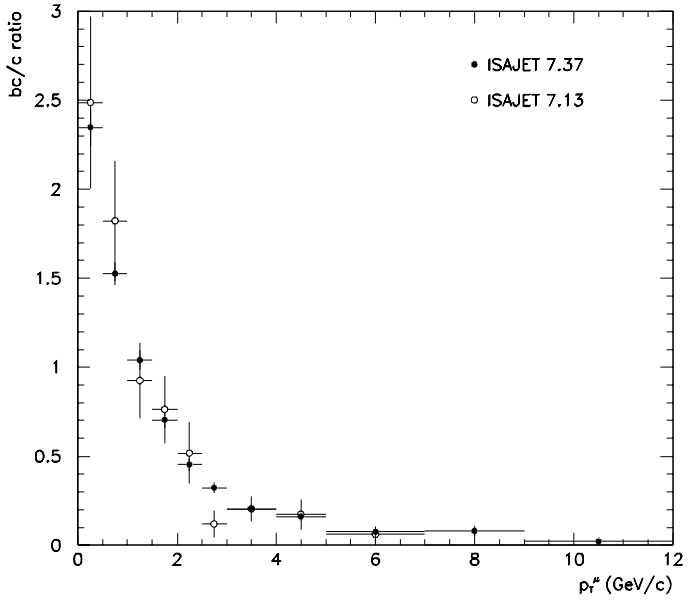

Figure 3.2: Comparison of the sequential decay to direct bottom decay ratios between ISAJET V7.13 and V7.37.

at DØ by Marc Baarmand, which provides a direct calculation of the NLO MNR prediction [15]. HVQJET uses the MNR parton level generator and a modified version of ISAJET for hadronization, particle decays, and underlying event modeling.

In HVQJET, the MNR prediction is realized by combining events with large negative weights with events with positive weights and similar topologies, resulting in events that have positive weights only. The transverse momentum spectrum produced by HVQJET was cross-checked against that produced by the MNR calculation, indicating that this negative weight cancellation process does not significantly affect the cross section [25].

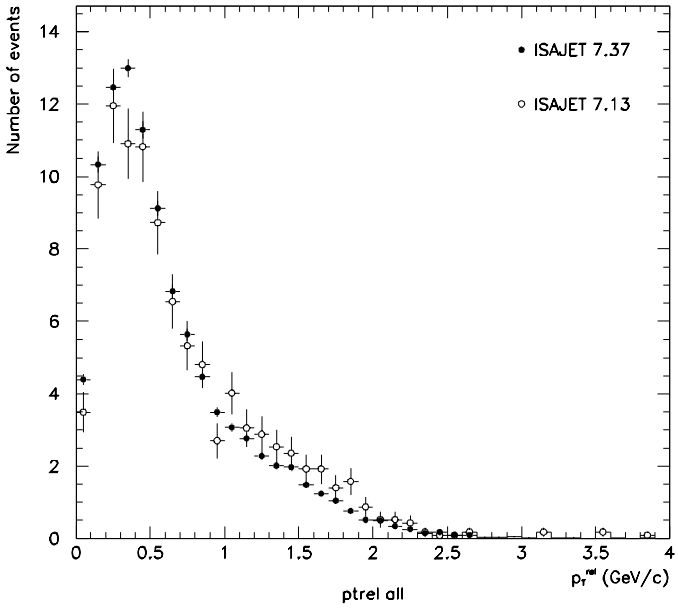

Figure 3.3: Comparison of the distributions of muon transverse momentum relative to the nearest heavy quark between ISAJET V7.13 and V7.37.

3.2 Monte Carlo Simulation of Data

It is not sufficient to merely simulate physics events with Monte Carlo. The data are collected with the DØ detector (Chapter 4), which affects the distributions observed. Fortunately, it is possible to pass the Monte Carlo events through a full detector simulation so they look similar to the data.

Once an event sample has been generated, it is passed through DØGEANT. GEANT is a multi-purpose tool used to simulate the passage of particles through matter developed at CERN. Effects modeled in GEANT include multiple Coulomb scattering, full electromagnetic and hadronic showering, bremsstrahlung, and particle decays. DØGEANT refers to a customized version of GEANT that includes a full physical description of the DØ detector. DØGEANT then uses the particle tracks to produce

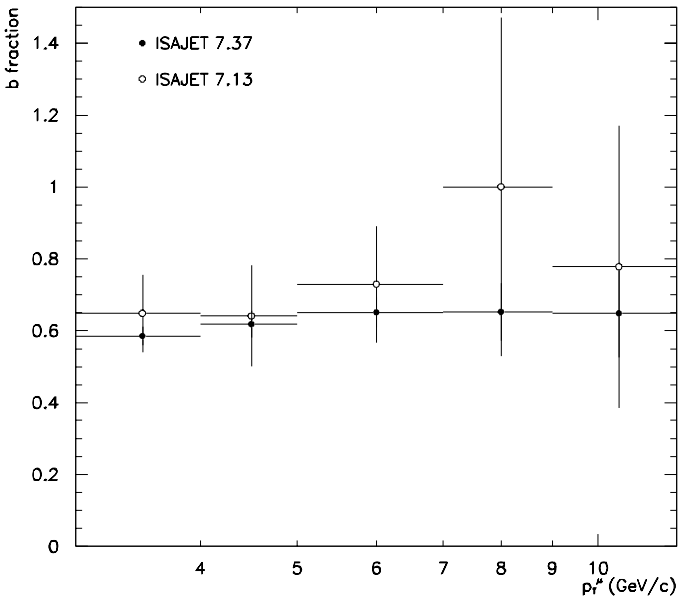

Figure 3.4: Comparison of the fraction of muons originating from bottom quark decays as a function of muon transverse momentum between ISAJET V7.13 and V7.37.

simulated hits in the detector, analogous to raw data.

Unfortunately, DØGEANT does not properly simulate all inefficiencies in the muon system. For example, it does not include alignment uncertainties or drift time resolutions. The true muon momentum resolution is not as good as the assumed resolution in DØGEANT. More information about resolutions can be found in Chapter 7.

The MUSMEAR package was created to simulate the smearing of muon momentum. Having a separate package allows one set of Monte Carlo to be processed with several versions of MUSMEAR, resulting in Monte Carlo that simulates data at various periods during the running of the experiment. In Run 1, due to the variation of chamber efficiencies (described in more detail in Section 5.3.2), the package was developed for two distinct running periods: prior to zapping the muon tracking chambers and after

zapping the chambers.

In addition to correctly simulated detector hits, proper simulation of the data requires a simulation of the trigger system. TRIGSIM is a package designed to simulate the full DØ trigger system, described in detail in Section 4.3. Full simulation of the Level 1 and Level 1.5 hardware triggers, as well as the Level 2 software trigger system, is included.

3.2.1 Decay Background Monte Carlo

The charged pion and kaon branching fraction for decay into muons is large, so π/K in-flight decay is expected to contribute significantly to the muon sample. The contribution is somewhat reduced because the decay lengths of the particles are boosted in the lab frame, so the fraction of charged particles decaying in the central tracker is small. In addition, the average transverse momentum for muons from these decays is less than 1 GeV, so only a small fraction are expected to traverse the iron toroid.

To speed production of pion and kaon decay Monte Carlo, a decay package was developed by the Arizona group at DØ [20]. A sample of ISAJET TWOJET events was generated, and each event was input into the decay simulator. The decay package determined the list of possible candidates $(\pi^{\pm}, K^{\pm}, K_L^0)$ for which $p_T^{\pi/K} > 3.0$ GeV/c and $\left|\eta^{\pi/K}\right| < 0.9$. A particle from this list was chosen at random and forced to decay into a muon. The probability that this type of decay occurs is expressed as

$$P = \left(1 - e^{-\frac{R_{CD}}{c\tau} \cdot \frac{m_{\pi/K}}{E_{\pi/K}}}\right) \cdot BR\left(\pi/K \rightarrow \mu\right), \tag{3.6}$$

where R_{CD} is the radius of the central tracking volume, $c\tau$ is the particle decay length, and $BR\left(\pi/K \rightarrow \mu\right)$ is the appropriate branching fraction to muons. The

decay modes included in this package are $\pi^+ \to \mu^+\nu_\mu$, $K^+ \to \mu^+\nu_\mu$, $K^+ \to \pi^0\mu^+\nu_\mu$, and $K_L \to \pi^\pm\mu^\mp\nu_\mu$, as well as the corresponding charge conjugate modes. The weight assigned to each event is given by the product of the original cross sectional weight of the single muon event with the probability for producing a muon from a pion or kaon decay in the event.

3.3 Various Monte Carlo Samples

In addition to the data ntuples, several samples of Monte Carlo are available for this analysis. For completeness and ease of reference, the available Monte Carlo samples are listed in Table 3.1. The table lists the name of the Monte Carlo set, the ISAJET version used to generate TWOJET events, the bins for the transverse momenta of the hard scatter, and any cuts applied to the generation process. After GEANTing, all raw events were smeared with MU_SMEAR_E95XX_R8892.RCP, obtained from the low and high energy data of Run 1C. The DØ trigger system was simulated using TRIGSIM 7.17 in conjunction with L301.GLB-TRIGLIST. Finally, the reconstruction of the raw information was performed using DØRECO 12.21.

MC Set	ISAJET **version**	**Generation Bins (GeV)**	**Cuts**
IND set 1	7.13	9 bins (6-10, 10-15, 15-20, 20-30, 30-40, 40-50, 50-60, 60-70, 70-80)	$p_{\rm T}^{\mu} > 3$ GeV/c, $\lvert\eta^{\mu}\rvert \leq 1.0$
IND set 2	7.13	1 bin (8-80)	$p_{\rm T}^{\mu} > 3$ GeV/c, $\lvert\eta^{\mu}\rvert \leq 1.0$
IND π/K	7.13	4 bins (5-10, 10-20, 20-40, 40-80)	$p_{\rm T}^{\mu} > 3$ GeV/c, $\lvert\eta^{\mu}\rvert \leq 1.0$
RIO set 1	7.22	1 bin (20-100)	$p_{\rm T}^{\mu} > 3$ GeV/c, $\lvert\eta^{\mu}\rvert \leq 1.0$ $\phi^{\mu} < 220^{\circ}$ or $\phi^{\mu} > 320^{\circ}$
RIO set 2	7.22	1 bin (20-100)	$p_{\rm T}^{\mu} > 3$ GeV/c, $\lvert\eta^{\mu}\rvert \leq 1.0$ $50^{\circ} < \phi^{\mu} < 130^{\circ}$
RIO set 3	7.22	1 bin (20-100)	$p_{\rm T}^{\mu} > 3$ GeV/c, $\lvert\eta^{\mu}\rvert \leq 1.0$ $30^{\circ} < \phi^{\mu} < 150^{\circ}$
RIO set 4	7.22	1 bin (10-20)	$p_{\rm T}^{\mu} > 3$ GeV/c, $\lvert\eta^{\mu}\rvert \leq 1.0$ $30^{\circ} < \phi^{\mu} < 150^{\circ}$
FNAL π/K	7.22	5 bins (1-3, 3-6, 6-10, 10-20, 20-100)	$p_{\rm T}^{\mu} > 3$ GeV/c, $\lvert\eta^{\mu}\rvert \leq 1.0$ $30^{\circ} < \phi^{\mu} < 150^{\circ}$

Table 3.1: The Monte Carlo available for this analysis.

CHAPTER 4

THE DØ EXPERIMENT

Fermi National Accelerator Laboratory (FNAL) is home to the world's highest energy particle accelerator, the Tevatron. The Tevatron operates in two different modes. In Fixed Target mode, the Tevatron delivers 900 GeV particle beams to fixed target experiments such as KTEV or NUTEV. In Collider Mode, the Tevatron provides counter-rotating beams of protons (p) and anti-protons ($\bar{p}$) with a center of momentum (CM) energy $\sqrt{s} = 1.8$ TeV.

The DØ collaboration studies the high p_{T} physics and mass states produced by these energetic beams. With the DØ detector, the collaboration has produced a great deal of new and exciting physics, including the simultaneous discovery of the top quark in 1995 by the DØ and CDF (Collider Detector at Fermilab) collaborations [11][12]. In addition, DØ has made precision measurements of the W boson mass [26], led the search for new particles, and constrained perturbative QCD in studies of hadronic jets and heavy quark production.

Following the 1994-1995 run of the Tevatron (termed Run 1B), the center of momentum energy was reduced to study the energy dependence of many physics processes. The energy, $\sqrt{s} = 630$ GeV, was chosen to match the energy used in the UA1 experiment at CERN. The run of the Tevatron corresponding to the 630 GeV CM energy is termed the Low Energy Run (LNR).

4.1 The Fermilab Tevatron

Creating and colliding stable particle beams of such energies is a multi-stage task. The Tevatron itself is the last of seven components used to create the proton and antiproton beams: the Cockroft-Walton pre-accelerator, the Linac, the Booster Synchrotron, the Main Ring, the Debuncher, the Accumulator, and finally, the Tevatron. Figure 4.1 depicts the general layout of the machines used in the acceleration process. The interested reader may obtain additional information about the accelerators elsewhere [27].

4.1.1 The Cockroft-Walton Pre-accelerator

The proton and antiproton beams begin their lives in a fairly humble tank of hydrogen gas. A magnetron surface-plasma source ionizes the hydrogen, producing a pulsed 18 keV H^- beam. The H^- ions are injected into a commercial Cockroft-Walton accelerator that boosts the energy of the ions to 750 keV using a cascading voltage multiplier.

4.1.2 The Linac

Transport lines direct the ion beam from the Cockroft-Walton into a two-stage linear accelerator (linac). A 79 m Alvarez drift-tube accelerator boosts the energy of the ions to 116 MeV. Quadrupole magnets focus the beam throughout acceleration. A side-coupled linear accelerator continues boosting the energy to 400 MeV. The beam is directed at a carbon foil target that strips the electrons from the ionized hydrogen, producing a pure proton beam.

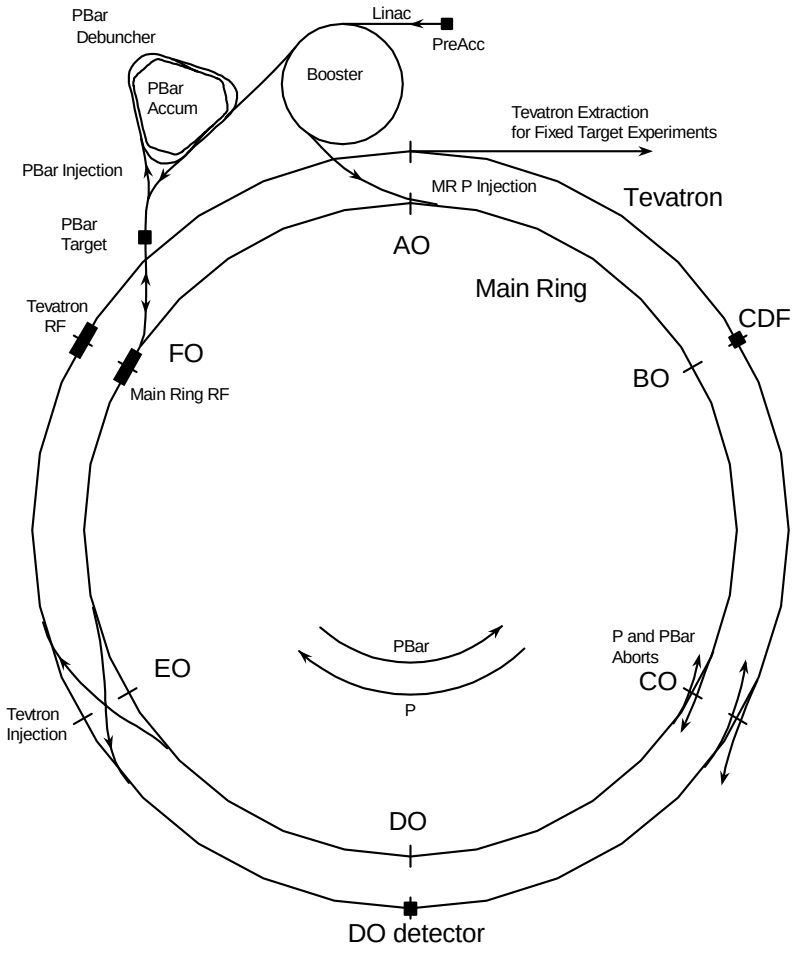

Figure 4.1: An overview of the system of accelerators used to accelerate protons and antiprotons at Fermilab. The picture is not drawn to scale: while the Main Ring and the Tevatron have the same diameter, they are shown offset here for clarity.

4.1.3 The Booster Synchrotron

The proton beam is injected into the Booster accelerator. The Booster is a synchrotron with a diameter of 151 m that serves as an injector for the main ring. Ninety-six dual function dipole/quadrupole magnets keep the beam focused and in a closed orbit. The frequency of RF electromagnetic fields is raised synchronously with the magnetic field strength (necessary due to relativistic effects). The protons are accelerated to an energy of 8 GeV and injected into the Main Ring.

4.1.4 The Main Ring Accelerator

The Main Ring synchrotron is similar to the Booster; however, the Main Ring is much larger, with a diameter of 2 km. The Main Ring steers and focuses the proton beam with one hundred copper coil magnets. Before Tevatron injection, the Main Ring provides the antiproton source with a beam of protons. Proton bunches with an energy of 120 GeV are directed onto a nickel/copper target. The antiprotons produced in the collisions are focused with a cylindrical lithium lens. Antiprotons with energies near 8 GeV are selected to match the energy of the proton beam injected into the Main Ring by the Booster. After enough antiprotons are accumulated by the $\overline{p}$ Debuncher and Accumulator Complex, the Main Ring accelerates the proton and antiproton beams to 150 GeV and injects the beams into the Tevatron.

4.1.5 The $\overline{p}$ Debuncher and Accumulator Complex

Initially the antiprotons are incoherent, exhibiting a large variance in momentum. Using stochastic cooling [28], the Debuncher reduces the variations in particle mo-

mentum about the 8 GeV mean. After cooling, approximately 2×10^{10} antiprotons are sent to the Accumulator, which further cools the antiprotons and stores them until 2×10^{11} antiprotons have accumulated. Typically, the accumulation proccess requires four to six hours. One "store" of protons and antiprotons lasts from 12 to 14 hours, giving the Main Ring time to accumulate enough antiprotons for another store.

4.1.6 The Tevatron Ring

After enough antiprotons accumulate, the Main Ring injects six bunches of protons and six bunches of antiprotons into the Tevatron, which is suspended 2 feet below the Main Ring. A typical proton bunch contains roughly 150×10^9 particles, while an antiproton bunch typically contains 50×10^9 particles. The Tevatron employs roughly one hundred superconducting magnets, cooled to 4.6 K by a liquid helium cooling system, to simultaneously focus and direct the beams. The Tevatron accelerates the bunches to 315 GeV, resulting in collisions with a CM energy $\sqrt{s} = 630$ GeV and a bunch crossing time of about 3.5 μs.

Once the beams reach the target energy, they are forced to collide in the center of the DØ and CDF detectors. Special focusing magnets, called the low beta quadrupoles, reduce the cross sectional area of each beam to approximately 1 mm^2.

The number of crossings each second through unit cross section is referred to as the instantaneous luminosity. Throughout Run 1B, for example, the Tevatron delivered a variety of instantaneous luminosities, ranging from $1 \times 10^{30} s^{-1} cm^{-2}$ to

Running Period	Dates	Delivered Lum.	Recorded Lum.
1A	1992-1993	23.0 pb^{-1}	15 pb^{-1}
1B	1994-1995	121.5 pb^{-1}	87.6 pb^{-1}
1C	1995-1996	16.9 pb^{-1}	12.7 pb^{-1}

Table 4.1: The total integrated luminosity from the three running periods during Run 1. These numbers are estimated to be correct to within 5%.

$25 \times 10^{30} s^{-1} cm^{-2}$. Integrated luminosity is defined as

$$\mathcal{L} = \sum_i L_i \Delta t_i, \tag{4.1}$$

where L_i represents a constant "instantaneous" luminosity over some time interval Δt_i. The sum runs over all time intervals of interest, making it possible to discuss, for example, the integrated luminosity of a given run range. Figure 4.2 depicts the integrated luminosity for all of Run 1. The integrated luminosities in the Table are expressed in barns, with the relation 1 barn = 10^{-28} m^2. The plot shows both delivered and accumulated luminosities, which are also given by partial run in Table 4.1. This thesis uses data from a low energy run taken just prior to Run 1C.

4.2 The DØ Detector - From the Inside Out

The DØ detector was intended to be a general purpose detector, useful for studying the high p_T and large mass states produced in the very high energy collisions of the Tevatron. It was designed with the following goals in mind:

- Excellent lepton identification
- Good energy resolution for parton jets with a very high transverse energy (E_T)
- Good measurement of missing E_T ($\not\!\!E_T$), which indicates the presence of neutrinos and other non-interacting particles

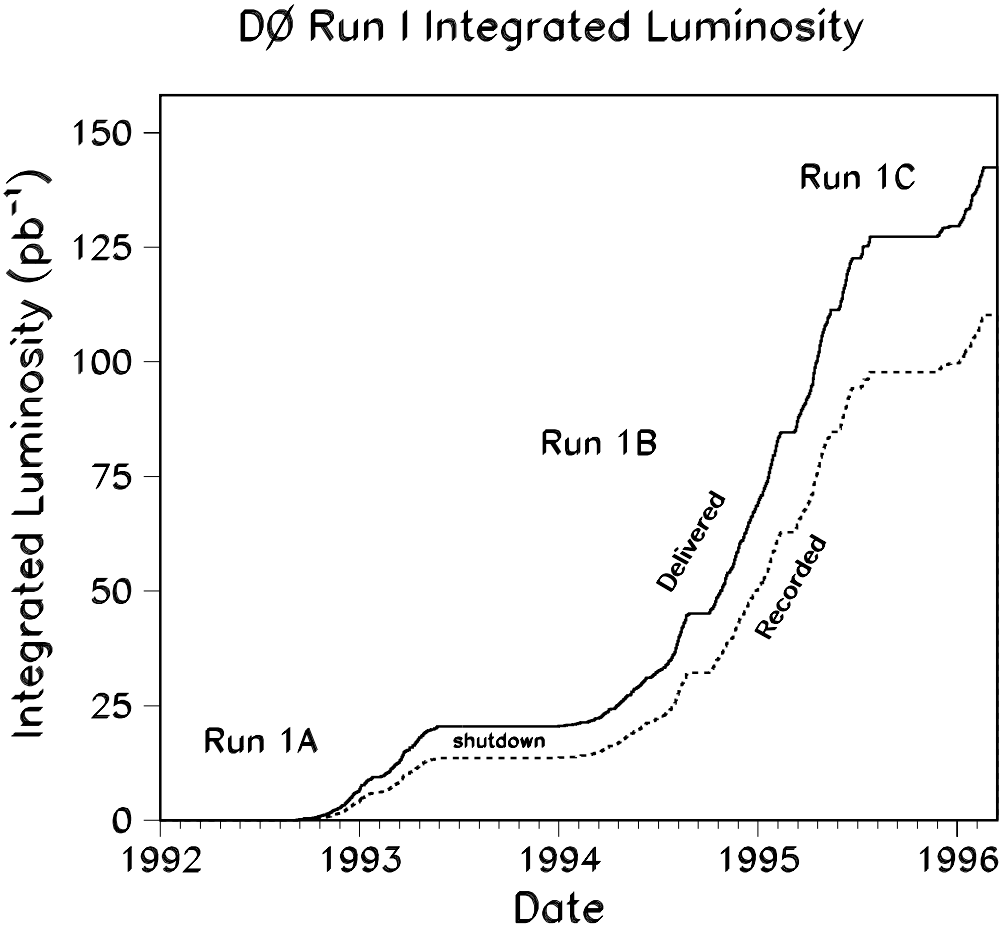

Figure 4.2: The luminosity delivered by the Tevatron and recorded by DØ as a function of date.

For example, the top quark and W boson have appreciable branching fractions for leptonic channels, while accompanying QCD backgrounds have much smaller branching fractions. The detector was required to have a nondestructive tracking and vertex detection system, a hermetic calorimeter that would detect leptons, hadrons, and neutrinos (via measurement of $\not\!\!E_{\mathrm{T}}$), and a muon system to detect leptons that escape the calorimeter. The resulting detector has the following features:

- A stable, hermetic, finely segmented, thick, and radiation hard liquid argon calorimeter
- A muon detection apparatus that includes a thick iron toroid to provide sufficient momentum resolution and protection from hadronic punchthrough
- A compact non-magnetic tracking volume with adequate spatial resolution and emphasis on electron background suppression

Figure 4.3 shows a cutaway view of the DØ detector. This simplified rendering depicts all three primary subsystems: the central detector, the calorimeter, and the muon system. Each primary detector subsystem and its components is described below. For reference beyond this thesis, an interested reader may consult [29]. Various coordinate systems are used to describe physics objects and detector component placement; a detailed description of the coordinate systems used at DØ is presented in Appendix A.

4.2.1 The Central Detector (CD)

The central detector consists of four subsystems, all of which provide non-destructive detection of charged particles: the Vertex Detector (VTX), the Transition Radiation

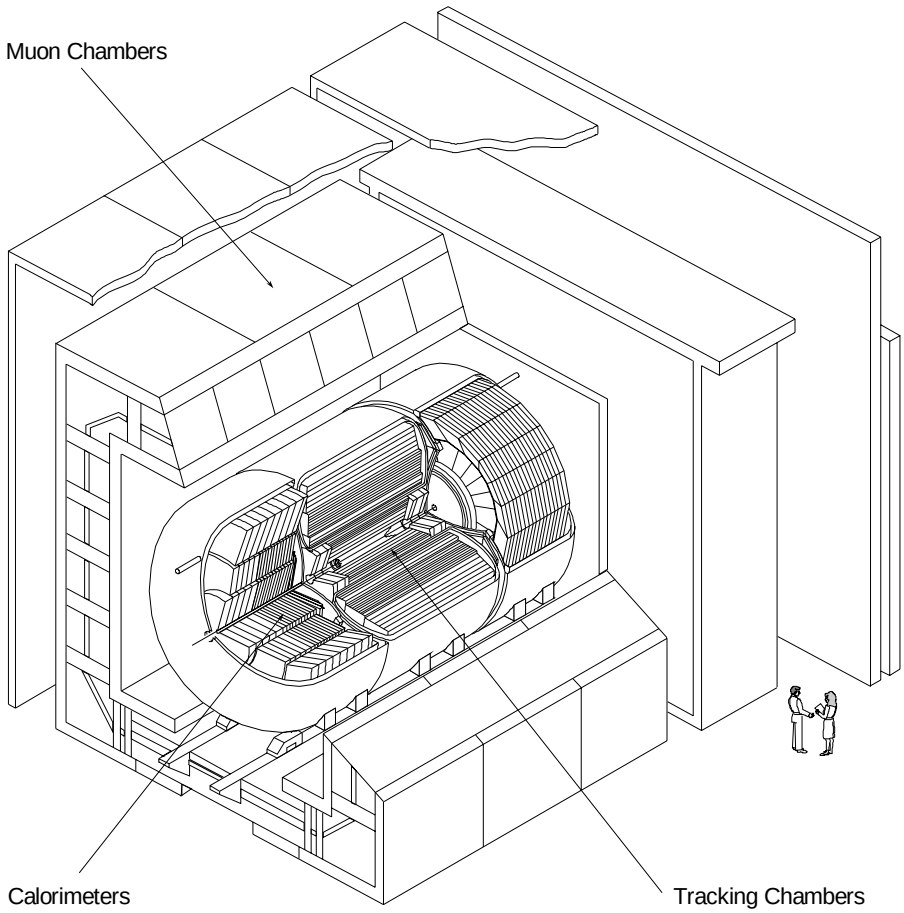

Figure 4.3: A cutaway view of the DØ detector depicting the three major detector components.

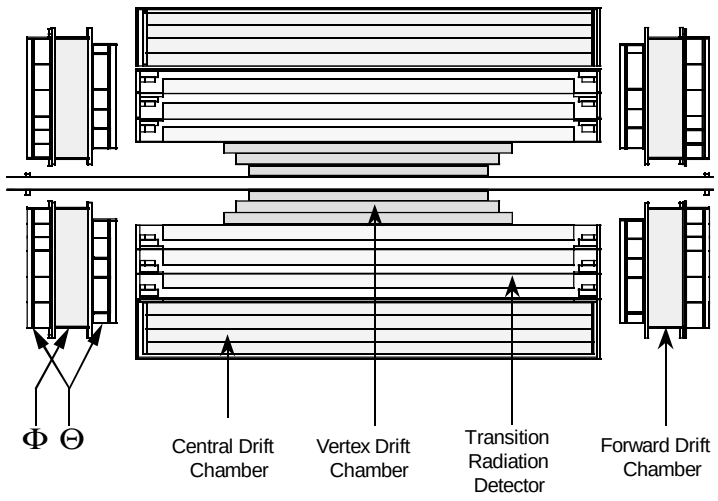

Figure 4.4: Detail of the central detector showing the VTX, CDC, TRD, and FDC.

Detector (TRD), the Central Drift Chambers (CDC), and the Forward Drift Chambers (FDC). The VTX, TRD, and CDC form coaxial cylinders around the beam pipe, covering a region out to $|\eta| < 1.2$. The FDC are oriented perpendicular to the beam pipe and provide coverage for the region $1.4 < |\eta| < 3.1$. Figure 4.4 depicts the design of the CD.

By design, the central detector allows reconstruction of charged particle trajectories originating from the interaction vertex. The information is used to locate the event vertex and find electromagnetic showers (either e^- or γ). The main design requirements were to produce an inner tracking system with good two-track resolving power, high efficiency, and ionization energy measurement capabilities.

A particle passing through a gas interacts electromagnetically with atomic electrons near the path of the particle. The interactions create electron-ion pairs, the

number of which depends on the energy of the particle and the type of gas used. Typically, 100 pairs/cm will be formed. An electric field causes the particles to drift towards the anode of the drift chamber, repeatedly colliding with gas molecules. If the applied field is strong, electrons kick other electrons out of gas molecules, and these loose electrons also drift toward the electrode. This exponential avalanche of electrons eventually materializes as a current on the anode proportional to the original number of electrons created.

Because an electron only initiates an avalanche when close to the anode, an electron moves at approximately constant speed through the rest of the gas. Measurement of the elapsed time between electron creation and collection can be used to determine the distance of the original source particle from the anode. This type of measurement is characteristic of a drift chamber. The VTX, CDC, and FDC are all drift chambers. The TRD detects transition radiation, and its operation is described in section 4.2.1.

The Vertex Detector (VTX)

For $|\eta| < 2$, the products of a high energy $p\overline{p}$ collision must first pass through the VTX [30], which lies directly outside the beam pipe. The Vertex Detector was designed to accurately determine the position of the event vertex. The VTX provides vertex resolution of about 1.5 cm along the z-axis. It also provides position resolution of approximately 50-60 μm for charged particle tracks.

The vertex chamber consists of three mechanically independent concentric layers of cells. The active region extends from an inner radius of 3.7 cm to an outer radius of 16.2 cm. The active length of the layer closest to the beam pipe is 97 cm, while each successive layer grows larger by approximately 10 cm. The innermost layer consists

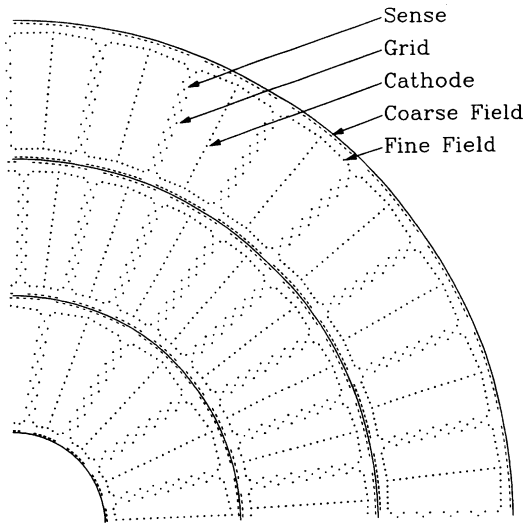

Figure 4.5: End view of the VTX showing the positions of the sense, field, and grid wires.

of 16 cells in azimuth, while the outer two each contain 32 cells. The walls between the cells are made of low density carbon fiber to minimize photon production of e^-e^+ pairs. Each cell contains eight sense wires, made of 25 μm NiCoTin [31], that measure the $r-\phi$ coordinate (Figure 4.5). Adjacent sense wires are staggered by 100 μm to resolve left-right ambiguities. The three layers of cells are offset in ϕ to aid pattern recognition.

The active medium, a CO_2-ethane gas mixture (95%:5%) with a small amount of H_2O added [32], provides good spatial resolution. The average drift velocity, about 7.3 μm/ns, results in a maximum drift time of 2.2 μs, comfortably within the collider bunch-crossing time of 3.5 μs.

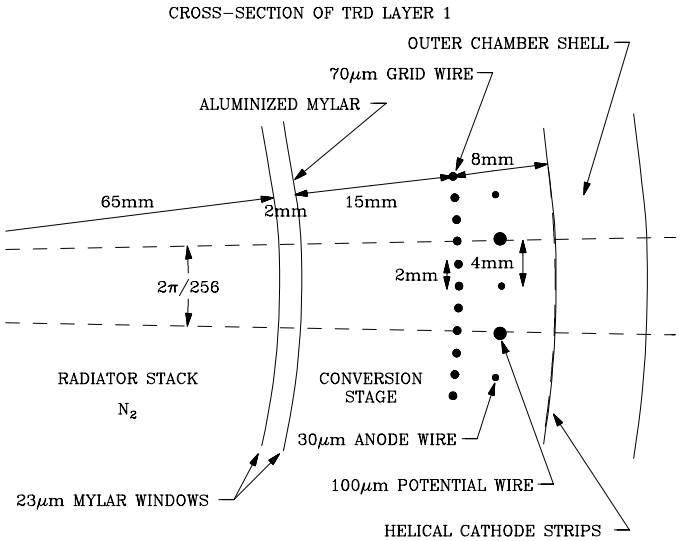

Figure 4.6: This cross sectional view of one section of the transition radiation detector shows the radiator and the detector in detail, as well as the positions of the various wires.

The Transition Radiation Detector (TRD)

Wrapped around the VTX, the Transition Radiation Detector provides electron identification independent of the DØ calorimeter. The TRD consists of three independent sections, each containing a radiator and an X-ray detector. A cross sectional view of the TRD is shown in Figure 4.6.

When a very relativistic particle passes between media with different dielectric constants, a dipole formed by the real charge and an image charge on the opposite side of the interface flips direction, producing transition radiation X-rays [33]. The energy of the X-rays emitted by a specific particle with a given momentum, is determined by the thickness of the radiator foils and the gaps between them. The three DØ TRD units each contain a radiator with 393 polypropylene foils, each 18 μm thick, in a

volume filled with N_2. The gap between foils is 150 μm. An electron passes through alternating layers of polypropylene and nitrogen, resulting in an X-ray spectrum that peaks at 8 keV and is mostly contained below 30 keV [34].

Immediately behind the radiator, proportional wire chambers (PWC) detect the X-rays. The X-rays convert in the first stage of the PWC, and the resulting charge drifts radially outward to the sense cells, where avalanche ionization occurs as described above.

Between the radiator and the detector lie two 23 μm mylar windows. Dry CO_2 gas flows between the windows to prevent the nitrogen in the radiator from leaking into the detector volume. The detector volume is filled with a gas mixture of Xe, CH_4, and C_2H_6 (91%:7%:2%), an efficient X-ray absorber because xenon has a large Z (Z=54) [35]. The outer mylar window is aluminized to serve as a high voltage cathode in the detection stage. The 15 mm conversion stage and the 8 mm amplification stage are separated by a grid of 70 μm gold-plated tungsten wires. Helical copper strips serve as the outer cathode of the amplification stage and are also used to measure the z coordinate of the $p\overline{p}$ interaction. The anodes are 30 μm gold-plated tungsten wires separated by 100 μm gold-plated copper/beryllium potential wires. Each TRD has 256 anode readout channels.

The Central Drift Chambers (CDC)

Located just outside the TRD and just inside the central calorimeter, the CDC (Figure 4.7) provides coverage for tracks at large angles. The active volume is a cylindrical shell 184 cm long, with an inner radius of 49.5 cm and an outer radius of 74.5 cm. Four coaxial rings of 32 azimuthal cells, each containing seven 30 μm gold-plated tungsten

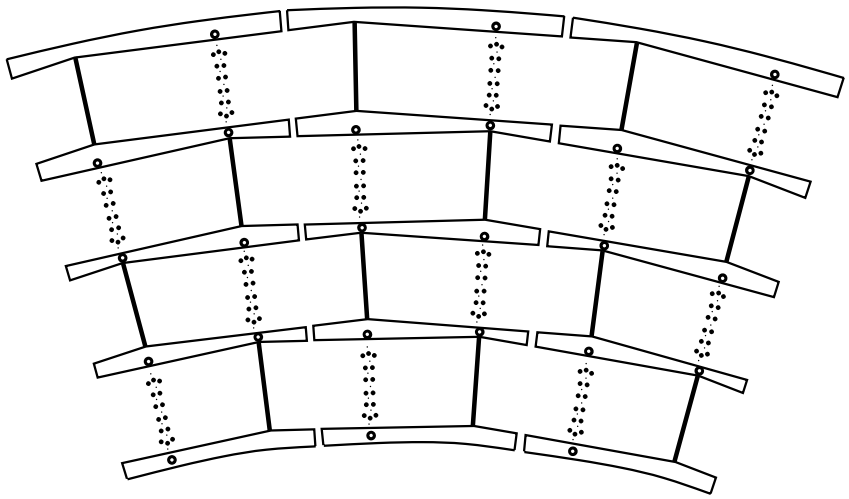

Figure 4.7: Detail of the central drift chamber.

sense wires, comprise the CDC. Within the cell, adjacent wires are staggered in ϕ by 200 μm to resolve left-right ambiguities. Two delay lines allow a determination of the z-coordinate of the track by measuring the difference of arrival times. The gas used in the CDC is an Ar, CH_4, and CO_2 mixture (92.5%:4%:3%) with 0.5% H_2O.

Forward Drift Chambers (FDC)

In the forward region of the CD, the forward drift chambers [36][37] (Figure 4.8) provide coverage for charged particles down to about $\theta = 5^\circ$ with respect to the beam axis. As depicted in Figure 4.4, the FDC's are located at the end of the CDC, TRD, and VTX and extend to the inner walls of the end calorimeter. The active region of the FDC extends out to a radius of 61 cm.

The two FDC's are made up of three modules each: one Φ module sandwiched between two Θ modules. The Φ module measures the ϕ coordinate with sense wires

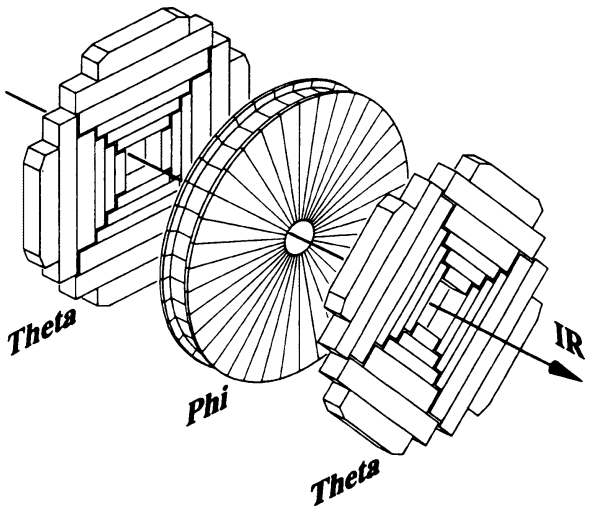

Figure 4.8: This depiction of the forward drift chambers shows the azimuthal offset between the two Θ layers as well as the placement of the six rectangular cells.

oriented perpendicular to the beam pipe, while the two Θ modules measure the θ coordinate. The Φ module consists of a single chamber containing 36 sections that cover the full azimuth. Each section has 16 anode wires in z. The Θ modules are divided into independent quadrants, each containing 6 rectangular cells. Each cell contains eight anode wires directed in z. The sense wires in the three inner cells lie at one edge, forcing the electrons to move in only one direction thereby removing the left-right ambiguity. Each Θ module has one delay line to give a local measurement of the orthogonal coordinate. The two Θ modules are also rotated in ϕ by 45° with respect to each other. In all modules, adjacent anode wires are staggered by 200 μm to resolve ambiguities. The FDC's use the same gas mixture as the CDC's.

4.2.2 The DØ Calorimeter

The DØ experiment relies on the calorimeter for measurements of electrons, photons, and jets. In addition, it serves to identify muons as minimum ionizing particles (MIPs) with a characteristic energy deposition of approximately 2 GeV.

The DØ calorimeter (Figure 4.9) acts as a "sampling" calorimeter: only a portion of the particle's energy is measured by the active medium as the particle traverses the volume of the calorimeter. While each individual calorimeter component is described below, all components rely on the same basic principle: particles traverse alternating layers of a dense absorbing material and an active medium, causing a shower of particles, increasing particle multiplicity until all the energy is dissipated and sampled by the active medium. The DØ calorimeter is designed to detect both electromagnetic and hadronic showers.

The calorimeter is divided into three pieces: the central calorimeter (CC), and the two end calorimeters (north EC and south EC). The CC covers a pseudorapidity region $|\eta| \leq 1$, while the EC extend the coverage to $|\eta| \approx 4$. Both the central and end calorimeters contain three distinct detection systems: the electromagnetic calorimeter with relatively thin uranium absorber plates, the fine hadronic calorimeter with thick uranium absorber plates, and a coarse hadronic calorimeter with either thick copper or stainless steel absorber plates. Each calorimeter subsystem employs liquid argon (LAr) as the active medium.

Electromagnetic showers arise when electrons pass through a dense absorbing medium with an energy greater than a material-dependent critical energy ($\sim$ 100 MeV for uranium). The energetic electrons lose energy almost entirely through

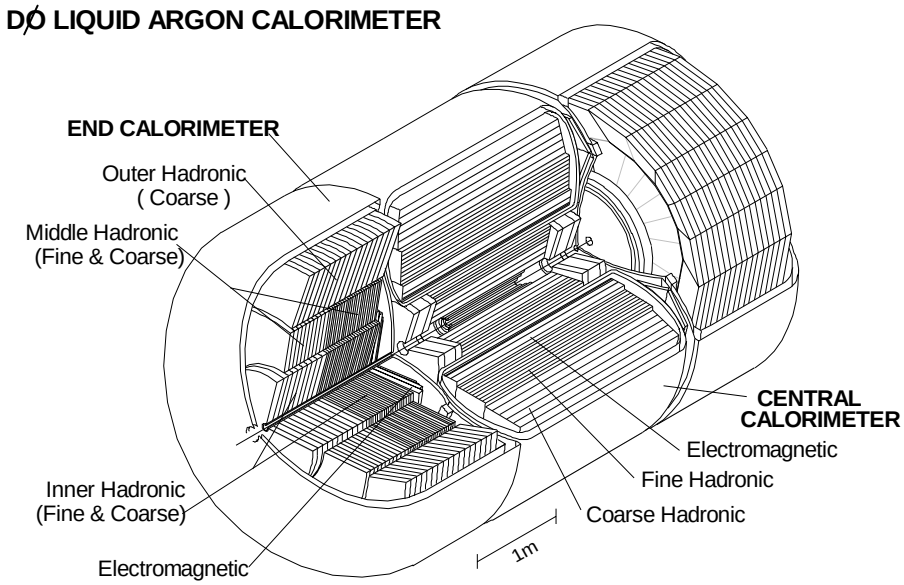

Figure 4.9: Cutaway view of the calorimeter showing the various layers in both the central and end regions.

bremsstrahlung. Bremsstrahlung (literally "braking radiation") describes the process by which a charged particle interacts with the Coulomb field around a nucleus and emits an energetic photon. This high energy photon, which typically carries a significant fraction of the electron's energy, interacts primarily by pair production, resulting in an e^-e^+ pair. These electrons and positrons can also bremsstrahlung, producing a cascade of particles until all the particles have energies below the critical energy for the absorbing material. Below the energy threshold, the energy loss is dominated by ionization and excitation. Such a cascade is referred to as an electromagnetic shower.

Through fundamentally different physical processes, hadronic particles can also initiate showers. Hadrons collide inelastically with atomic nuclei, producing secondary hadrons that themselves undergo inelastic collisions. Roughly half of the initial hadronic energy observed as ionization of the LAr is associated with these secondary hadrons, while the other half is lost to nuclear binding energies and neutron kinetic energy. This hadronic cascade is called a hadronic shower. Like the electromagnetic showers, the cascade continues until all the energy is dissipated by ionization losses or nuclear processes.

Using the absorber plates and active medium described above, DØ is able to detect and measure the energy of both types of showers. Each module in the calorimeter contains a stack of interleaved absorber plates and signal boards. A 2.3 mm LAr-filled gap separates the absorber plates and the signal boards. A signal board consists of a copper pad sandwiched between two 0.5 mm sheets of G10, which is coated on the LAr side with a resistive coating. A charged particle leaves a trail of ionization as it passes through the liquid argon. The resistive coating, held at 2.0-2.5 kV with respect to the grounded absorber plates, collects the ionization, and the signal is read out

from the copper pads.

The calorimeter cells are typically segmented such that the cell readout space is 0.1×0.1 in $\eta - \phi$. Electromagnetic showers deposit the majority of their energy in the third layer of the EM calorimeter, so the cells in that layer have an area of 0.05×0.05. In addition, cells in the very forward region $|\eta| > 3.2$ are larger in both η and ϕ.

The Central Calorimeter (CC)

The CC provides coverage out to a pseudorapidity of 1.2 and consists of three concentric cylindrical shells. The innermost shell contains 32 electromagnetic modules (CCEM), constructed to be thick enough to contain most electromagnetic showers. Surrounding the CCEM is a shell of 16 fine hadronic modules (CCFH) designed to measure the energy of hadronic showers. The outermost layer of the calorimeter contains 16 coarse hadronic cells (CCCH) that measure any leakage from the CCFH and reduce punchthrough into the muon system. Each layer is rotated azimuthally with respect to the previous layer so that no projective rays cross more than one intermodule gap. The radiation lengths, χ_0, of the central calorimeter modules are 20.5, 96.0, and 32.9, for the CCEM, CCFH, and CCCH modules respectively.

The End Calorimeters (EC)

Each end calorimeter (ECN and ECS) is made up of four subdetectors and provides a pseudorapidity coverage of $1.3 \leq |\eta| \leq 4.0$. The electromagnetic (ECEM, shown in Figure 4.10) and inner hadronic (ECIH) modules contain only one module. Outside the ECEM and ECIH lie concentric rings of 16 middle (ECMH) and outer (ECOH) hadronic modules. The various modules are rotated with respect to one another to

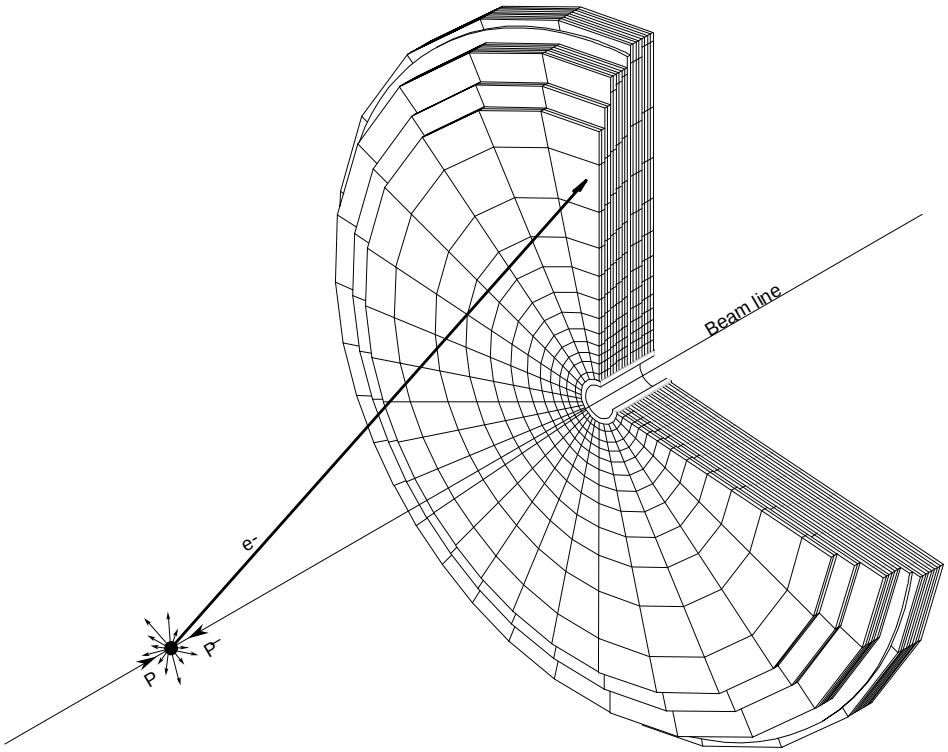

Figure 4.10: View of the ECEM. The readout boards form disks with no azimuthal cracks. The ICEM is of similar construction.

prevent particles from escaping the calorimeter.

Massless Gaps and the Intercryostat Detectors (ICD)

The region $0.8 \leq |\eta| \leq 1.4$ contains uninstrumented space used by support structures, module endplates, and the cryogenic walls of the central and end calorimeters. To account for the energy not measured by the CC and EC in this gap, two scintillation arrays, called intercryostat detectors, were mounted on the front surface of the end calorimeters. Each ICD consists of 384 scintillators, segmented to match the $\eta - \phi$

area of the LAr cells in the calorimeter.

In addition to the ICD, single-cell structures were installed on the faces of the CCFH, CCMH, and CCOH. These structures, called massless gap detectors, consist of two signal boards surrounded by three LAr gaps. The gaps also exhibit a segmentation $\Delta\eta = \Delta\phi = .1$ to match the ICD and the calorimeter cells. The massless gaps and the ICD provide a good approximation to the LAr sampling of EM showers.

Calorimeter Performance

In a test beam setup, the calorimeter module response was studied using single electrons and pions. The response for both electromagnetic and hadronic modules was found to be linear within 0.5%. The resolution can be parametrized as

$$\left(\frac{\sigma}{\mathrm{E}}\right)^2 = \mathrm{C}^2 + \frac{\mathrm{S}^2}{\mathrm{E}} + \frac{\mathrm{N}^2}{\mathrm{E}^2} \ , \tag{4.2}$$

where constants C, S, and N represent calibration errors, sampling fluctuations, and noise contributions, respectively. For electrons, the measured constants are

$$\mathrm{C} = 0.003 \pm 0.002,\ \mathrm{S} = 0.157 \pm 0.005\ \mathrm{GeV}^{\frac{1}{2}},\ \mathrm{N} \approx 0.140\ \mathrm{GeV}, \tag{4.3}$$

and for pions

$$\mathrm{C} = 0.032 \pm 0.004,\ \mathrm{S} = 0.41 \pm 0.04\ \mathrm{GeV}^{\frac{1}{2}},\ \mathrm{N} \approx 1.28\ \mathrm{GeV}. \tag{4.4}$$

The fractional energy resolution of the DØ detector is roughly $15\%/\sqrt{\mathrm{E}}$ for electrons and $50\%/\sqrt{\mathrm{E}}$ for pions [29].

4.2.3 The DØ Muon System

The outermost system of the DØ detector, the muon system, consists of five iron toroid magnets, a system of proportional drift chambers (PDT's), and scintillators. The

muon system is divided into two subsystems: the wide angle muon system (WAMUS) provides coverage of the pseudorapidity region $|\eta| \leq 2.5$, while the small angle muon system extends the coverage out to $|\eta| \leq 4.0$, and is designed to operate in the high rate environment near the beam pipe. In both WAMUS and SAMUS, three layers of muon chambers (A, B, and C) provide a measurement of the muon momentum and direction. the muon toroids are positioned between the A and B layers of the muon system.

The Muon Toroids

The muon system employs five iron toroids. The toroids fulfill two functions in the muon system. First, the sign and momentum of muon tracks are determined by the bend angle of the muon track passing through the toroid. In addition, the longitudinal depth of toroid plus the calorimeter reduces the hadronic punchthrough to the muon chambers. Punchthrough refers to any hadronic particles produced by showers in the calorimeter that produce hits in the muon system. The rate of punchthrough into the muon system varies with pseudorapidity, but in the central region, the rate is less than 2% of all tracks [38]. Because the punchthrough rate is kept to a minimum, identifying muons within hadronic jets is relatively easy.

At $\eta = 0$, a muon must have a momentum greater than 3 GeV/c to make it through the iron. Because the amount of iron subtended by a muon track increases with pseudorapidity, at larger η, a muon needs 5 GeV/c to traverse the 13-20 interaction lengths of iron. The thickness in interaction lengths as a function of polar angle θ is given in Figure 4.11. Additional problems with detector acceptance exist at the bottom of the detector due to holes created by the calorimeter support structure.

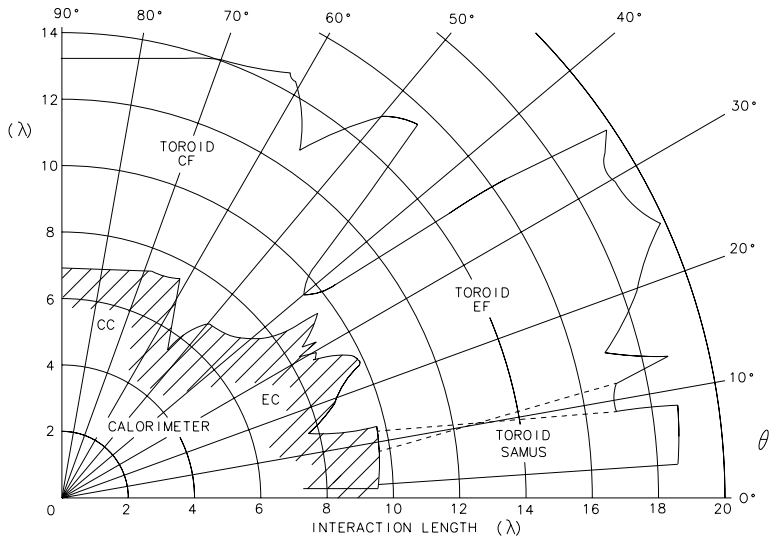

Figure 4.11: Thickness of the calorimeter and muon system in interaction lengths.

The central toroid is a square annulus 109 cm thick centered on the Tevatron beam lines. The inner surface of the CF toroid is 317.5 cm from the beam. To permit access to the inner portions of the detector, the central toroid was constructed in three pieces. A middle bottom section is fixed to the detector platform. Two C-shaped shells complete the central toroid. Twenty coils of ten turns each carry currents of 2.5 kA to create internal fields of 1.9 T. Fringe fields can exceed .01 T near the central beam.

The two EF toroids use eight coils of eight turns carrying 2.5 kA to generate fields of up to 2 T. The end toroids extend in z from 447 cm to 600 cm. The outer surfaces are located at a perpendicular distance of 417 cm, and each EF toroid has a 183 cm square hole centered on the beam line.

Within each inner hole of the EF toroid lies a separate SAMUS toroid. Two coils

Region	Construction	Wire Material	Gas (Drift Sp.)	Resolution
WAMUS	Rectangular aluminum extrusion	Gold-plated Tungsten (50 μm)	Ar, CF_4,CO_2 90%:5%:5% (6.5 cm/μs)	$\sim$ 0.4 mm
SAMUS	Cylindrical stainless steel tubes	Gold-plated Tungsten 50 μm	CF_4,CH_4 90%:10% (9.7 cm/μs)	$\sim$ 350 μm

Table 4.2: Technical details of the WAMUS and SAMUS wire chambers

of 25 turns carry a current of 1 kA, providing a field aligned with that in the EF toroid. The outer surface of the SAMUS toroids is located 170 cm from the Tevatron beams, and a 102 cm square hole is centered on the beam line.

The Wide Angle Muon System

The wide angle muon system (WAMUS) provides muon momentum and sign measurement in the pseudorapidity region $0 \leq |\eta| \leq 2.5$, corresponding to all of the CF and most of the EF toroids. The WAMUS system is composed of 164 proportional drift chambers (PDTs) arranged in three layers. The A layer lies inside the iron toroid, while the B and C layers lie outside. Each layer is made up of several planes (called decks) of PDTs: the A layer is composed of four decks of 10 cm drift chambers, while the B and C layers are each made up of three decks. The technical details of the WAMUS PDTs (Figure 4.12) are given in Table 4.2.

The coordinate ξ along the wire direction (non-bend view) is measured using a combination of cathode pad signals and timing information from the anode wires. Each cathode strip contains an inner and an outer pad ganged together separated by a repetitive diamond pattern that repeats every 61 cm (Figure 4.13). The ratio of the sum and difference of inner and outer signals provides a measure of the ξ coordinate,

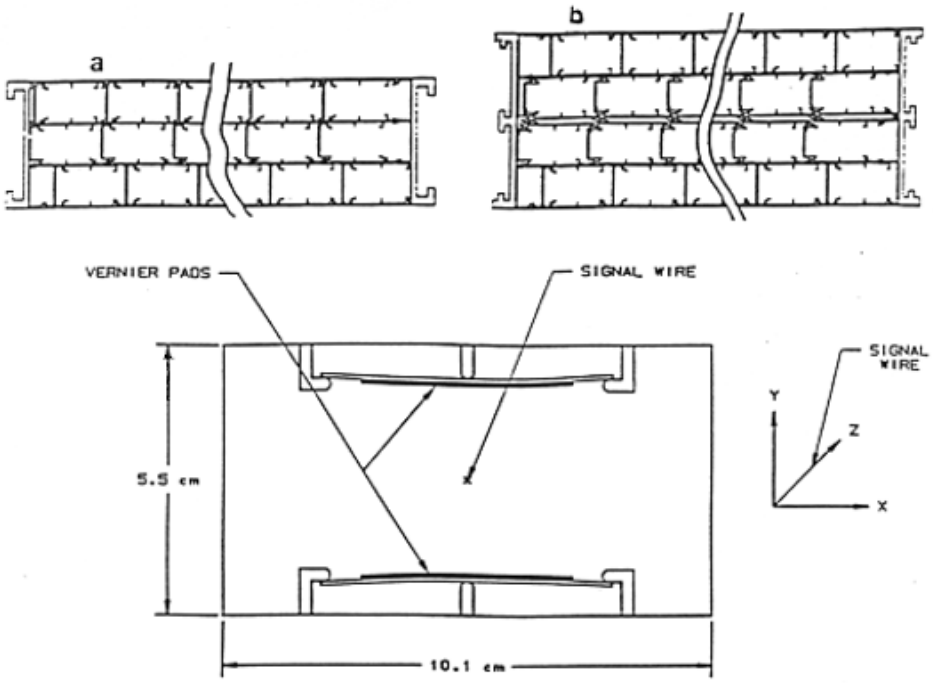

Figure 4.12: End view of the WAMUS PDTs depicting the arrangement of cells in three and four deck layers as well as the placement of the cathode pads.

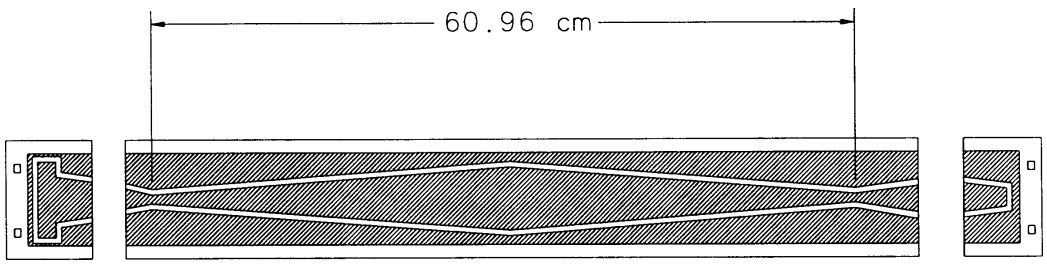

Figure 4.13: WAMUS drift tube cathode pad structure.

modulo half the repeat length of the diamond pattern ($\approx$ 30 cm). Ambiguities are resolved using the time difference of the signal arriving along the anode at both ends of the chamber. For a given chamber, the ξ resolution is approximately $\pm$3 mm.

The Small Angle Muon System

The small angle muon system consists of two mirror image systems, north and south. Three layers (A, B, and C) of doublet planes (two-deck planes) of cylindrical PDTs provide coverage out to $|\eta| \leq 4.0$. The A station, the closest to the center of the detector, precedes the SAMUS toroid, while the B and C stations lie between the SAMUS toroid and the beginning of the low-beta quadrupole for DØ insertion. The three planes in each layer are oriented in x, y, and u (rotated 45° with respect to x or y) (Figure 4.14). The technical details of the SAMUS PDTs can be found in Table 4.2.

Scintillators

Because cosmic ray produced muons comprise a large background to beam-produced muons, muon scintillators [39] were installed on the outside of the C layer of the muon

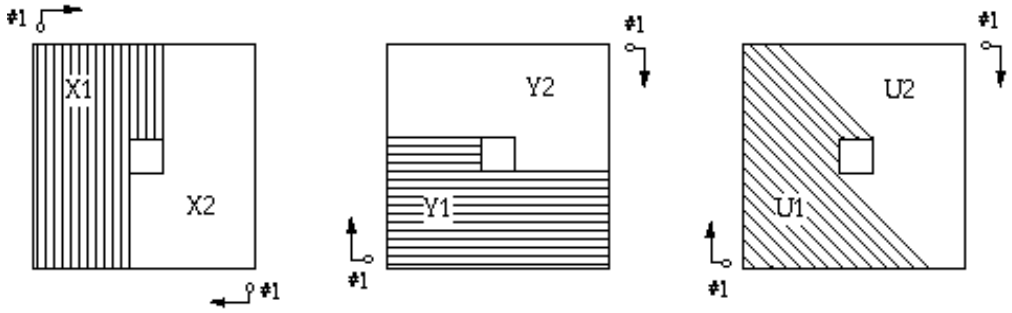

Figure 4.14: Diagram showing the orientation of the three layers in each plane of the Small Angle Muon System (SAMUS).

system during Run 1B. The scintillators, 1/2" Bicron 404A scintillator [40] material, measure 25 inches in width with lengths varying from 81.5" to 113" depending on the PDT to which it is attached. The scintillators are mounted in a nested configuration designed to reduce geometrical inefficiencies.

A muon passing through the scintillating material typically deposits 2 MeV of energy, creating roughly 2×10^4 photons in the scintillator. The photon signal is amplified by a factor of 10^7 by photomultiplier tubes. For the data used in this analysis, the scintillators are active during a 50 ns time window centered on the beam crossing time.

4.3 The DØ Trigger System

Writing to tape every event that occurs in the high luminosity environment provided by the Tevatron is impossible. To select the most interesting physics events from a sea of background events, DØ developed a sophisticated triggering system designed to reduce the rate of the events written to tape. The trigger system has three levels of increasing sophistication. Level Ø is a hardware based system relying on scintillators

to indicate the presence of inelastic collisions. At a luminosity of 5×10^{30} cm^{-2}s^{-1}, the rate out of Level Ø is about 150 kHz. The Level 1 trigger, a hardware-based trigger, mostly operates within the 3.5 μs bunch crossing time. Level 1 triggers that require several beam crossings to form their trigger decisions are referred to as Level 1.5 triggers. The rate out of Level 1 is roughly 200 Hz, while the rate out of Level 1.5 is approximately 100 Hz. The final trigger, Level 2, consists of a farm of microprocessors. This farm forms a software triggering system that further reduces the trigger rate to about 2 Hz. Events passing the Level 2 trigger are sent to host computers to be written to 8 mm tape.

4.3.1 Level Ø

The Level Ø trigger detects inelastic collisions, monitors luminosity, provides a relative zero-time for other triggers, and provides a fast measurement of the z-coordinate of the interaction vertex. The Level 0 detector consists of two hodoscopes with a checkerboard-like array of scintillating counters covering the pseudorapidity region $1.9 < |\eta| < 4.3$. The time resolution for each counter is 100-150 ps. Measurement of the relative arrival times of the signals in each hodoscope provides a fast measurement of the position of the interaction vertex to within 8 cm. Because E_T is z-dependent, this interaction position information must be determined quickly enough to be used by the $\not\!\!E_T$ triggers at Level 2. After obtaining information from the rest of the detector, the position can be resolved to within ± 3 cm. In a high luminosity environment, multiple interactions occur frequently. When a multiple interaction occurs, the Level Ø vertex measurement is ambiguous and a flag is set to mark this occurrence.

4.3.2 The Level 1 Trigger Framework

The trigger at Level 1 must function within the 3.5 μs bunch crossing time. Because of this stringent time limitation, the Level 1 trigger is composed of hardware logic devices that find objects such as muons, electrons, and jets. Each of the hardware triggers send decisions to the Level 1 framework, which uses a two-dimensional AND/OR network array that collects 256 input bits. The output from the array consists of 32 preselected trigger conditions. Each of the trigger conditions is formed from the 256 inputs bits by requiring that each bit must be either asserted, negated, or ignored. The conditions are selected from a trigger menu that is downloaded from the host VAX cluster. If one of the 32 conditions is met, the detector electronics are read out and sent to Level 2. In addition, the Level 1 framework also handles the prescaling of the Level 1 triggers.

4.3.3 The Level 1 Muon Trigger

Each of the 16694 muon drift cells corresponds to a pad latch bit in the chamber electronics that is set whenever the accumulated charge on the chamber cathode pads exceeds a preset threshold. Module Address Cards (MACs) make this bit information available to the Level 1 trigger. The MACs are kept physically distinct for five separate eta regions (Table 4.3). The MACs take use hit information to form an address (or "centroid"). These centroids represent the z-coordinate of the half-cell of the PDT that was most likely hit. The granularity of the centroids in WAMUS (SAMUS) is 5 cm (1.5cm). At Level 1, the MACs take the logical OR of 3 (4) centroids to form "coarse" centroids in WAMUS (SAMUS).

Name	**η range**
CF	$\|\eta\| < 1.0$
EF-North	$1.0 < \eta < 2.4$
EF-South	$-1.0 < \eta < -2.4$
SAMUS North	$2.4 < \eta < 4.0$
SAMUS South	$-2.4 < \eta < -4.0$

Table 4.3: Regions of the muon system.

This coarse centroid information is sent to Coarse Centroid Trigger (CCT) cards. The CCT logically ORs the coarse centroids by another factor of four, producing a hodoscopic pattern of "cells" that are 12 centroids wide (60 cm). WAMUS muon tracks are formed whenever two or three layers have been hit and are aligned properly. Pattern recognition is performed by the CCTs on logic contained in their EPLDs, programmable logic devices that use EPROM (Erasable Programmable Read-Only Memory) memory cells. One CCT per octant sends tracks to a final summing CCT.

The summing CCTs send trigger decisions to the trigger monitor card (TRGMON) located in the muon supervisor crate. The TRGMON maps the CCT trigger information onto the 16 trigger states. The trigger states are then sent to the Level 1 trigger framework. The muon trigger control computer (MUTCC) receives the trigger mapping from the host VAX cluster and sends it to the TRGMON. The supervisor crate also distributes timing signals from the trigger framework to the MAC, Level 1, and Level 1.5 trigger crates.

4.3.4 The Level 1.5 Muon Trigger

The Level 1.5 muon trigger uses the full centroid resolution of the MACS, allowing sharper momentum cuts on the tracks and better rejection of bad tracks. The MACs strobe their information to Octant Trigger Cards (OTCs) upon receipt of a Level

1 accept. The OTCs use combinations of the A, B, and C layer centroids to form addresses that are used to access their static random access memories (SRAMs). The SRAMs contain patterns used in identifying trigger conditions. These patterns are regional and will be discussed in detail for each region. The OTCs contain a 4×4 array of SRAMs, allowing the OTCs to simultaneously process up to 16 ABC centroid combinations.

Following the SRAM lookup, the centroids associated with good Level 1.5 triggers are used to form another address for an additional set of memories, producing two 24-bit user-defined trigger words. These trigger words are placed into FIFO's for later readout by the Octant Trigger Manager (OTCMGR). The OTCMGR applies a second p_{T}^{μ} cut using the centroids in the trigger words. This design affords the Level 1.5 trigger the flexibility of applying different p_{T}^{μ} thresholds. The OTCMGR produces trigger decision data for each η region and sends it to the TRGMON. The TRGMON translates the trigger decision information into 16 muon trigger states to be used by the trigger framework in the global physics trigger decision. All Level 1.5 trigger decisions and centroid patterns associated with good triggers are written to tape if the event passes Level 2.

4.3.5 Level 2

The Level 2 trigger system consists of 32 micro-VAX 4000-M60 and 16 micro-VAX 4000-M90 worker nodes. Four additional micro-VAX 4000-M60s were used as control nodes that managed the operations of the worker nodes. Level 2 collects Level 1 and Level 1.5 triggers at a rate of roughly 100 Hz and reduces the rate to approximately 2 Hz. To keep dead time at a minimum ($< 5\%$), each node must process an event

within 350 ms.

The Level 2 software is built around collections of algorithms called "tools." Each tool is designed to recognize a specific object or condition within an event. Tools can recognize muons, electrons, photons, jets, taus, scalar and missing E_T, etc. The tools are developed in a VMS environment offline. This environment uses a Level 1 simulator to mimic the behavior of the level 1 hardware. Before using them online, the tools are tested using data and Monte Carlo simulation. Further tests were made during 'shadow runs,' during which a test version of the Level 2 code is loaded into one of the nodes. Data is sent to this node for testing of the new tools, but this node may not participate in trigger decisions.

The triggers and tools are specified by a script file. This file contains the description of 32 Level 1 triggers. Each Level 1 trigger has attached to it at least one Level 2 filter. Each script may include up to 128 Level 2 filters. Each filter consists of various combinations of the tools described above. If an event passes even one of the filters, the event is transferred to the host computer to log and record the event.

CHAPTER 5

DATA SAMPLE SELECTION

The first step in obtaining the b-quark production cross section involves obtaining the differential b-produced muon cross section

$$\frac{d\sigma_b^\mu}{dp_{\rm T}^\mu} = \frac{1}{\Delta\eta\Delta p_{\rm T}^\mu} \cdot \frac{N_\mu^b}{\left(\int \mathcal{L} \cdot dt\right) \cdot \varepsilon}, \tag{5.1}$$

where $\Delta\eta$ is the pseudorapidity region (1.6 units of pseudorapidity for $|\eta^\mu| < 0.8$), $\Delta p_{\rm T}^\mu$ is the bin width in transverse momentum, N_μ^b is the number of muons in the sample determined to have originated from a b quark decay after background subtraction and momentum unsmearing. $\int L \cdot dt$ is the total integrated luminosity for the data sample, and ε is the combined efficiency and acceptances of all muon and jet cuts.

To measure the muon cross section, triggers select events with potentially good muons for analysis. The events are reconstructed and processed into an easily analyzed database format (an ntuple). Offline selection cuts further ensure the quality of the muons and jets in the analyzed events and are designed to enrich the data sample in muons produced by a b-quark decay.

5.1 Data Collection and Processing

The data for this analysis were collected during the December 1995 collider run at Fermilab. During this run, the Tevatron produced $p\bar{p}$ collisions with a center-of-mass energy of $\sqrt{s} = 630$ GeV, corresponding to global run numbers 94874 through 95389. The average instantaneous luminosity was $0.7 \cdot 10^{30}$ crossings/(cm^{2}s) and

never exceeded $3 \cdot 10^{30}$ crossings/(cm^{2}s). Data from runs 95077, 95078, 95080, 95087, and 95296 are excluded from the data sample because their runs have zero recorded luminosity. The total integrated luminosity recorded in the three-week running period was 537 nb^{-1}.

5.1.1 Event Reconstruction

After event information is written to tape, an algorithm processes the raw information, such as hits in the muon chambers and ADC values in the calorimeter, to reconstruct the trajectories and momenta of the products of the $p\bar{p}$ collision. This algorithm, called DØRECO, identifies the tracks and hits in the detector with physics objects (photons, electrons, muons, and jets). The data sample was processed with version 12.21 of DØRECO.

In general, as part of the reconstruction procedure, events are written to various streams based on their characteristics. Each stream is enriched in events consistent with a particular type of analysis. The ALL stream is the master stream, containing every event written to tape. In the low energy run, only a single data stream, dubbed the LNR stream, was written to tape.

5.2 Trigger Requirement

Each event in this analysis is acquired with the MU_1_CENT_LNR trigger. This trigger was defined in the global trigger list in the following way:

trig_bit mu_1_cent-lnr spec_trig spec_trig_3 prescale 100000

terms beam & good beam & mu (1, y1) & mu_scint;

filt_bit mu_1_cent-lnr pass_1_of 5000

filters l2mu(1,9,3,mq_best,cal_confirm,l2_scint,mu_track_y1);

This definition requires that the Level 0 hodoscopes fired and that there was no Main Ring veto. In addition, at Level 1, the trigger requires a single central muon without a scintillator veto.

At Level 2, the muon found is required to be of the highest quality, with confirming energy deposition in the calorimeter along the muon track. The "l2_scint" requirement indicates the state of scintillator confirmation. In this trigger, the cosmic rejection is turned off, but a scintillator along the muon track must have fired. The final Level 2 filter condition requires a muon track at Level 1.0.

5.3 Offline Muon ID and Event Selection

After the events are written to tape, further cuts are imposed to enrich the sample in signal muons while rejecting as much noise and background as possible. The cuts generally can be categorized into muon quality cuts, kinematic and fiducial volume cuts, and associated jet cuts. Scintillator cuts are introduced separately to emphasize the rejection of cosmic ray muons obtained with these cuts. All cuts and their effects are shown in Table 5.1.

5.3.1 Muon Quality Cuts

The trigger system provides very loose muon quality cuts to increase bandwidth in the trigger system. Because the trigger must operate very swiftly, however, offline quality cuts are required to remove noise and spurious hits that get reconstructed as

Cut	Cut Definition	N_μ after cut
Number of muons		88470
Kinematic cut	$3\ \mathrm{GeV/c} < p_T^\mu < 30\ \mathrm{GeV/c}$	83008
Pseudorapidity cut	$\lvert\eta\rvert < 0.8$	68511
Fiducial Volume	$50^\circ < \phi^\mu < 130^\circ$	31883
Trigger	MU_1_CENT_LNR = 1	27948
Muon Quality Cuts		
Flag word	IFW4 ≤ 1	27948
Hadronic fraction	HFRAC = 1	21592
MIP confirmation	ECAL1 > 1 GeV	18935
Momentum kick	$\int \mathrm{B}\cdot\mathrm{dl} > 0.6$ GeV/c	18781
Scintillator Cuts		
Scintillator flag	SCINT = 1	17784
Delta time-of-flight	$\lvert\Delta T_{tof}\rvert \leq 15$ ns	11765
Associated Jet Cuts		
Jet energy	$E_T^{jet} \geq 12$ GeV	1288
μ - jet distance	$\Delta R \leq 0.7$	1241

Table 5.1: The list of selection cuts and their effects.

muons.

Muon Track Quality Flag

Each track reconstructed from muon chamber hits is assigned a "quality of fit" flag. Hits in the muon system are fit to two straight lines that meet in the center of the iron toroid, where the path of the muon is bent by the toroidal field. Routines in the reconstruction algorithms select tracks based on the residuals of the fit, effectively providing a very loose ($\chi^2 \leq 500$) selection. The value of the flag, IFW4, is incremented by one for each of the following criteria that are not satisfied:

- Good fit in the non-bend direction
- Good fit in the bend direction
- Good fit to the vertex in the non-bend direction

- Good fit to the vertex in the bend direction

Requiring IFW4 ≤ 1 reduces contamination of the sample due to cosmic ray muons and reconstructed noise by requiring at least three of the four above conditions are satisfied.

Muon Minimum Ionizing Energy Deposition

Muons produced at the interaction vertex deposit an energy in the calorimeter consistent with a minimum ionizing particle (MIP). Tracks that are not consistent with this energy deposition are likely to be cosmic ray muons or tracks reconstructed from noise. For candidate muons, the energy deposited in each calorimeter cell along the muon track is added with the energy of the nearest neighboring cell. The summed energy, ECAL1, is required to exceed 1.0 GeV.

Hadronic Fraction

The fraction of coarse hadronic calorimeter layers exhibiting energy deposition along the reconstructed muon track is denoted HFRAC. All four layers are required to contain energy, corresponding to HFRAC = 1.

Momentum Kick

The integral $\int \mathrm{B} \cdot \mathrm{dl}$ is calculated. The value of this integral must exceed 0.6 GeV/c to ensure good muon momentum measurement and avoid the edges of the iron toroid where the magnetic field map is less accurate.

Bin Number	p_{T}^{μ} range (GeV/c)
1	3.0 - 3.5
2	3.5 - 4.0
3	4.0 - 4.5
4	4.5 - 5.5
5	5.5 - 6.5
6	6.5 - 9.0
7	9.0 - 12.0
8	12.0 - 15.0
9	15.0 - 30.0

Table 5.2: Transverse momentum ranges as a function of bin number.

5.3.2 Kinematic and Fiducial Cuts

The muons used in this analysis are required to have a transverse momentum between 3 and 30 GeV/c. Muons with transverse momenta less than 3 GeV/c are not energetic enough to pass through the iron toriod in the central muon system. The muon momentum from the PMUO bank is used when the global fit used a central detector (CD) track. If no good CD match was found, a point in the calorimeter was used and the correct muon momentum is obtained from the MUOT bank.

The bins of muon transverse momentum are shown in Table 5.2. The bins were chosen so that approximately the same number of muons are found in each bin before background subtraction to keep the statistical error approximately the same across all bins. While muons below 4 GeV/c generally do not make it through the central iron toroid with a reliable momentum measurement, they are included for purposes of momentum distribution unsmearing, as is the low statistics bin between 15 and 30 GeV/c.

The muons are required to be in the central region ($|\eta^{\mu}| \leq 0.8$). The muon tracking chambers in the central region suffered from a buildup on the anode wire due to the

outgassing of material in the chambers. The source of the buildup was the vapor of the "Glas-Steel" polyester-epoxy resin of the cathode pad. This buildup decreased the efficiency of muon detection significantly. Running high current through the anode wires, a process called "zapping," [41] removed the buildup from the wires. Not all chambers were zapped prior to the 630 GeV running. Instead, the zapping occured only for alternating B and C layer chambers on the sides of the detector. Muons used in this analysis, therefore, are constrained to the fiducial region $50^\circ < \phi^\mu < 130^\circ$, because muon chambers on the sides and bottom of the detector have efficiencies that are not well understood. Because b-quark production is isotropic, the number of muons can be scaled by a factor of 4.5 to account for this acceptance in ϕ.

5.3.3 Scintillator Cuts

The cosmic cap scintillators installed during Run 1B provide a powerful tool for reducing cosmic ray muon background. The reconstructed muon track must point to a scintillator that fired, and the timing information for the scintillator that fired must be available (in our ntuples, this requirement corresponds to SCINT=1). Further, the expected time of flight is subtracted from the measured time of flight to obtain $\Delta \mathrm{T}_{tof}$. Signal events should exhibit $\Delta \mathrm{T}_{tof}$ values that lie within a gaussian peak around 0 ns. Because the passage through the detector of a cosmic ray muon is not correlated with beam crossing times, the cosmic background is flat in $\Delta \mathrm{T}_{tof}$ for $\Delta \mathrm{T}_{tof}$ values in the interval [-20, 40 ns]. Requiring $|\Delta \mathrm{T}_{tof}| \leq 15$ ns removes a great deal of cosmic ray contamination from the sample, and the remainder can be estimated as a function of muon transverse momentum. See Section 6.1 for more detailed information on the cosmic ray muon background subtraction.

5.3.4 Associated Jet Requirement

While the scintillator cuts reduce the amount of cosmic background, requiring the association of each muon to a nearby jet provides more powerful background reduction in two ways. First, the fraction of cosmic ray muons in the muon plus jets sample as a function of p_{T}^{μ} is lower than that found in the inclusive muon data sample. Second, muons coming from direct b-quark decays exhibit a very different $p_{\mathrm{T}}^{\mathrm{rel}}$ distribution from those resulting from direct charm, pion, or kaon decays. The variable $p_{\mathrm{T}}^{\mathrm{rel}}$ is defined as the component of the muon momentum perpendicular to the associated jet axis and is the variable that allows us to separate our b-quark signal from background. The use of $p_{\mathrm{T}}^{\mathrm{rel}}$ to extract the fraction of muons from bottom decays is detailed in Section 6.2.

Jet Finding Algorithm

The definition of a jet used in this analysis is the summation of energy deposited in the calorimeter within a cone in η-ϕ space of radius

$$\Delta \mathrm{R} = \sqrt{(\Delta\eta)^2 + (\Delta\phi)^2} = 0.7. \tag{5.2}$$

Reconstruction of jets found in the DØ calorimeter begins with a list of measured values of transverse energy found in each of the calorimeter trigger towers. The trigger towers are projective towers of calorimeter cells that point toward the interaction region at the center of the detector. The segmentation of the trigger towers is generally 0.1×0.1 in $\eta - \phi$, getting slightly larger in the forward regions near the beampipe. The energy in the towers is corrected for the vertex position measured in the central detector.

Jet reconstruction begins by finding pre-clusters, localized energy deposits used as seeds for the iterative reconstruction process. The pre-clusters consist initially of adjacent towers that exhibit transverse energies greater than 1 GeV. The average E_T-weighted coordinate in $\eta - \phi$ is used as the starting coordinate for the jet axis. The reconstruction algorithm then determines the weighted average of all cells within a 0.7 cone around this axis to form a new jet axis. The process repeats until the weighted axis position is found to be the same as in the previous iteration. When all jets in the event have stabilized in this manner, a jet E_T of 8 GeV is required.

After the jets have stabilized, the reconstruction code determines whether the jets must be split or merged by examining the E_T overlap between any two jets. If two jets share more than 50% of their transverse energy, they are merged. Otherwise, the transverse energy is assumed to be from the jet with the closest axis. Two different preclusters found within $\Delta R = 0.1$ are assumed to be identical, and the one with the smaller E_T is removed.

Jet Quality Cuts

A set of quality cuts has been developed to reduce the number of fake jets in the sample. Fake jets come from main ring noise, hot cells in the calorimeter, and bremsstrahlung from cosmic ray muons. The efficiencies of these cuts have been studied extensively. They have been found to range from 96% efficient for 11 GeV jets and 91% efficient for 400 GeV jets. The rejection for fake jets is greater than 95% [42].

Electromagnetic Fraction The fraction of jet E_T in the electromagnetic layer of the calorimeter is required to be less that 0.95. This cut has been determined to be 90% efficient in removing fake jets originating from calorimeter 'hot cells.' Monte Carlo studies suggest that the efficiency for real jets is 99% except for a slight decrease in the region between the central and end calorimeters.

Coarse Hadronic Fraction The fraction of jet E_T in the coarse hadronic layer of the calorimeter is required to be less that 0.5. This cut helps eliminate fake jets originating from Main Ring noise. The Main Ring passes through the coarse hadronic portion of the caloimeter in the top of the detector. This cut is 90% effective at removing fake jets caused by Main Ring activity, and 99% efficient at removing hot cells in the coarse hadronic layer of the calorimeter. For real jets, the efficiency is 99%, except in the crack between the central and end calorimeters (95%).

Hot Cell Ratio The hot cell ratio is defined to be the ratio of the energy in the highest energy cell in a jet to the energy in the second most energetic cell. Real jets are not expected to exhibit large variations in cell energy within a given jet. The hot cell ratio is required to be less than 20 for this analysis. This cut removes fake jets originating from calorimeter noise.

Associated Jet Requirement

The muons in the data sample are required to lie within the jet cone, so the separation in $\eta - \phi$ space between the reconstructed muon track and the jet axis must satisfy $\Delta R \leq 0.7$. The associated jet is required to have a transverse energy $E_T \geq 12$ GeV,

which includes the transverse momentum of the muon. Efficiencies for reconstruction of jets below 12 GeV are not well understood, so they are withdrawn from consideration.

In addition to the cosmic background reduction associated with requiring an associated jet, the requirement also removes nearly all of the Drell-Yan and Υ background, because muons from these processes are generally isolated. It is expected that less than 0.01% of the events in the data sample originate from these processes.

5.3.5 Variable Correlations

Various pieces of this analysis rest on the assumption that certain variables are not strongly correlated. This brief section introduces correlations and presents the correlations between the variables p_{T}^{μ}, p_{T}^{rel}, and E_{T}^{jet}. Further details about correlation and correlated errors are shown in Appendix B.

The correlation ρ_{XY} between two variables X and Y is given by the expression

$$\rho_{XY} = \frac{\sigma_{XY}}{\sigma_X \cdot \sigma_Y}, \tag{5.3}$$

where σ_{XY} is the covariance between X and Y, defined by

$$\sigma_{XY} = \overline{X \cdot Y} - \overline{X} \cdot \overline{Y}. \tag{5.4}$$

Here, $\overline{X}$ is the average value of a variable X. In the expression for the correlation above, σ_X is the square root of the variance of the variable X, calculated by

$$\sigma_X^2 = \overline{X^2} - \left(\overline{X}\right)^2.$$

Correlation can be understood as a normalized covariance between two variables, constrained to lie in the interval $[-1, 1]$. If $\rho_{XY} = 1$, the variables X and Y are said

	p_{T}^{μ}	p_{T}^{rel}	E_{T}^{jet}
p_{T}^{μ}	1	.241	.0821
p_{T}^{rel}	.241	1	.0827
E_{T}^{jet}	.0821	.0827	1

Table 5.3: Correlations between three variables used in this analysis.

to be completely correlated, indicating that an increase of 1σ in the value of variable X requires an increase of 1σ in the value of variable Y. Completely anti-correlated variables ($\rho_{XY} = -1$) have the property that an increase of 1σ in the value of variable X requires a decrease of 1σ in the value of variable Y. Pairs of variables with $\rho_{XY} = 0$ are uncorrelated.

Table 5.3 shows the correlations between variables in the selected muons plus jets data sample. Note that this is not a proper full correlation matrix; each pair of variables was considered independently, using the prescription above.

The table shows that all pairs of variables are positively correlated. E_{T}^{jet}, however, is not significantly correlated with either variable. The variables p_{T}^{μ} and p_{T}^{rel} are more stongly correlated, although .25 is not a strong correlation. The consequences of this slight correlation are discussed in the next chapter.

5.3.6 Sample Events

A total of 1241 events pass all selection cuts in the muon sample. In general, the analysis is performed using raw event information, but it is often useful to use an event viewer to scan events. Event displays can help identify problems in the reconstruction algorithms and offer a method of seeing what is occurring an the event.

Figures 5.1 and 5.2 depict two sample events from the selected data sample. In the event displays, the muon track traversing the muon system is evident, as well as the

bending of its path in the center of the iron toroid. In addition, the energy deposition in the calorimeter indicates the presence of a low energy jet associated with the muon. The detector is shown in profile from the side, and the muon is traversing the top of the detector.

5.3.7 Comparison with Monte Carlo

Because this analysis relies on fully reconstructed ISAJET Monte carlo for the shapes of the input distributions for background subtraction, and on the relative contribution of sequential to direct bottom decays, we must briefly compare the selected data to the Monte Carlo Samples used. Figures 5.3 through 5.5 compare the selected data to ISAJET MC (RIO sets 3 and 4 with the FNAL π/K sample added). The distributions in the figures are shown normalized to one another.

Because the muon transverse momentum shapes do not agree, we first obtain the measured muon cross section as a function of true muon transverse momentum (obtained later in this note). The raw ISAJET p_{T}^{μ} is also obtained for bottom quark decays as a function of generated transverse momentum. A ratio of the two distributions is used to obtain weights as a function of real p_{T}^{μ}. Each reconstructed muon in the ISAJET sample, is given a weight based on the transverse momentum of its associated generated muon. The new reconstructed p_{T}^{μ} spectrum agrees well with the measured data sample (Figure 5.6). The new weighting scheme does not significantly alter either the E_{T}^{jet} or the p_{T}^{rel} distributions.

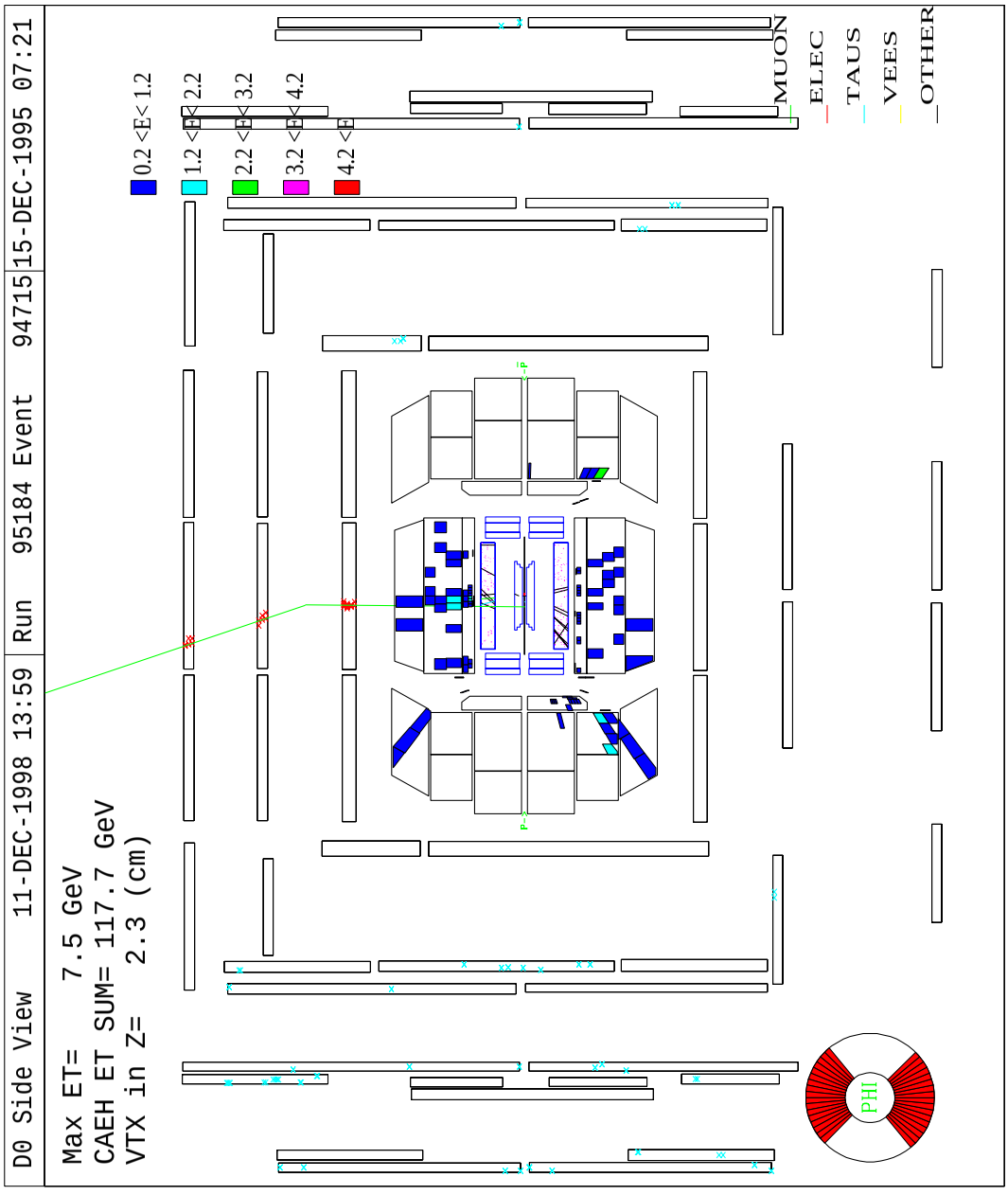

Figure 5.1: Event 94715 from Run 95184.

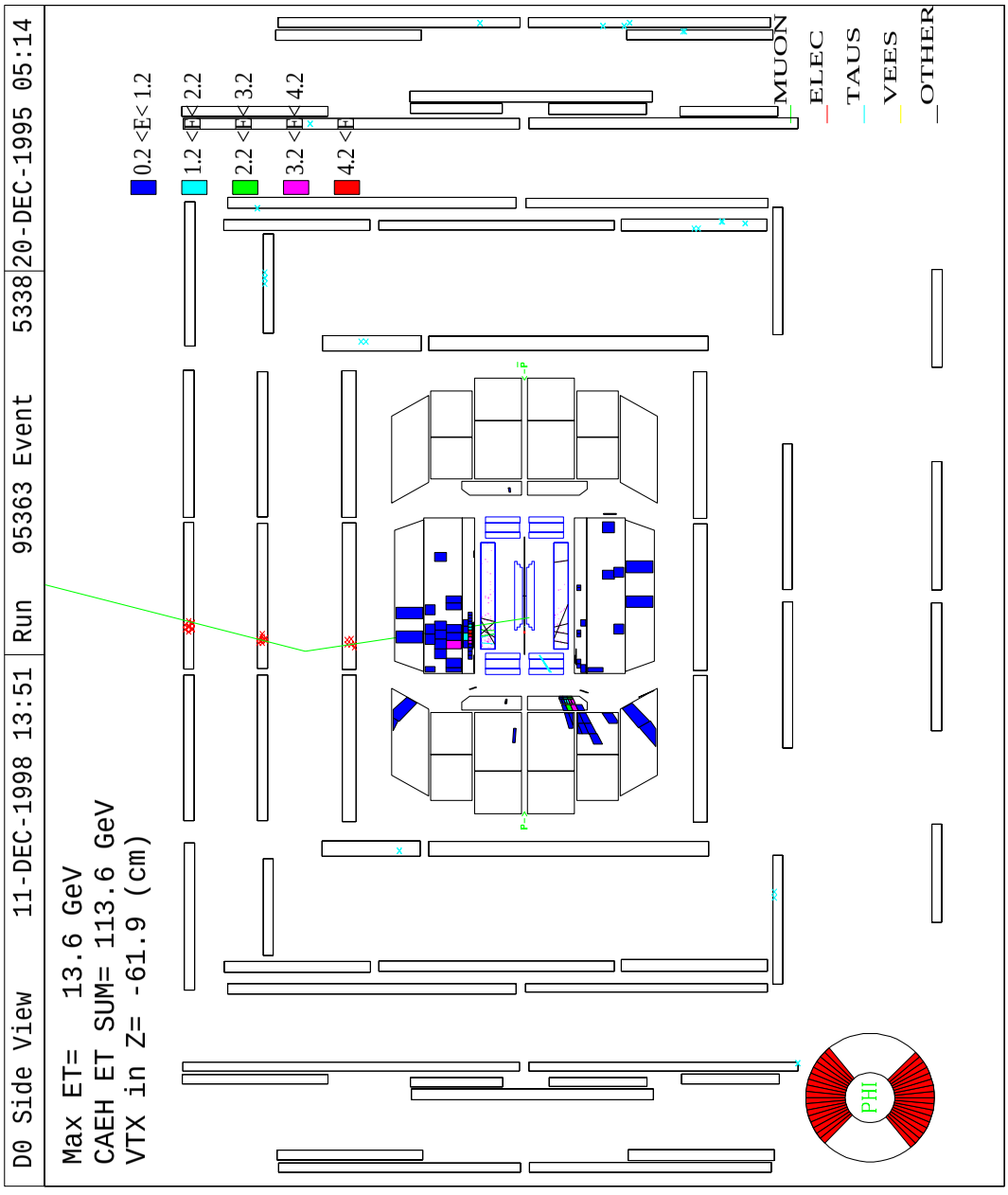

Figure 5.2: Event 5338 from Run 95363.

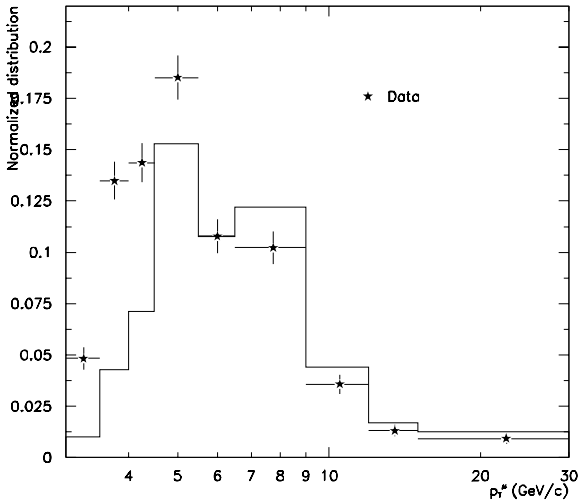

Figure 5.3: The muon transverse momentum spectrum from fully weighted, selected ISAJET events (histogram) compared to selected data events (stars).

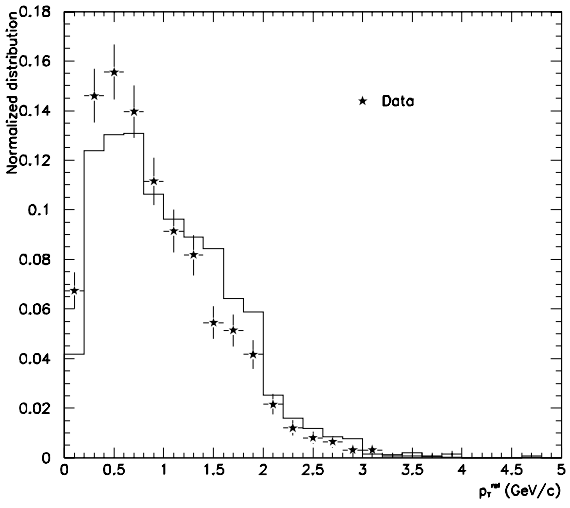

Figure 5.4: The spectrum of muon transverse momentum relative to the associated jet axis from fully weighted, selected ISAJET events (histogram) compared to selected data events (stars).

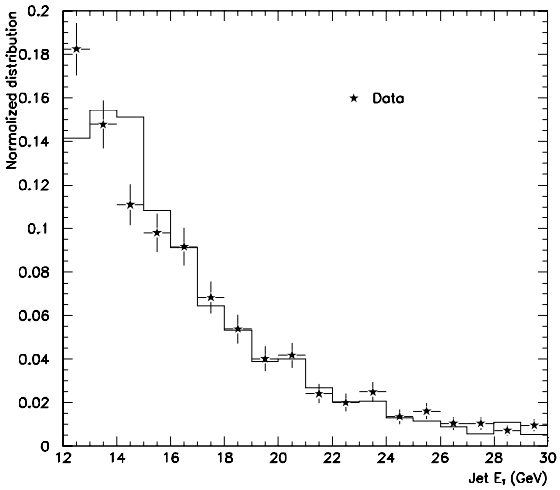

Figure 5.5: The jet transverse energy spectrum from fully weighted, selected ISAJET events (histogram) compared to selected data events (stars).

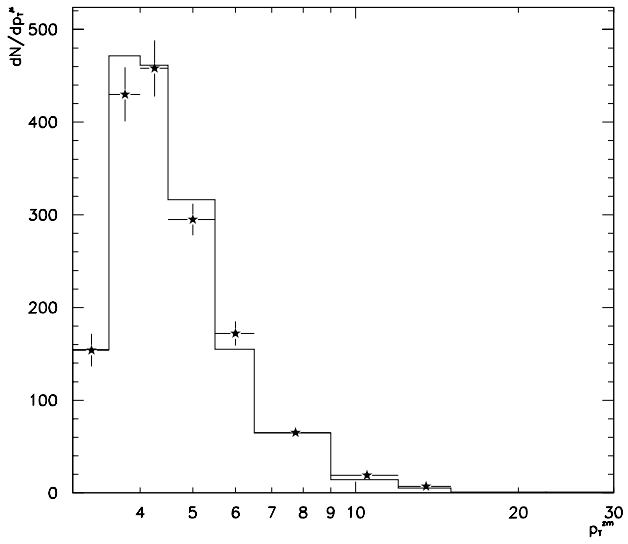

Figure 5.6: Reweighting the Monte Carlo provides considerably better agreement between data and Monte Carlo.

5.3.8 Cut Efficiencies

All requirements placed on the data set result in a loss of a portion of the b-produced muon cross section. To obtain the true cross section, corrections must be applied to the data to recover the lost muons. Because the efficiencies are applied after unfolding the data (Chapter 7), the efficiencies are determined as a function of true muon transverse momentum.

These corrections are represented in the expression for the b-produced muon cross section (Eq. 5.1) as

$$\varepsilon = \varepsilon_{reco} \cdot \varepsilon_{trig} \cdot \varepsilon_{\mu} \cdot \varepsilon_{jet}, \tag{5.5}$$

where ε_{reco} represents the reconstruction efficiency, ε_{trig} represents the trigger efficiency, ε_{μ} denotes the muon quality cut efficiency, and ε_{jet} represents the efficiency and acceptance of requiring a good jet within $\Delta R \leq 0.7$. All efficiencies are obtained for muons coming from direct and sequential bottom quark decay only. The manner in which these efficiencies were obtained is described below, and the values of the efficiencies are summarized in Table 5.4.

Muon Trigger Efficiency

Using Rio Monte Carlo sets 3 and 4 (see Section 3.3), each event containing one muon was selected. From this distribution, the fraction of the events that satisfied the trigger bit representing MU_1_CENT_LNR is considered to be the muon trigger efficiency. Because the trigger bit comes from Level 2, this efficiency represents the total L1·L2 trigger efficiency. To smooth out the efficiency correction, a hyperbolic

tangent with the functional form

$$\varepsilon_{trig} = p_1 \cdot \tanh\left(p_2 \cdot p_{\mathrm{T}}^{\mu} + p_3\right) \tag{5.6}$$

was fit to the Monte Carlo points. The resulting function, evaluated at the bin centers, was used as the trigger efficiency correction to the data. The original points and the fit are shown in Figure 5.7. The error band on the function results from the error on the fit parameters calculated within MINUIT. A more explicit calculation of the error determination may be found in Section B.3.

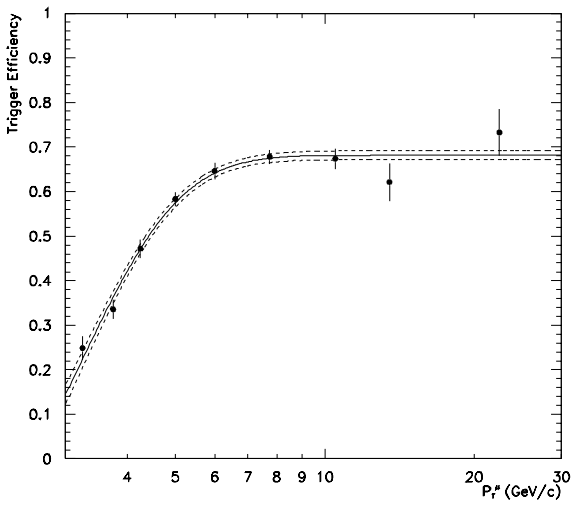

Figure 5.7: A hyperbolic tangent fit to the Monte Carlo. The error band is the statistical error on the function due to parameter errors from MINUIT. The trigger efficiency is obtained as a function of real muon transverse momentum.

To cross-check the trigger efficiency from the Monte Carlo, data events containing a reconstructed muon satisfying any non-muon trigger were selected to obtain an unbiased sample of muons. Then the total L1·L2 muon trigger was required and the efficiency computed by taking the ratio of muons passing the trigger to those in the unbiased sample as a function of muon transverse momentum. The Monte Carlo

efficiency is recomputed as a function of reconstructed muon transverse momentum. Agreement within errors between the data and Monte Carlo efficiencies as a function of reconstructed transverse momentum is shown in Fig. 5.8.

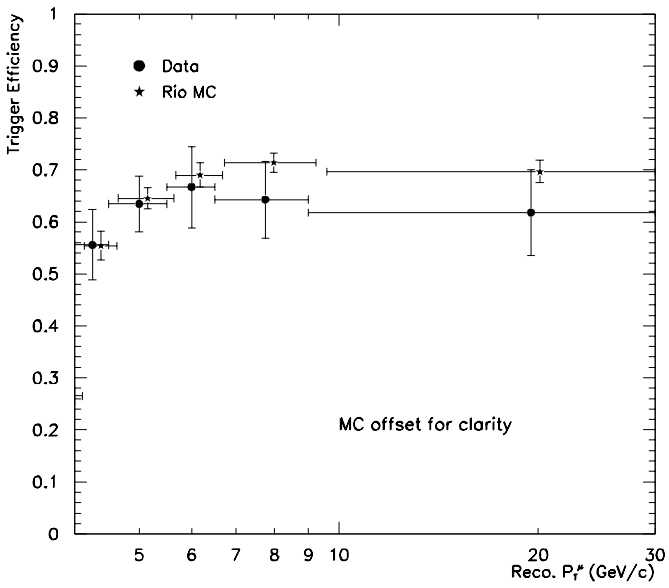

Figure 5.8: The combined Level 1 and Level 2 trigger efficiency in both the data and the Monte Carlo.

Muon Reconstruction Efficiency

The muon reconstruction efficiency is the probability that a real muon passing through the muon system will be reconstructed after firing the combined L1·L2 trigger. Using the Rio Monte Carlo sets 3 and 4, processed with DØRECO, the reconstruction efficiency is obtained as a function of p_{T}^{μ} by taking a ratio of the number of muons reconstructed to those generated within ISAJET. The efficiency of reconstruction is roughly 96%, and the values used in the calculation of the total efficiency are given in Table 5.4.

Muon Quality Cut Efficiency

To obtain the muon quality cut efficiency, the transverse momentum spectrum is plotted for muons from Rio Monte Carlo sets 3 and 4 and the FNAL π/K Monte Carlo set that satisfied reconstruction and trigger requirements. The muon quality cuts were applied and a new p_{T}^{μ} spectrum was plotted. The ratio between the two distributions is taken to be the muon quality cut efficiency. The values used in the calculation of the total efficiency are also given in Table 5.4.

Associated Jet Requirement

The correction to the muon transverse momentum spectrum due to the associated jet requirement is large, a combination of both jet acceptances and inefficiencies associated with jet reconstruction and identification. This correction will be referred to here as the associated jet cut efficiency.

Muons coming from bottom quarks are mostly lost due to the efficiency of finding a jet with a transverse energy greater than 12 GeV. Figure 5.9 demonstrates that a ΔR_{min} cut at 0.7 does not eliiminate a significant fraction of the muons, but a cut on the jet transverse energy does. In addition, the associated jet cut efficiency is similar across all muon transverse momenta, borne out in Figure 5.10. In Figure 5.10, the data sample has been divided roughly in half. The histogram represents the associated jet transverse energy for muons with a low transverse momentum, while the stars represent the associated jet E_T for muons with a high transverse momentum. The plot also confirms the lack of correlation between the two variables (computed in Section 5.3.5).

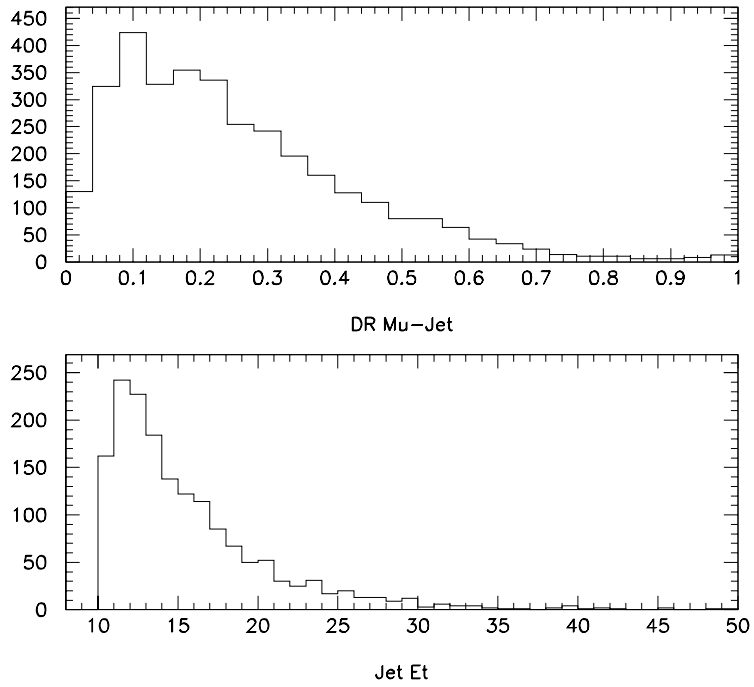

Figure 5.9: The $\Delta R_{\rm min}$ and E_T^{jet} distributions in the data.

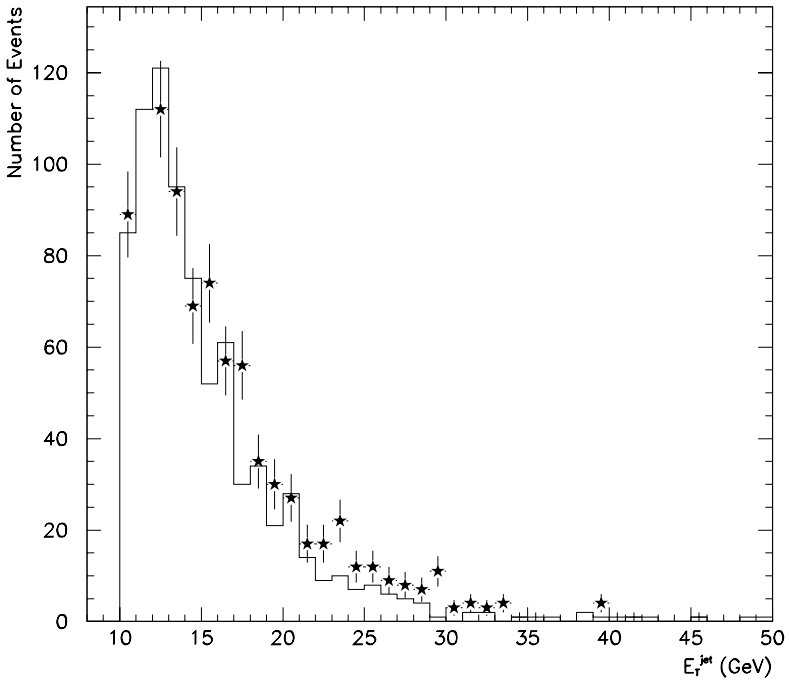

Figure 5.10: The muon plus jet data sample is divided roughly in half, and the associated jet transverse energy is plotted. The histogram represents the lower p_T^μ bin, and the stars represent the upper p_T^μ bin.

The associated jet cut efficiency was obtained from Monte Carlo. In three independent ISAJET samples, muons with an associated jet were selected from a base sample of muons passing reconstruction, trigger, and quality requirements. The ratio for the spectrum of muons with associated jets to the spectrum of reconstructed, triggered muons was taken. The samples chosen were IND Set 1, IND Set 2, and a combination of Rio Sets 3 and 4. The evaluated points are shown in Fig. 5.11. The results of the computation agree within Monte Carlo statistical errors over the transverse momentum interval of interest (between 4 and 15 GeV/c).

To obtain the associated jet cut efficiency used to compute the b-produced muon cross section, we take a weighted average of the results of the three samples. The result of the weighted average is shown in Fig. 5.12. For details on the weighted average computation, see Appendix B.

Scintillator Cut Efficiency

The 15ns scintillator timing window was chosen to remove some cosmic ray muon background while retaining all of the data. The scintillator cuts are over 98% efficient for data, where the inefficiency results from muons slipping through cracks in the scintillator coverage. The rest of the cosmic background subtraction is explained in Section 6.1.

Uncertainties on the Efficiencies

The muon trigger and the jet reconstruction corrections are both obtained using fully reconstructed Monte Carlo. The trigger efficiency, obtained using ISAJET events as a function of true muon transverse momentum, was fit with a hyperbolic tangent. The

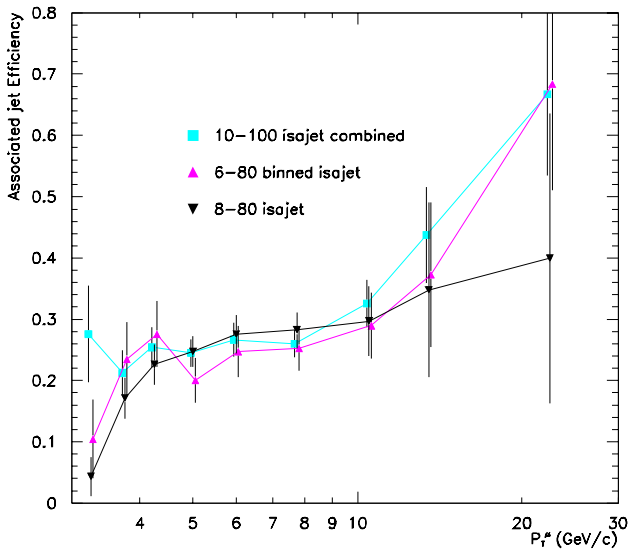

Figure 5.11: The associated jet cut efficiency for three independent Monte Carlo samples (shown offset for clarity). The values are consistent within errors over the region of interest ($4 < p_T^{\mu} < 15$ GeV/c).

fit error is taken to be the uncertainty on the correction and is included in the error on the trigger correction shown in Fig. 5.12.

The associated jet correction is evaluated using three samples of Monte Carlo as described above. Part of the uncertainty on the jet correction is taken to be the statistical error on the weighted average of the efficiencies combined in quadrature with half the maximum spread of the values from the three samples.

In addition to the uncertainty on the jet cut efficiency due to the weighted average calculation, jet finding efficiencies were compared for samples of ISAJET and PYTHIA Monte Carlo events. The Monte Carlo event generator PYTHIA was chosen because it handles the particle fragmentation and jet production differently [43]. A 5% uncertainty [44], flat in muon transverse momentum, is included in the associated

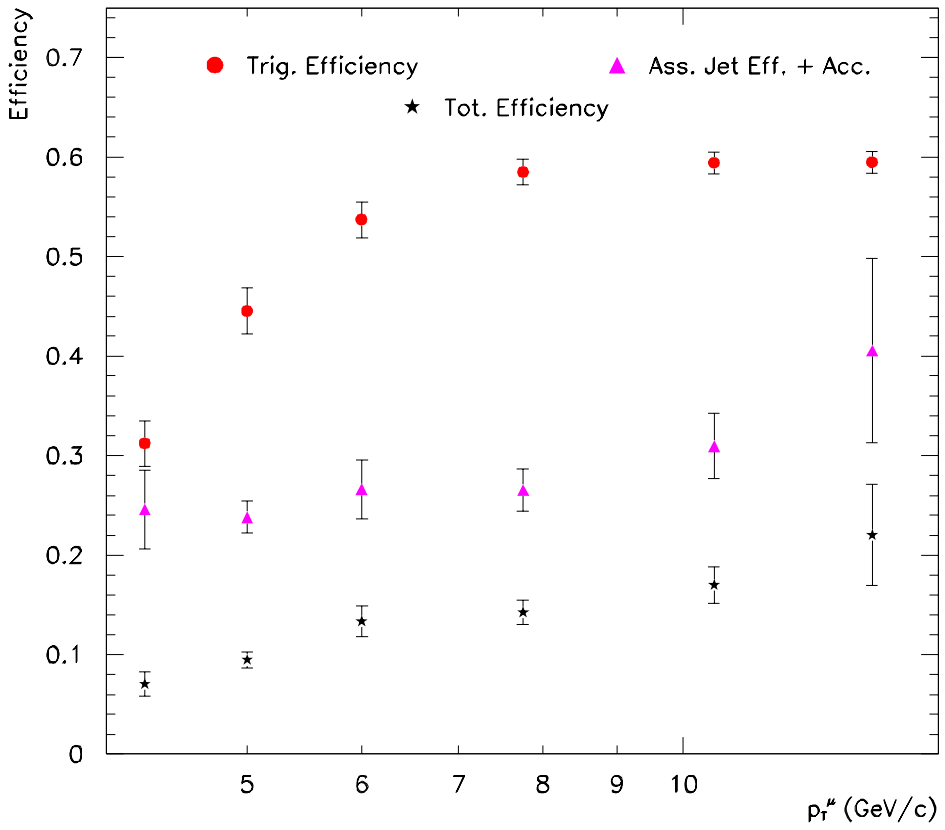

Figure 5.12: Cut efficiencies as a function of muon transverse momentum. The stars represent the final correction to the data. Not shown in the figure are the reconstruction and quality cut efficiencies (∼95%). The fiducial volume correction is not included here. The stars represent the total correction to the data.

p_T^μ (GeV/c)	μ Reco	μ Trigger	μ Quality	Jet Corr.	Total Corr.
$4 - 4.5$	$.95 \pm .01$	$.31 \pm .02$	$.96 \pm .01$	$.25 \pm .04$	$.070 \pm .013$
$4.5 - 5.5$	$.96 \pm .01$	$.44 \pm .02$	$.92 \pm .01$	$.24 \pm .02$	$.094 \pm .009$
$5.5 - 6.5$	$.97 \pm .01$	$.54 \pm .02$	$.96 \pm .01$	$.27 \pm .03$	$.13 \pm .017$
$6.5 - 9$	$.97 \pm .01$	$.58 \pm .01$	$.95 \pm .01$	$.27 \pm .03$	$.14 \pm .014$
$9 - 12$	$.97 \pm .01$	$.59 \pm .01$	$.95 \pm .01$	$.31 \pm .04$	$.17 \pm .020$
$12 - 15$	$.96 \pm .02$	$.59 \pm .01$	$.95 \pm .02$	$.41 \pm .09$	$.22 \pm .052$

Table 5.4: The contributions to the total efficiency as a function of muon transverse momentum with associated uncertainties.

jet cut efficiency to account for potential Monte Carlo generator dependence.

In the inclusive muon analysis at $\sqrt{s} = 630$ GeV [45], the muon cut efficiencies were found to be systematically consistent with the data to within a few percent. Uncertainties on the order of 2-3% were introduced for the hadronic fraction and scintillator cuts (HFRAC = 1 and the SCINT = 1 cuts).

The total efficiency correction is the product of the individual efficiencies (Eq. 5.5). The total error is given as the sum in quadrature of the relative error on each correction. The efficiencies and uncertainties used to correct the cross section as a function of muon transverse momentum bin are shown in Table 5.4.

With the sample of candidate muons chosen and the efficiencies for the selection criteria, it remains to determine the fraction of the sample muons originating from the decay of a bottom quark. The next chapter presents the techniques used to extract the b-quark produced muon signal from the selected data sample.

CHAPTER 6

SEPARATION OF SIGNAL FROM BACKGROUND

To obtain the b-produced muon cross section, the fraction of the muons in the data sample originating from the decay of a b-quark must be determined. Backgrounds to this signal include muons originating in cosmic ray showers, primary charm quark decays, and π/K in-flight decays. A fit to scintillator timing information permits an estimation of the level of cosmic ray contamination in the sample, while a fit to the data in the variable $p_{\mathrm{T}}^{\mathrm{rel}}$ enables an estimation of the fraction of the muons in the sample coming from bottom decays. The number of b-produced muons $\left(N_{\mu}^{b}\right)$ in the data sample per muon transverse momentum bin is given by

$$N_{\mu}^{b} = N_{\mu} \cdot f_{NC} \cdot f_{b}, \tag{6.1}$$

where N_{μ} is the raw number of measured muons, f_{NC} is the fraction of non-cosmic muons, and f_b is the fraction of bottom-produced muons in the data sample.

6.1 Estimation of the Cosmic Ray Muon Background

Energetic particles incident upon the earth create showers of particles in the upper atmosphere. These showers predominantly produce low mass mesons, specifically pions (π) and kaons (K). Charged pion and kaon decays have a very high probability of decaying to a muon, making the muon the most copiously produced charged particle from cosmic ray interactions.

At sea level, muons coming from cosmic ray interactions follow a $\cos^2\theta$ distribution, where θ is the zenith angle at production, with a mean energy of roughly 2

GeV. If a cosmic ray muon is nearly vertically incident on the top of the detector, then, it may pass the minimum p_{T}^{μ} cut of 3 GeV/c and contaminate the muon data sample. While muon quality and associated jet cuts can remove much of the contamination due to cosmic ray muons, a small fraction remains that must be estimated as a function of muon transverse momentum.

The cosmic cap scintillators (see Section 4.2.3) provide the most powerful tool for estimating the background due to cosmic ray muons. The time of flight of the muon is obtained using the difference between the beam crossing time and the time the scintillator fired. Given the measured time-of-flight and the expected time-of-flight, the $\Delta \mathrm{T}_{tof} = T_{tof}^{\mathrm{meas}} - T_{tof}^{\mathrm{exp}}$, or "delta time-of-flight," can be computed.

Previous results from an analysis of time-of-flight data with a larger muon sample [45] suggest that because cosmic ray muon arrival times are not correlated with beam crossings, their $\Delta \mathrm{T}_{tof}$ distribution is flat within the interval [-20, 40] ns, while signal muons exhibit a gaussian $\Delta \mathrm{T}_{tof}$ distribution (Figure 6.1). Figure 6.2 shows the $\Delta \mathrm{T}_{tof}$ distribution in the selected data sample for this analysis. Note that the requirement of an associated jet reduces the fraction of cosmic ray muons in the sample. Also shown in Figure 6.2 is the 15 ns cut and a sample log-likelihood fit of a gaussian plus a constant to the distribution.

The single muon analysis suggests that the fraction of muons originating from cosmic rays increases as a function of muon p_{T}, so the cosmic ray muon fraction is estimated independently for each p_{T}^{μ} bin. The $\Delta \mathrm{T}_{tof}$ distribution between -20 and 40 ns is plotted for each bin, and the number of cosmic ray muons within the 15 ns window is estimated by fitting the distributions with a gaussian plus a constant; the number of cosmic ray muons is then simply the value of the constant times the width

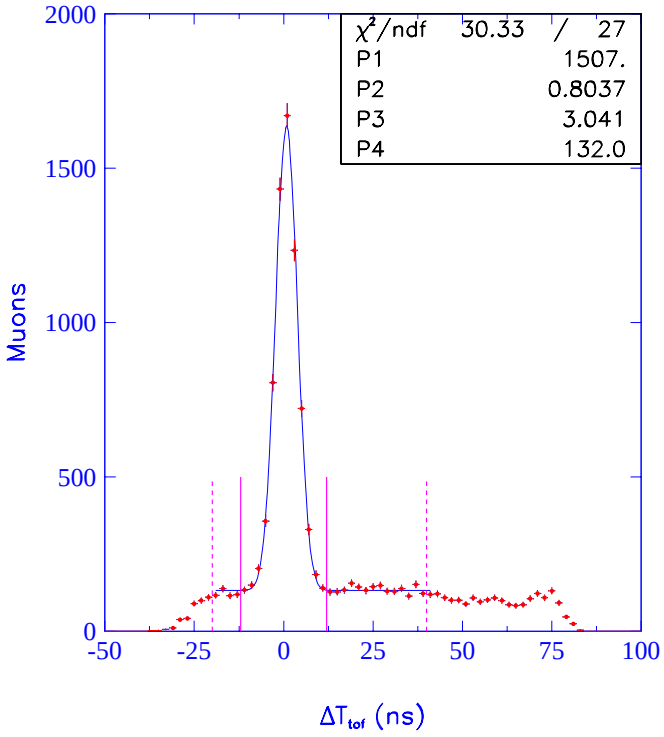

Figure 6.1: A fit of a gaussian plus a constant to the ΔT_{tof} distribution over the interval [-20, 40 ns] for the inclusive muons data sample.

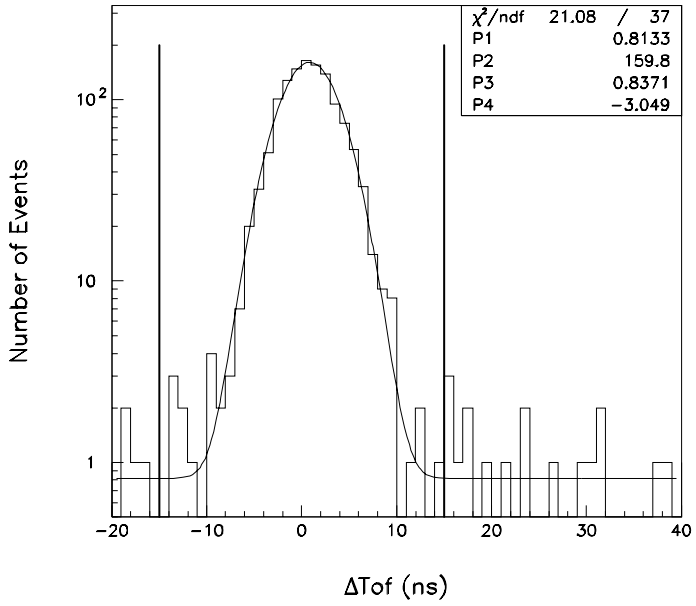

Figure 6.2: The scintillator timing distribution in the data sample. Also shown is a fit of a gaussian plus a constant to the data and the 15 ns cut used to select events.

of the window in ns. The fits to all muon transverse momentum bins are shown in Figures 6.3 and 6.4.

Figure 6.5 shows the results of the ΔT_{tof} fits as a function of muon transverse momentum. Also shown in Figure 6.5 is a fit to the cosmic ray muon fraction found in each bin. The last two bins have been combined to avoid low statistics in the 15-30 GeV/c bin. The functional form employed in the fit is

$$f_{\cos} = e^{a_1 + a_2 p_{\mathrm{T}}^{\mu}}. \tag{6.2}$$

The errors band represents the error on the fit only. The correction applied to the data is the fraction of non-cosmic ray muons in the sample, obtained by

$$f_{NC} = 1 - f_{\cos}, \tag{6.3}$$

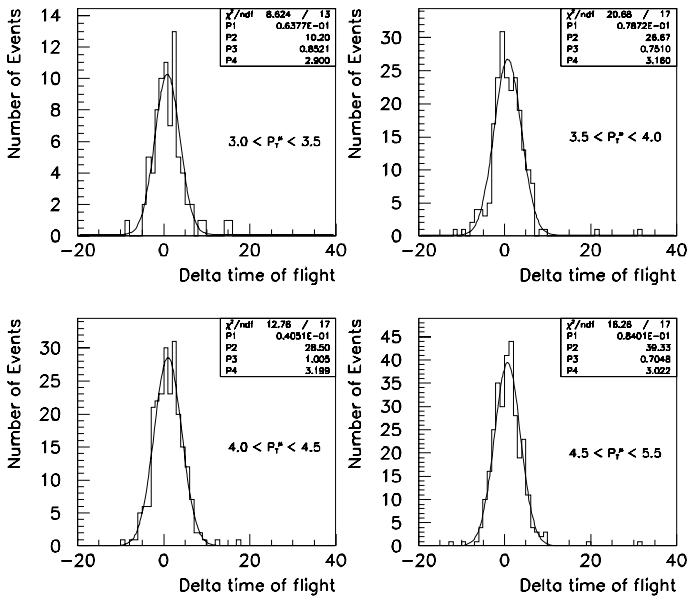

Figure 6.3: The scintillator timing information fit with a gaussian plus a constant for the first four bins of muon transverse momentum.

where $f_{\cos}$ is the value of the fitted function at the center of the muon transverse momentum bin. The values of f_{NC} used to compute the bottom produced muon cross section are given in Table 6.1.

6.2 Obtaining the *b*-Fraction in the Data

To determine the b-quark cross section, first the fraction of muons in the sample that originate from the decay of a bottom quark (f_b) must be determined. Two mechanisms of b-quark decay contribute significantly to the total muon cross section. The first mechanism, denoted *b primary decay*, occurs when a bottom quark decays to a W boson and a charm quark, and the W subsequently decays to a muon and a muon neutrino. In the second mechanism, *b sequential decay*, a bottom quark decays

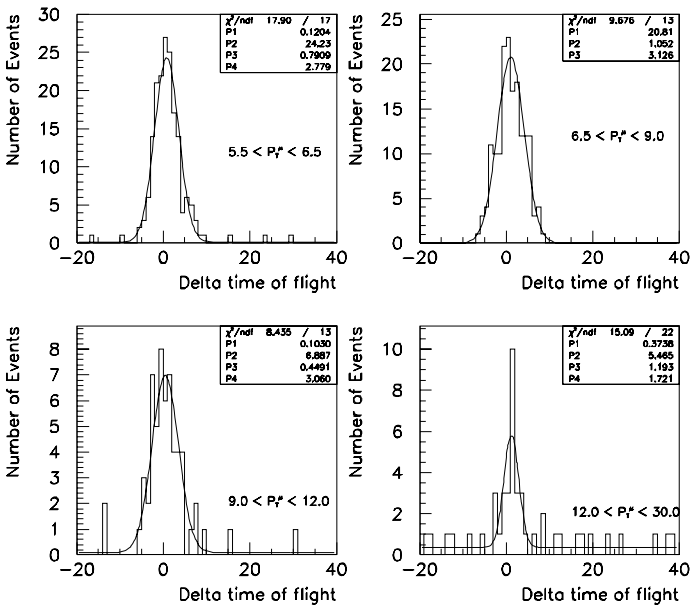

Figure 6.4: The scintillator timing information fit with a gaussian plus a constant for the last four bins of muon transverse momentum. The last two bins are combined because statistics are poor in the 15-30 GeV/c bin.

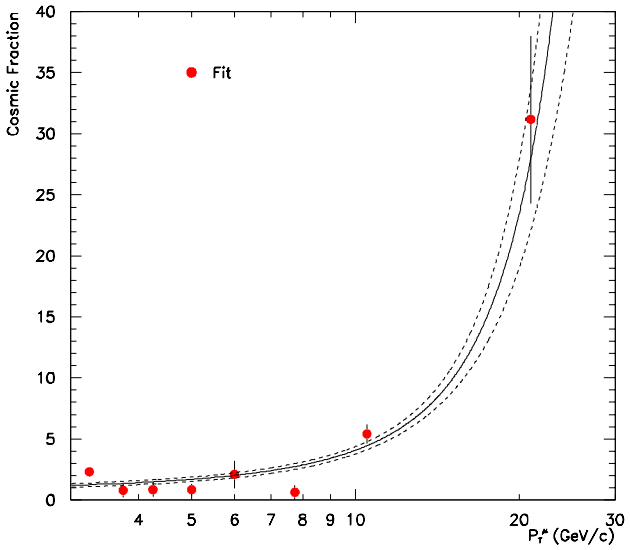

Figure 6.5: The cosmic ray muon fraction estimated using a fit to the scintillator timing information as a function of muon transverse momentum.

p_{T}^{μ} (GeV/c)	f_{NC}
$4 - 4.5$	$.99 \pm .002$
$4.5 - 5.5$	$.98 \pm .002$
$5.5 - 6.5$	$.98 \pm .003$
$6.5 - 9$	$.97 \pm .003$
$9 - 12$	$.96 \pm .004$
$12 - 15$	$.92 \pm .007$

Table 6.1: The fraction of muons from non-cosmic sources and associated uncertainty for the bins used to compute the muon cross section.

to a W boson and a charm quark, but the charm quark subsequently decays weakly to a strange quark and a W boson that decays into a muon and a muon neutrino. These decays are described by the diagrams in Figure 6.6 (see also Section 3.1.3). Backgrounds to these decays include primary charm decay and π/K in-flight decay.

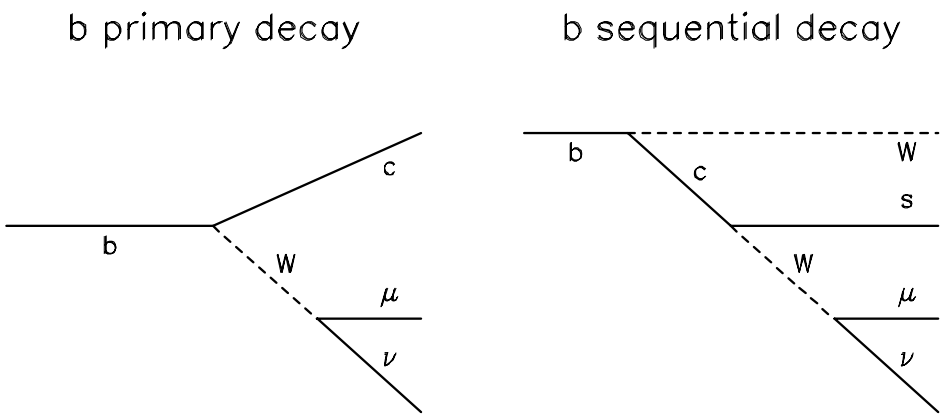

Figure 6.6: Primary (left) and sequential (right) decays of a bottom quark.

Other potential backgrounds to the muon plus associated jet sample include W/Z decay, Υ decay ($b\overline{b}$ bound states), J/ψ decay ($c\overline{c}$ bound states), Drell-Yan production ($q\overline{q} \rightarrow \gamma^* \rightarrow l^- l^+$), hadronic punchthrough, and muon fakes. Just as the jet requirement is useful for removing isolated muons from cosmic ray contamination, requiring

an associated jet strongly suppresses processes that primarily produce isolated muons, such as W/Z decay and Drell-Yan production. In addition, W and Z boson decays generally produce muons with transverse momenta beyond the 30 GeV selection cut. The cross section for muons originating from the Drell-Yan process is too small to affect this measurement, as is the cross section for muons from upsilon decays [46]. The thickness of the calorimeter and the iron toroid is approximately 14 interaction lengths and removes all hadronic punchthrough [38].

The variable $p_{\mathrm{T}}^{\mathrm{rel}}$ is defined as the component of the muon momentum perpendicular to the associated jet axis (Figure 6.7), where the jet axis is defined after first subtracting out the expected minimum ionizing particle from the jet [47]. Discrimination in $p_{\mathrm{T}}^{\mathrm{rel}}$ is available due to the heavier mass of the bottom quark; more energy is available to kick the muon out of a bottom quark jet than a charm quark jet.

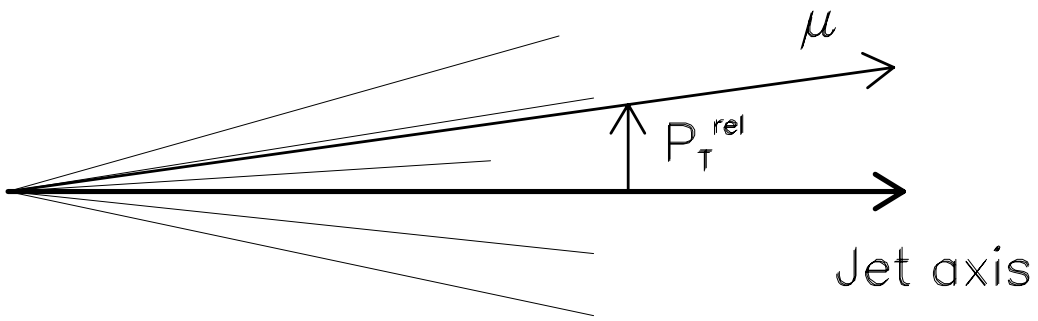

Figure 6.7: Graphic representation of the definition of $\mathrm{P}_{\mathrm{T}}^{\mathrm{rel}}$, the transverse momentum of the muon relative to the associated jet.

The primary objective is to obtain a b-produced muon cross section as a function of muon p_{T}, but discrimination is only available in the variable $p_{\mathrm{T}}^{\mathrm{rel}}$. The two variables are not strongly correlated, so a simple fit in $p_{\mathrm{T}}^{\mathrm{rel}}$ provides very little information about

the p_{T}^{μ} distribution. To obtain the fraction of muons originating in the sequential or direct decay of a bottom quark as a function of muon p_{T}, an event-by-event weighting scheme is employed. For each muon in the data sample, the probability that the muon originates from a b-quark decay is assigned as the weight for that muon. This weight can be thought of as the "b-ness" of the muon. The sum of all the weights as a function of p_{T}^{μ} divided by the total number of events in each bin is called the *b fraction*.

6.2.1 The Maximum Likelihood Fit

An event-by-event maximum likelihood fit is used to determine the fraction of muons in the sample originating from a b-quark decay. To determine the fraction A_j of the sample due to each of the contributing processes j, where $\mathrm{j} = 1, \ldots, \mathrm{N}_j$, we maximize the log-likelihood function

$$\mathrm{L} = \ln \mathcal{L} \tag{6.4}$$

with respect to A_j. The likelihood function is a measure of the probability that a set of measured quantities (x_k) are distributed according to a probability density function $(\rho(x_k))$. The likelihood function is given by the expression

$$\mathcal{L} = \prod_{i=1}^{N_i} \left[\sum_{j=1}^{N_j} \mathrm{A}j \prod_{k=1}^{N_k} \rho_k^j \left(x_k^i \right) \right], \tag{6.5}$$

where the functions $\rho_k^j \left(x_k \right)$ are the normalized probability functions for each variable x_k. In this analysis, only the variable $p_{\mathrm{T}}^{\mathrm{rel}}$ will be used, eliminating the product over k distributions. Prior to performing the maximum likelihood fit, the $p_{\mathrm{T}}^{\mathrm{rel}}$ distributions are normalized to unit area.

Input Distributions

The maximum likelihood code requires normalized input distributions of the variables being fit for signal and background. These input distributions are taken from the Rio sets 3 and 4 weighted ISAJET samples. The $p_{\mathrm{T}}^{\mathrm{rel}}$ distributions shown in Figures 6.8, 6.9, and 6.10 depict fits to the Monte Carlo for direct charm, sequential ($b \rightarrow c \rightarrow \mu$) bottom, and direct bottom decays respectively.

The p_{T}^{rel} distribution for a small sample of pions and kaons generated from 5 to 80 in hard scatter p_{T} is plotted in Figure 6.11. The p_{T}^{rel} distribution is for muons of any transverse momentum above 3 GeV/c. Along with the π/K distribution, a fit to the p_{T}^{rel} distribution for primary charm decay to muons of any transverse momentum above 3 GeV/c is also shown, normalized to the same area. Because the p_{T}^{rel} distribution for muons produced by pion and kaon decays is similar to that of muons originating from charm decays, the charm decay distribution is assumed to remove pion and kaon background as well.

In addition, the p_{T}^{rel} distributions are weakly dependent on muon transverse momentum, so the fits are made in two p_{T}^{μ} bins for each process, a low bin and a high bin. The division of 5.5 GeV/c was determined by the p_{T}^{μ} bin edge that divided the Monte Carlo statistics roughly in half to improve the quality of the fits.

The functional form employed in all fits is that of a fourth degree polynomial below a floating parameter and an exponential decay above:

$$\rho(x) = \left\{ \begin{array}{cc} p_3 \cdot x^4 + p_2 \cdot x^3 + p_1 \cdot x^2 - \alpha \cdot x & x \leq p_5 \\ \beta \cdot e^{-p_4 \cdot x} & x \geq p_5 \end{array} \right\}, \tag{6.6}$$

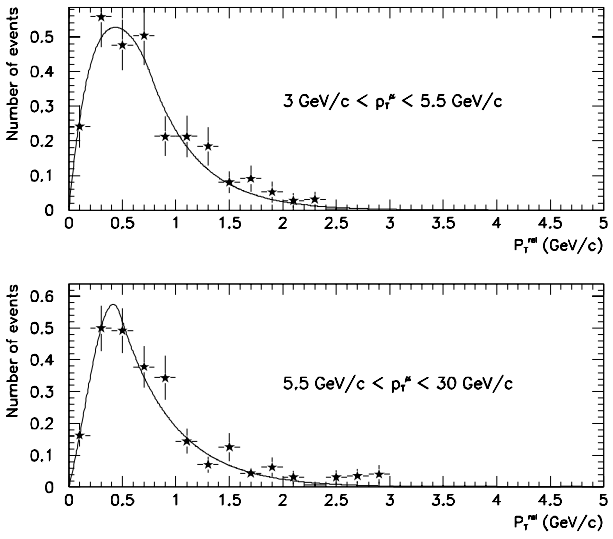

Figure 6.8: Input charm p_{T}^{rel} distributions taken from Monte Carlo. The top (bottom) distribution is for muons with transverse momenta less (greater) than 5.5 GeV/c.

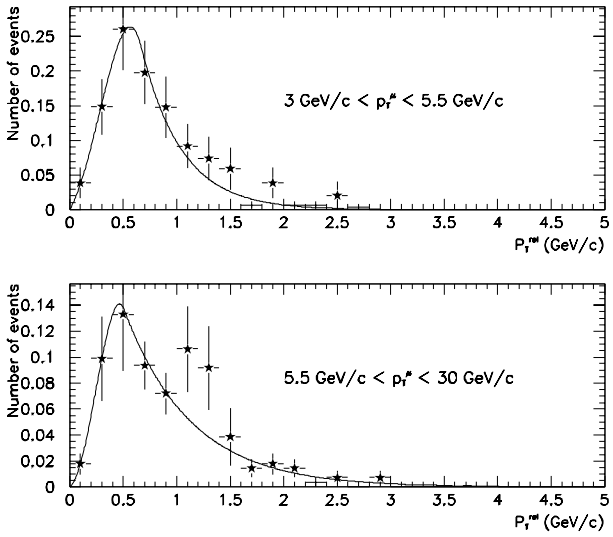

Figure 6.9: Input sequential bottom p_{T}^{rel} distributions taken from Monte Carlo. The top (bottom) distribution is for muons with transverse momenta less (greater) than 5.5 GeV/c.

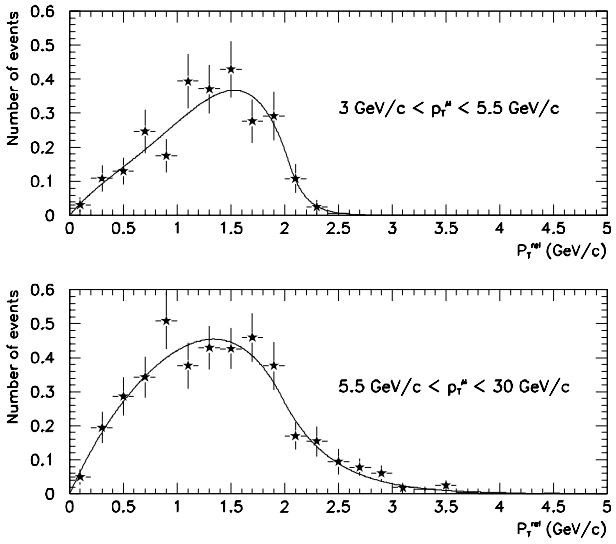

Figure 6.10: Input direct bottom p_{T}^{rel} distributions taken from Monte Carlo. The top (bottom) distribution is for muons with transverse momenta less (greater) than 5.5 GeV/c.

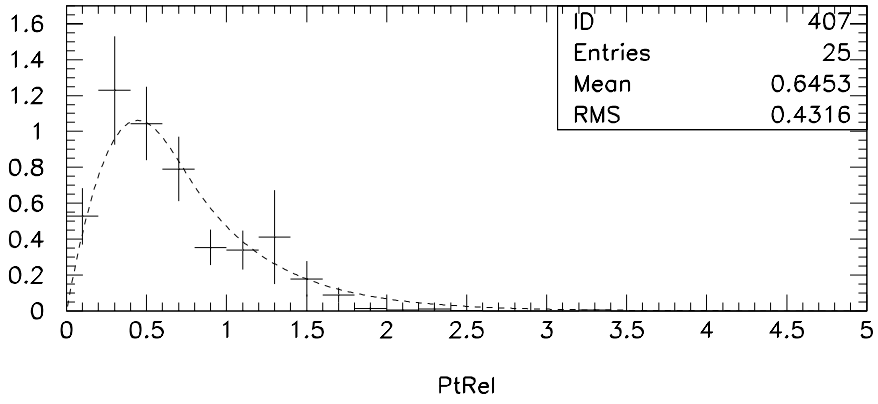

Figure 6.11: The p_{T}^{rel} distribution for muons coming from pions and kaons (histogram) compared to a fit to the p_{T}^{rel} distribution for muons originating in a primary charm quark decay. Both distributions are integrated over all p_{T}^{μ}.

where the p_i are free parameters and

$$\begin{aligned} \beta &= -\left[\frac{1}{1+p_4+p_5}\right](p_1 \cdot p_5^2 + 2p_2 \cdot p_5^3 + 3p_3 \cdot p_5^4)\, e^{p_4 \cdot p_5} \\ \alpha &= \beta p_4 e^{-p_4 \cdot p_5} + 2p_1 \cdot p_5 + 3p_2 \cdot p_5 + 4p_3 \cdot p_5 \end{aligned} \quad . \tag{6.7}$$

The form is chosen to be continuous and smooth at $p_{\mathrm{T}}^{rel} = p_5$.

Fixing the Sequential to Direct Ratio

Because sequential bottom decay exhibits a p_{T}^{rel} spectrum similar to that of direct charm decay, the normalization of the sequential decay can not be permitted to float freely in the maximum likelihood fit. Fixing the ratio of sequential bottom decays to direct bottom decays in the maximum likelihood fit removes a degree of freedom from the fit and increases the quality of the fit. The ratio obtained from Monte Carlo as a function of p_{T}^{μ} is shown Figure 6.12. Also shown is the fit of the functional form

$$f = p_1 + p_2 \cdot \left(\frac{1}{x^2}\right) + p_3 \cdot \left(\frac{1}{x^3}\right) \tag{6.8}$$

to the ratio. The dotted bands represent the uncertainty on the fit from MINUIT.

Constraining the ratio between sequential and direct decays reduces the number of distributions to two, a bottom signal distribution and a background distribution. These distributions are thus functions of muon transverse momentum as well as p_{T}^{rel}. For each event, the muon transverse momentum determines not only whether the high or low distributions are used for each process, but also the ratio of sequential to direct bottom decay. These functions are all normalized to unit area for any value of p_{T}^{μ}.

Because we are fitting only two distributions, the maximum likelihood fit must

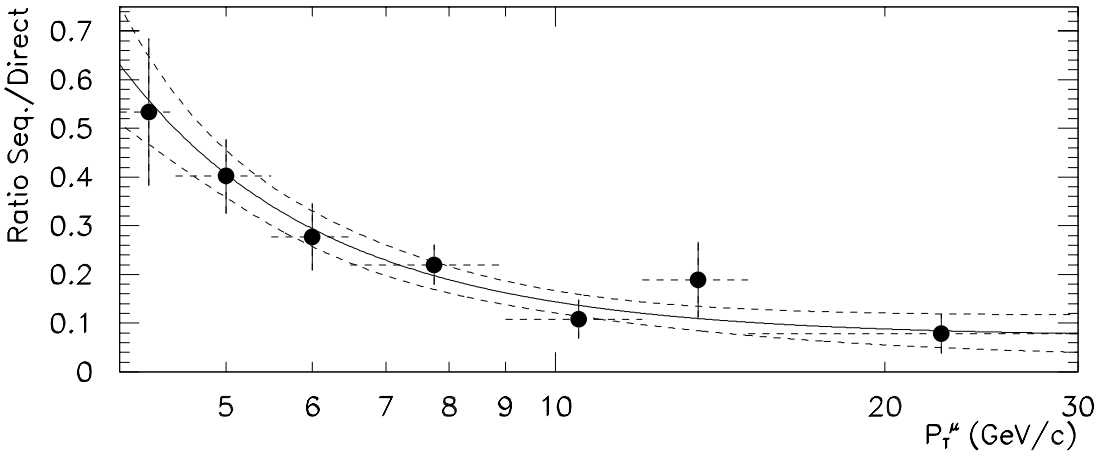

Figure 6.12: The ratio of sequential bottom decays to direct bottom decays in the Monte Carlo.

calculate two parameters, subject to the constraint

$$\sum_{j=1}^{N_j} \mathrm{A}_j = 1. \tag{6.9}$$

In practice, this constraint reduces the problem to a maximization as a function of a single parameter, p_1, where

$$\begin{aligned} \mathrm{A}_1 &= p_1 \\ \mathrm{A}_2 &= (1 - p_1)\,. \end{aligned} \tag{6.10}$$

The parameter p_1 is determined in the maximum likelihood fit to the data to be $0.48 \pm .03$. The error represents the fit error determined by MINUIT.

Results of the Maximum Likelihood Fit

The p_{T}^{rel} distributions vary as a function of muon transverse momentum due to the fixing of the sequential to direct ratio, so a global fit in the variable p_{T}^{rel} can not be shown. Instead, the results of the global fit must be shown for each p_{T}^{μ} bin. Figures 6.13 through 6.15 show the fit results in the data for all p_{T}^{μ} bins. Recall that the

maximum likelihood fit uses all events in the data sample simultaneously, so bins with fewer events are given less overall weight in the global fit.

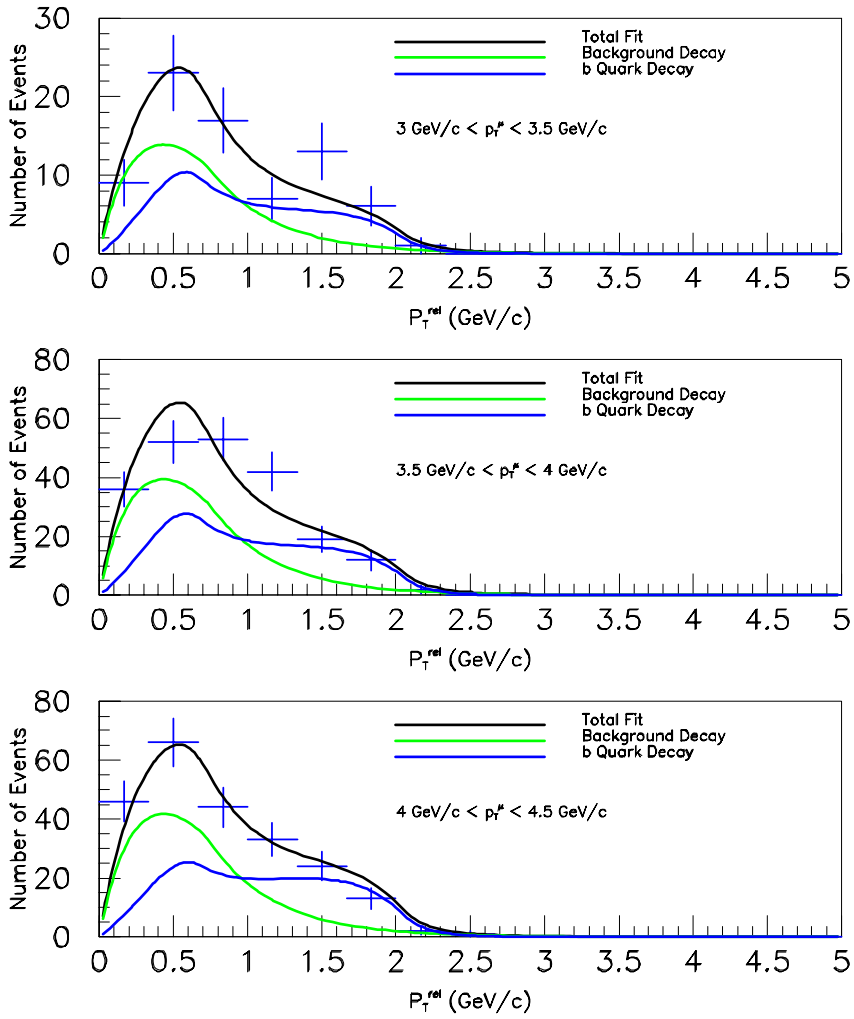

Figure 6.13: Results of the maximum likelihood fit in the data for the first three muon transverse momentum bins.

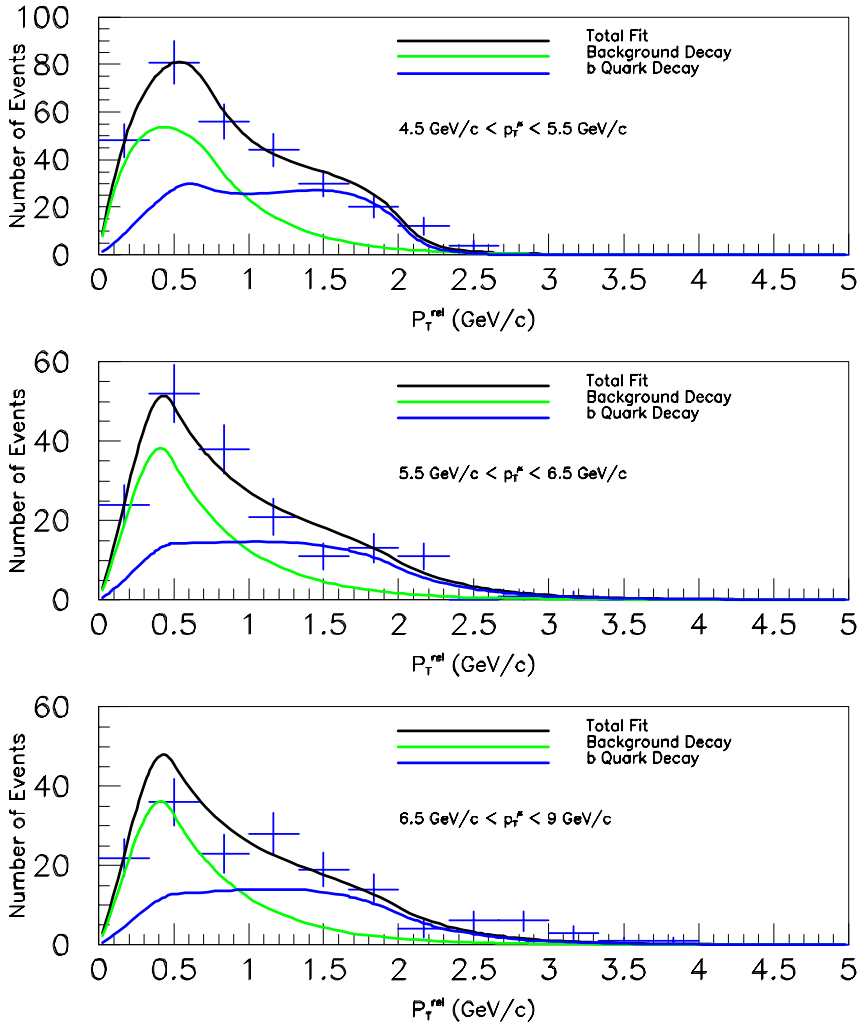

Figure 6.14: Results of the maximum likelihood fit in the data for the middle three muon transverse momentum bins.

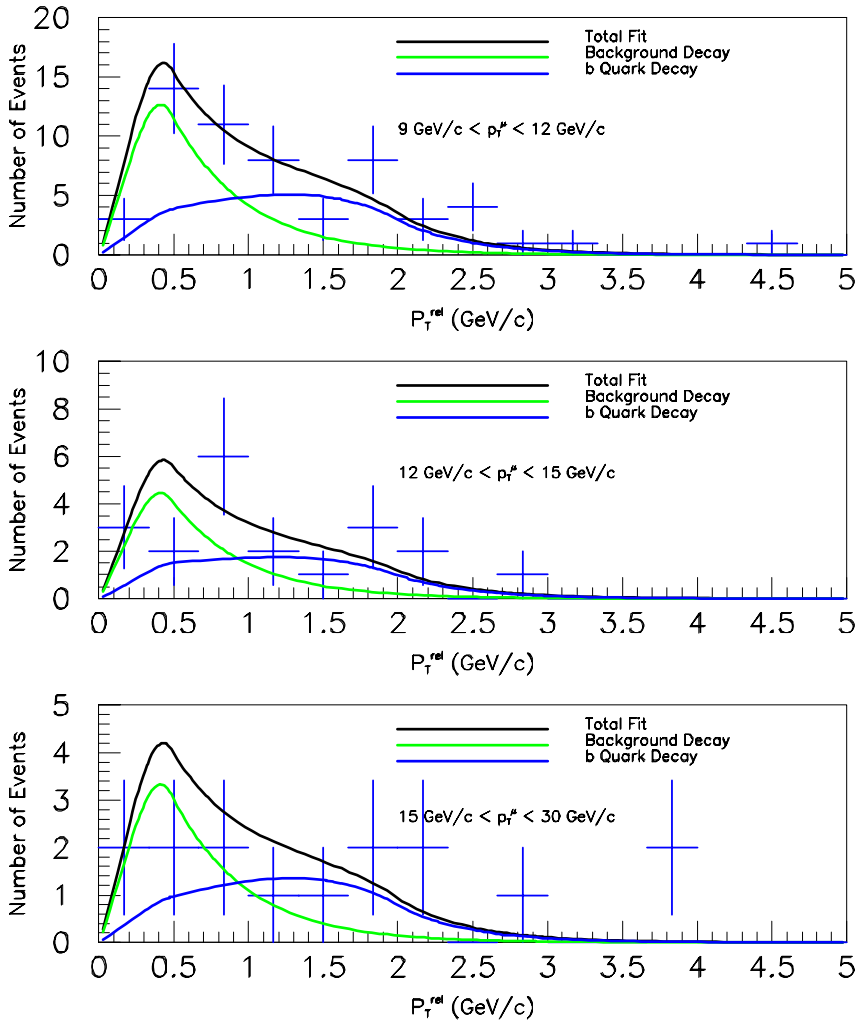

Figure 6.15: Results of the maximum likelihood fit in the data for the last three muon transverse momentum bins.

6.2.2 Determining the *b*-Fraction

To determine the bottom produced muon cross section, the fraction of muons originating from the decay of a bottom quark in the sample must be obtained. Each event is given a weight by the maximum likelihood fit that determines the likelihood, on average, that the muon was a product of a final state bottom quark. These weights are summed in each bin of muon transverse momentum and divided by the total number of events in that bin to obtain the *b-fraction* in that bin. The systematic uncertainties associated with determining the *b*-fraction are discussed below.

Tests Using Monte Carlo

IND set 2 was used to test the maximum likelihood fitting method. The Monte Carlo set was chosen despite low statistics because all events were generated in one large bin of hard scatter transverse momentum, so all the ISAJET event weights are roughly equal. Because the maximum likelihood code operates on an event-by-event basis, the events must exhibit real physics distributions to be fit properly regardless of ISAJET weight. The systematic uncertainties shown in plots 6.16 through 6.18 come from the errors on the fit parameters alone (see Appendix B for a more detailed discussion). The original ISAJET are shown without error.

Figure 6.16 shows the result of fitting IND set 2 Monte Carlo using the p_{T}^{rel} distributions obtained from Rio sets 3 and 4. The results agree agree on average to within 3%.

The data *b*-fraction is not expected a priori to agree with that found in the Monte Carlo. The maximum likelihood code must be able to account for a variable *b*-

fraction. To test the fit, a subset of the IND set 2 was prepared with the bottom quark contribution reduced by a factor of two. Figure 6.17 depicts the comparison between the actual b-fraction and that found by the maximum likelihood technique.

In addition, another subset was prepared in which the background was suppressed by a factor of two. The maximum likelihood technique was applied to this sample and also demonstrates good agreement, shown in Figure 6.18.

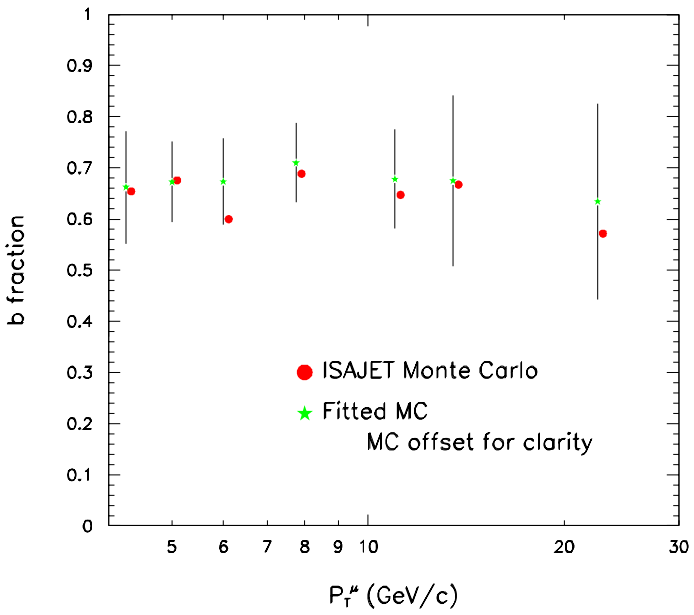

Figure 6.16: A fit with the maximum likelihood technique to the IND set 2 Monte Carlo.

b-Fraction in the Data

In Figure 6.19, the b-fraction found in the data is cross-checked with that found in fully reconstructed, weighted ISAJET Monte Carlo (Rio sets 3 and 4 with FNAL π/K). The data is found to be in good agreement with the Monte Carlo predictions.

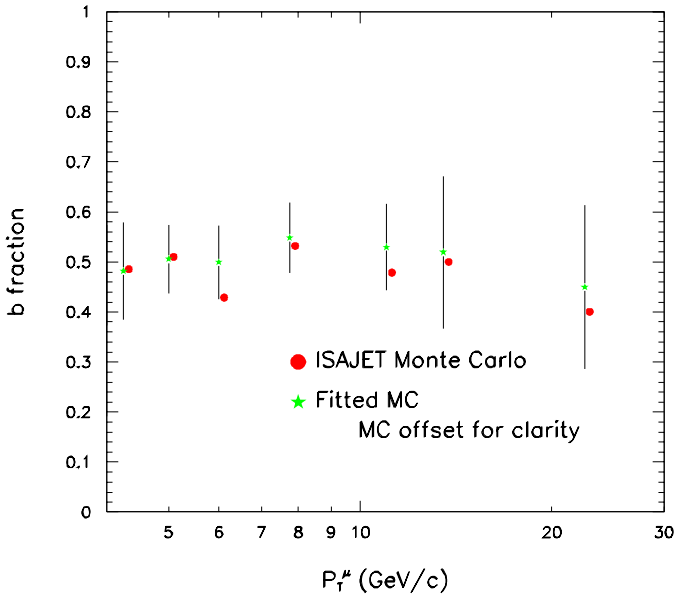

Figure 6.17: A fit with the maximum likelihood technique to the IND set 2 Monte Carlo. In this test, the bottom contribution has been reduced by half.

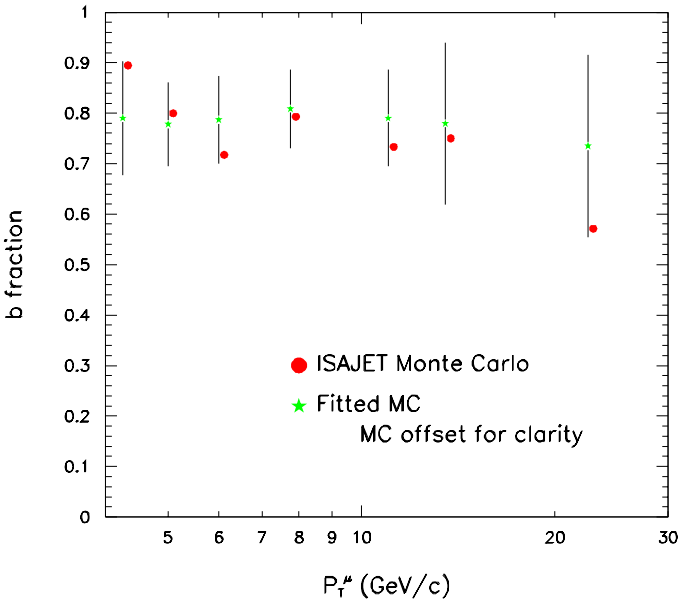

Figure 6.18: A fit with the maximum likelihood technique to the IND set 2 Monte Carlo. In this test, the background contribution has been reduced by half.

p_{T}^{μ} (GeV/c)	f_b	Δ_{fit}	Δ_{NC}	$\Delta_{bc/b}$	Δ_{MC}	Δ_{total}
$4 - 4.5$	.46	9.6	1.1	4	3	10
$4.5 - 5.5$	.47	8.7	1.2	4	3	9.2
$5.5 - 6.5$	.46	10.	1.4	4	3	11
$6.5 - 9$	.52	9.1	1.7	4	3	9.7
$9 - 12$	.55	13	2.7	4	3	14
$12 - 15$	.55	21	3.0	4	3	22

Table 6.2: The fraction of muons originating in sequential and direct bottom decays and associated relative uncertainties (expressed in percent).

The uncertainties in the plot represent the statistical and systematic uncertainties (discussed in the next section) on the b-fraction obtained in the data. The values of f_b used to compute the b-quark produced muon cross section are given in Table 6.2, along with the contributions to the total systematic error from the various sources of uncertainty.

Systematic Uncertainties on the b-fraction

The fraction of muons originating from the decay of a bottom quark in the data will be used to calculate the $b \rightarrow \mu$ cross section. Associated with this correction are uncertainties arising from how well the method can replicate known Monte Carlo samples, errors on the maximum likelihood fit parameters obtained from MINUIT, uncertainty due to the mis-estimation of cosmic ray muon background, and uncertainies due to the sequential to direct decay ratio.

Closure Tests The maximum likelihood is stable over the range of b-fractions tested, as shown in Figures 6.16 through 6.18. An uncertainty of 3%, flat in muon transverse momentum, is applied to the correction as being due to the method alone. The error associated with using only 2 bins of muon transverse momentum when

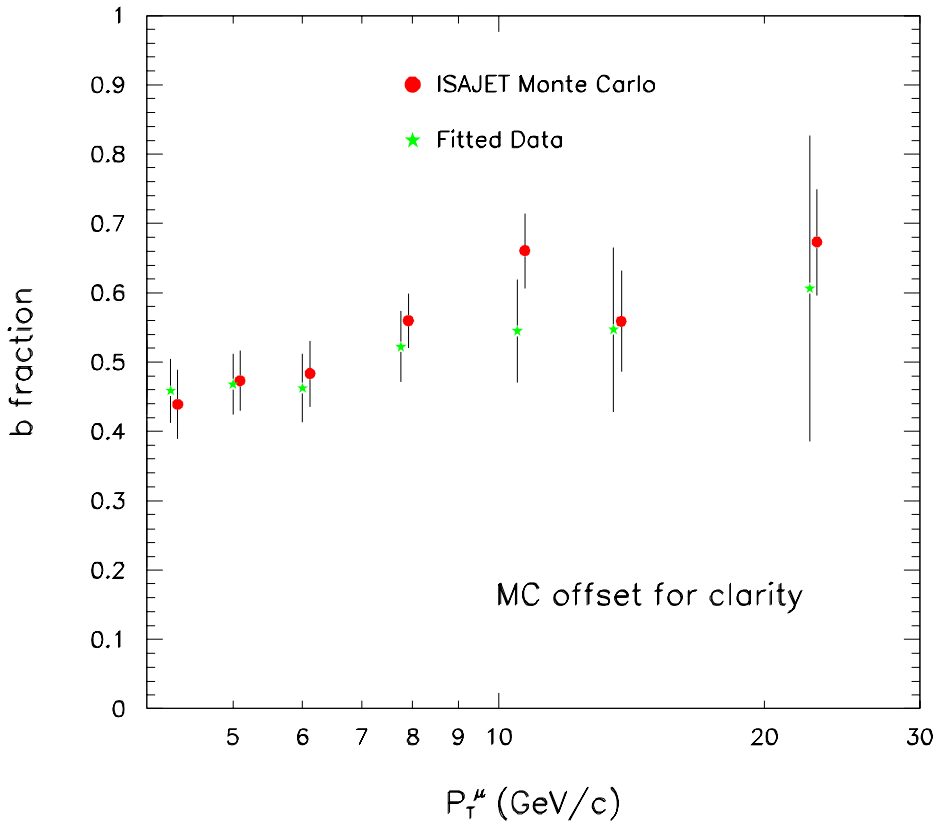

Figure 6.19: The b-fraction in the data compared to fully reconstructed, weighted ISAJET Monte Carlo.

obtaining the input distributions is contained herein

Fit Parameter The maximum likelihood fit yields a single parameter and an uncertainty on that parameter. The parameter and the uncertainty are both obtained from the MINUIT software package. The error on each event weight is calculated. Because the errors are completely correlated from event to event (see Appendix B), the errors on each weight are simply summed, not summed in quadrature. This summation reflects the overall shift of 1σ in the b-fraction for a 1σ shift in the value of the fit parameter.

Cosmic Fraction Though the cosmic ray muon fraction is small (Figure 6.5), it must be considered. The shape of cosmic ray muon $p_{\mathrm{T}}^{\mathrm{rel}}$ is compared to those of bottom and charm decays in Figure 6.20. The sample of cosmic ray muons used for this plot is obtained by making a cut of $|\Delta\mathrm{Tof}| > 15$ ns in the data sample. For the b fraction, it is assumed that cosmic ray muons mimic all processes equally, so that the b fraction obtained from the fit does not change:

$$f_b = \frac{N_\mu^b \cdot f_{NC}}{N_\mu \cdot f_{NC}} = \frac{N_\mu^b}{N_\mu}, \tag{6.11}$$

where N_μ is the number of muons, N_μ^b is the number of muons from a b decay, and f_{NC} is the fraction of muons in the sample estimated to be non-cosmic.

If cosmic ray muons do not mimic all decays equally, the b fraction changes. If cosmic ray muons appeared to only originate from b decays,

$$f_b' = \frac{N_\mu^b - N_\mu^{\cos}}{N_\mu - N_\mu^{\cos}}, \tag{6.12}$$

where N_μ^c is the number of cosmic ray muons estimated using the fit technique described above. If cosmic ray muons only appear to originate from charm and π/K

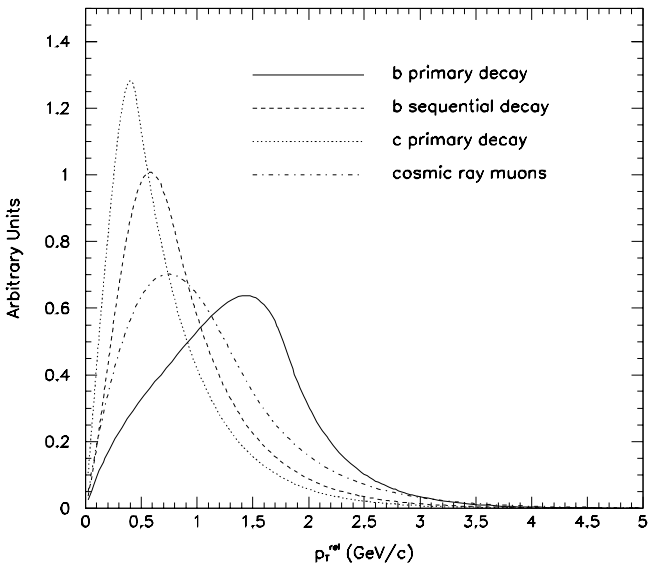

Figure 6.20: Cosmic $p_{\mathrm{T}}^{\mathrm{rel}}$ distribution compared to those used in the maximum likelihood fit. All functions have been normalized to unit area.

decays,

$$f_b'' = \frac{N_\mu^b}{N_\mu - N_\mu^{\cos}}. \tag{6.13}$$

The differences between these quantities and f_b are shown in Figure 6.21. The differences, applied as a systematic error on f_b, are averaged and further reduced by $\sqrt{\frac{1}{3}}$, assuming a uniform distribution in the variance [48].

Ratio A systematic shift in the b-fraction necessarily results from a variation of the fixed ratio between sequential and direct bottom decays. The ratio was varied within the errors of the fit shown in Figure 6.12, and the data refit with the maximum likelihood technique. The resulting b-fraction was quite stable, exhibiting a difference of about 4% for both the upper and lower error bands of the ratio fit.

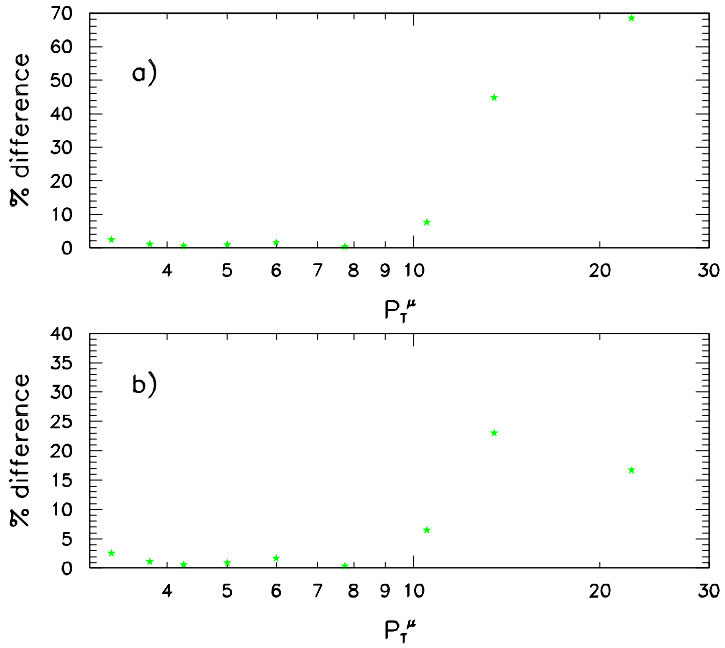

Figure 6.21: Errors on the b fraction due to cosmic background subtraction. In the top plot, cosmics are assumed not to mimic any bottom decays. In the bottom plot, all cosmics mimic bottom decays.

6.2.3 Neural Network Analysis

Neural networks are often employed as a method for solving pattern recognition problems in which one wishes to separate a data sample into signal and background based on characteristics of each. Basically extensions of the conventional methods, such as multivariate fits, neural networks are often used when the signal and backgrounds exhibit many independent variable distributions that differ slightly.

In general, one "trains" the network using equal-sized data samples of Monte Carlo samples for signal and background. The network "learns" the multivariate patterns associated with both signal and background. Then a data sample is fed through the network, and the algorithm outputs a weight between zero and one for each event that describes how much the like the signal or background the data is. The user then selects a value at which to place a cut on this output distribution, a simple process if the distributions do not overlap, and somewhat more difficult if they do. Above the cut value, the event is considered to be in the signal sample.

A neural net was trained using the Rio set 3, Rio set 4, and FNAL π/K Monte Carlo sets as input. The variables p_{T}^{μ}, the $p_{\mathrm{T}}^{\mathrm{rel}}$ of the muon, the distance in $\eta - \phi$ space between the muon and the jet, the $\mathrm{E_T}$ of the jet, and zfrag (the ratio of muon energy along the jet axis to the energy of the jet) were selected because signal and background Monte Carlo samples exhibited qualitatively different shapes. The trained net was applied to the same Monte Carlo samples. The plot of the output weights is shown in Figure 6.22. While the signal and background peaks are present, the separation is not good: if a cut were to be placed, for example, at 0.5, much of the background would remain in the sample, and much of the sample would be lost as background. The

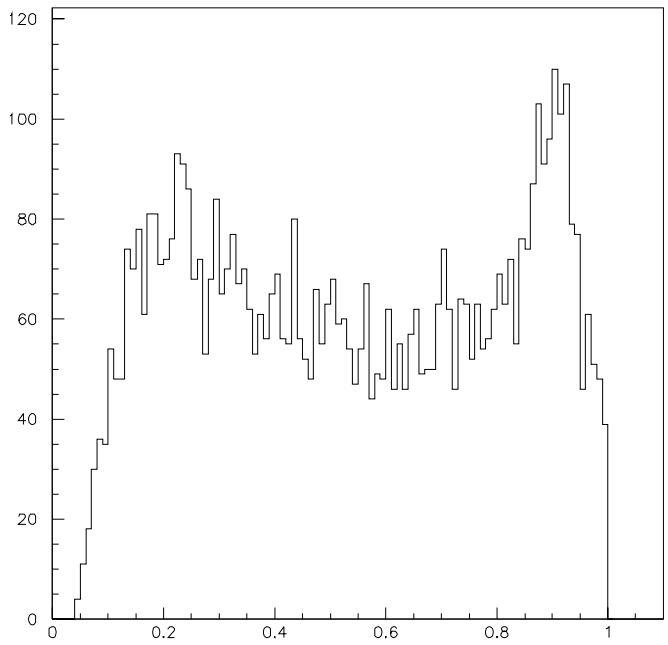

Figure 6.22: Neural network output for a Monte Carlo test. The signal and background peaks are present but are not well separated.

problem with separating signal from background is assumed to result from extremely correlated input variables.

6.3 Smeared b-Produced Muon Cross Section

A smeared muon cross section can be obtained using the b-fraction and the estimation of cosmic contamination using the prescription in the introductory section to this chapter. The raw number of muons (N_μ) and the number of bottom-produced muons after background subtraction $\left(N_\mu^b = N_\mu \cdot f_{NC} \cdot f_b\right)$ are shown as a function of muon transverse momentum in Figure 6.23. In Figure 6.24, the raw differential muon cross section is presented; this plot includes the statistical error on the data as well as the systematic effects of the cosmic subtraction and the application of the b fraction. To obtain the true differential cross section, the distribution must be corrected (or "unsmeared") to account for the limited muon momentum resolution of the detector, and also corrected for the efficiencies of the cuts described in Chapter 5.

6.4 Summary

This chapter has summarized the background subtraction methods used in this analysis. When computing the bottom quark produced muon cross section, the values for the non-cosmic fraction and the b-fraction, presented in Tables 6.1 and 6.2 respectively, are used to compute the number of muons coming from bottom quark decays $\left(N_\mu^b = N_\mu \cdot f_{NC} \cdot f_b\right)$. The next chapter describes the prescription for unsmearing the muon momentum spectrum.

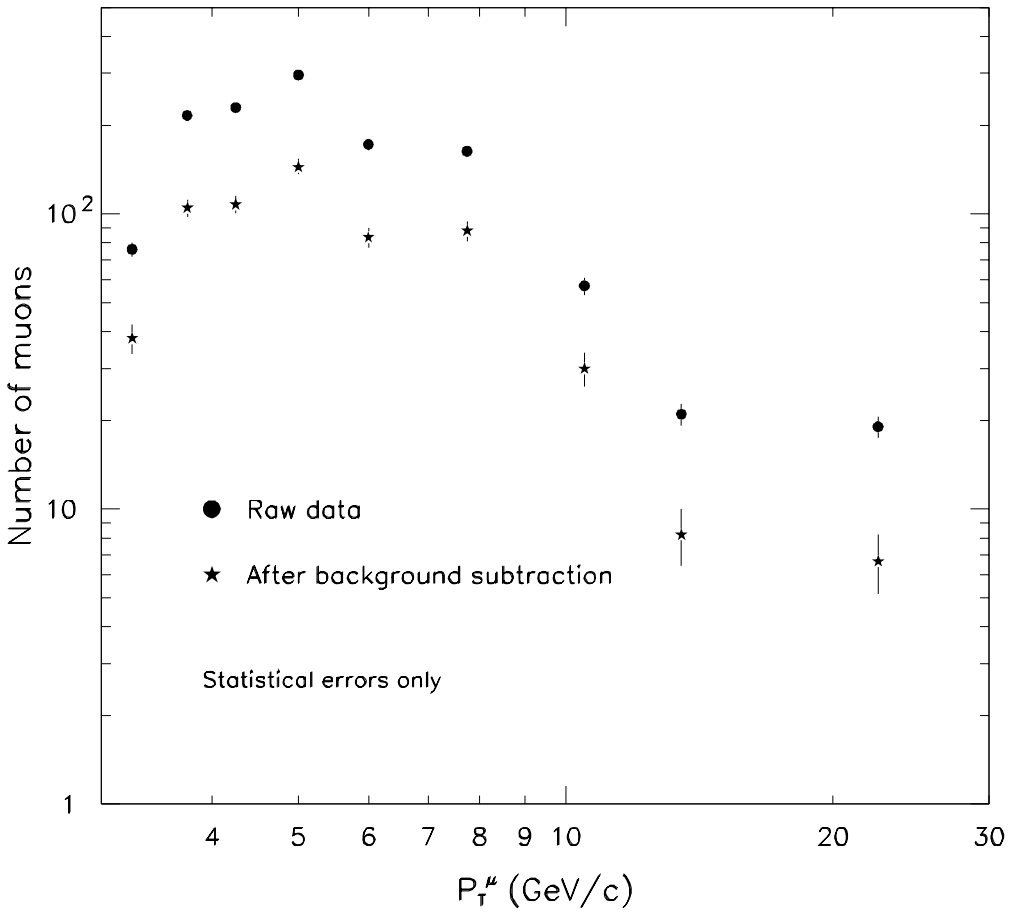

Figure 6.23: The raw number of muons as a function of muon transverse momentum before and after background subtraction. The errors shown are statistical only.

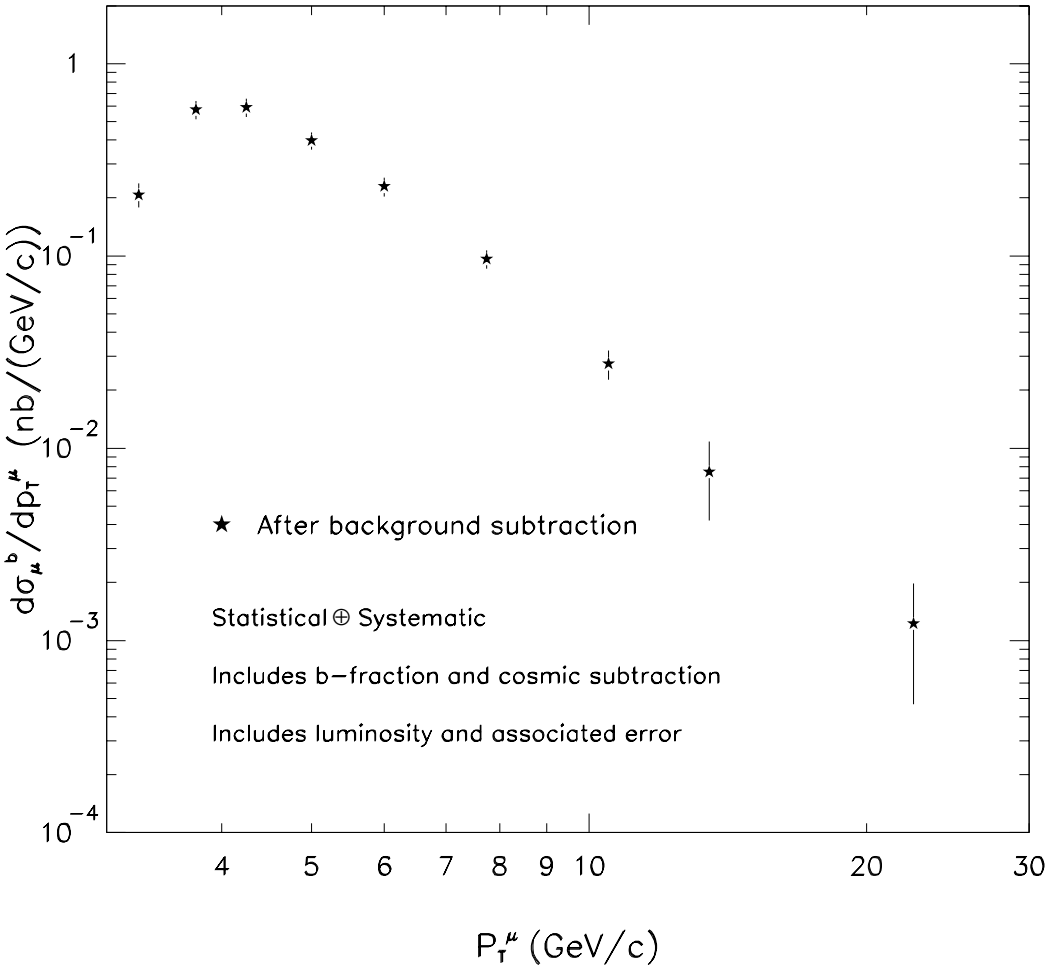

Figure 6.24: The raw differential b-produced muon cross section. The errors shown include systematic errors from background subtraction. This cross section does not include momentum resolution or efficiency corrections.

CHAPTER 7

UNSMEARING THE MUON MOMENTUM RESOLUTION

The DØ muon spectrometer consists of three layers of drift tubes, the first two layers of which are separated by the central iron toroid. The toroid bends the muon in polar angle, θ, allowing measurement of its momentum. Two effects, the position resolution of the drift tubes and multiple scattering of the muon in the calorimeter and toroid, contribute to the finite momentum resolution. To account for the effect of the finite resolution on the on the true p_{T}^{μ} spectrum, the measured spectrum must be unsmeared.

To understand momentum smearing, consider a steeply falling spectrum as a function of transverse momentum bin number (Figure 7.1, solid line). If the resolution is not perfect, some muons with a true transverse momentum falling in one bin will be measured as having a transverse momentum. In the extremely simple case that the resolution is the same across all the bins, and the number of muons in each bin is mismeasured so that 20% of the events in each bin migrate with equal probability to the right and the left, more events migrate to the right across bin boundaries, inflating the cross section at higher transverse momentum. The dotted line depicts the smeared cross section.

In the DØ muon system, the smearing is somewhat more complicated. Bin widths and momentum resolution vary as a function of muon transverse momentum. In addition, edge effects in the smearing occur because muons with real transverse momenta less than 3 GeV can not penetrate the central iron toroid. An example of an edge

effect is provided in Figure 7.1, in which events have been allowed to smear out of the distribution to the left and right, while no events are permitted to smear in, resulting in a suppressed spectrum at the low edge. In the data, edge effects and the efficiency turn-on result in supression of the low end of the p_{T}^{μ} spectrum.

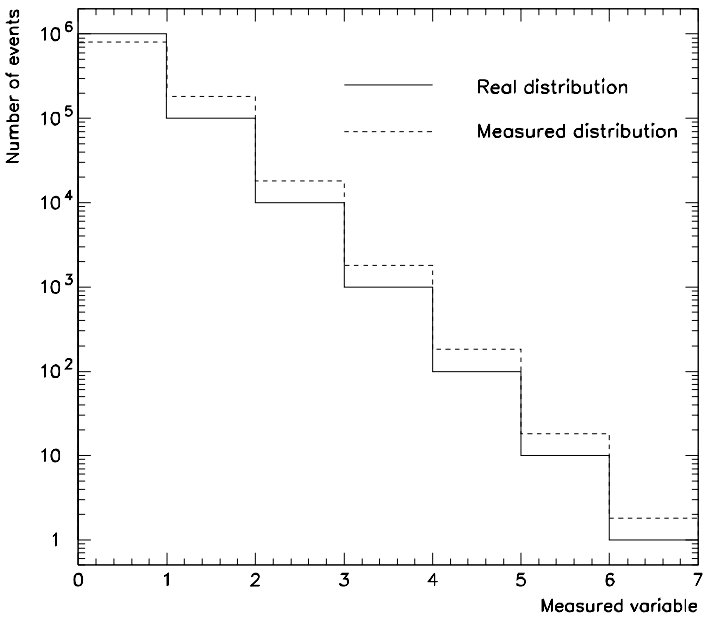

Figure 7.1: The smearing effect on a steeply falling spectrum. The solid line is the real spectrum, and the dashed line is the spectrum after smearing.

7.1 Muon Momentum Resolution

The muon momentum resolution was obtained using the Run 1a $Z \rightarrow \mu\mu$ data sample and cross checked in Monte Carlo [50]. The data were fit with a simple function

$$\frac{\sigma\left(\frac{1}{p^{\mu}}\right)}{\left(\frac{1}{p^{\mu}}\right)} = \sqrt{\left(\frac{c_1(p^{\mu}-2)}{p^{\mu}}\right)^2 + (c_2 p^{\mu})^2}, \tag{7.1}$$

where the first term on the right-hand side represents the effect of multiple scattering, the second term describes the detector position measurement uncertainties, and p^{μ} is given in GeV/c. From the fit to the Z data, the constant c_1 was determined to be 0.18, while c_2 was found to have a value of 0.003 ± 0.001.

The momentum resolution was also examined in a reconstructed sample of low-energy fully GEANTed Monte Carlo events processed with DØRECO V12.21. In each momentum bin, $\sigma\left(\frac{1}{p^{\mu}}\right)$ was taken to be the width of the gaussian distribution of the difference between inverse reconstructed momentum and inverse ISAJET momentum. Figure 7.2 depicts the distribution $\left(\frac{1}{p^{\mu}_{\mathrm{ISAJET}}} - \frac{1}{p^{\mu}_{\mathrm{reco}}}\right)$ for the first bin. Note that the shoulder to the left of the central peak is not included in the determination of $\sigma\left(\frac{1}{p^{\mu}}\right)$. Further, at low p^{μ}_{T} in the lower bins, the central value is shifted significantly away from zero. The points in Figure 7.3 depict the quotient $\sigma\left(\frac{1}{p^{\mu}}\right) / \left(\frac{1}{p^{\mu}}\right)$, where the value of the denominator was taken to be the average value of the true inverse ISAJET momentum in that bin. The solid line shows Equation 7.1 with the parameters from the data fit. The dashed line represents the same function with a c_2 value of 0.008, and the dotted line denotes a fit to the low energy Monte Carlo points, resulting in a value for c_2 of 0.012. Because the multiple scattering term does not change in these studies, the resolution will henceforth be denoted by the value of c_2 in Equation 7.1. In this nomenclature, the solid line in Figure 7.3 represents "0.003 smearing."

7.2 Bayesian Unsmearing

Various methods may be used to unsmear the momentum spectrum. For example, one method involves building a smearing matrix from reconstructed Monte Carlo events

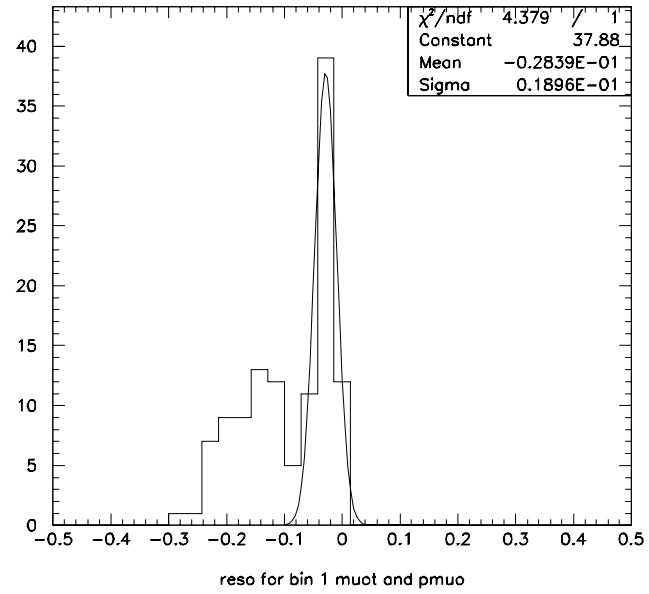

Figure 7.2: Plot of $\Delta\left(\frac{1}{p^{\mu}}\right)$ for bin 1. Note that the shoulder to the left of the gaussian is not used in the fit.

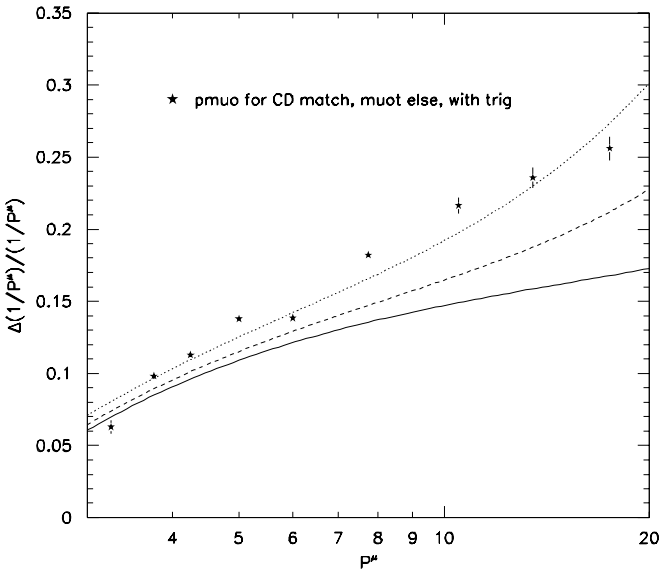

Figure 7.3: Muon momentum resolution. The stars represent fully reconstructed low energy ISAJET. The solid line represents the fit to the Run 1A Z data, and the dotted line depicts a fit to the Monte Carlo.

that quantifies the migration between reconstructed and "true" momentum bins. Inverting the normalized smearing matrix and multiplying it by the data distribution should result in the real muon spectrum. The problem with simple matrix inversion is that it depends strongly on the measured and reconstructed transverse momentum spectra; instead, an alternative method of unsmearing is examined — Bayesian unsmearing.

7.2.1 Bayes' Theorem

Bayesian unsmearing describes a particular technique of unsmearing data based on Bayes' Theorem:

$$P(C_i \mid E) = \frac{P(E \mid C_i) \cdot P(C_i)}{\sum_{l=1}^{n_c} P(E \mid C_l) \cdot P(C_l)}, \tag{7.2}$$

where C_i is the ith cause that can produce an effect E. In our case, the C_i's represent the real transverse momentum of the muon, and the effect is the measured p_{T}^{μ}; thus, $P(E \mid C_i)$ is simply the probability that a muon in a p_{T}^{μ} bin representing E came from a muon with a real p_{T}^{μ} in bin i. This method can be applied for several effects, or several reconstructed p_{T}^{μ} bins, by noting that

$$P(C_i \mid E_j) = \frac{P(E_j \mid C_i) \cdot P(C_i)}{\sum_{l=1}^{n_c} P(E_j \mid C_l) \cdot P(C_l)}, \tag{7.3}$$

where E_j represents the reconstructed p_{T}^{μ} bin j. Unsmearing the measured p_{T}^{μ} spectrum should yield the true p_{T}^{μ} spectrum, or the number of events in each cause bin $\hat{n}(C_i)$. The number of events in each bin must be given by

$$\hat{n}(C_i) = \sum_{j=1}^{N_j} P(C_i \mid E_j) \cdot \hat{n}(E_j). \tag{7.4}$$

The procedure for obtaining $\hat{n}(C_i)$ is as follows:

1. Select an initial distribution for $P_0(C_i)$, the initial guess at the correct unsmeared momentum distribution, subject to the constraint that

$$\sum_{i=1}^{N_i} P_0(C_i) = 1. \tag{7.5}$$

   In this analysis, the generated ISAJET Monte Carlo p_{T}^{μ} distribution functions as the "best" initial guess at the spectrum. This guess also selects the initial expected number of events ($\hat{n_0}(C_i) = P_0(C_i) \cdot N_{obs}$).

2. Calculate $\hat{n}(C_i)$ and $P(C_i)$.

3. Perform a χ^2 comparison between $\hat{n}(C_i)$ and $\hat{n_0}(C_i)$.

4. Replace $P_0(C_i)$ with $P(C_i)$, and $\hat{n_0}(C_i)$ with $\hat{n}(C_i)$ and restart the process. After the second iteration, if the χ^2 value is small, stop the iteration; otherwise, return to step 2 and repeat.

Bayesian unsmearing offers many advantages over other unsmearing methods. First, the Bayesian method is theoretically sound. Second, it should not depend on the shape of the distribution being unsmeared, should the need arise. Third, although the method gives the best results if one uses a realistic starting guess, a satisfactory result can still be obtained from a uniform initial distribution. Last, Bayesian unsmearing does not require matrix inversion, which fails if the smearing matrix is singular. For further details on unsmearing using the Bayesian method, the interested reader is directed to consult G. D'agostini [51].

7.2.2 Using Monte Carlo to Test the Method

Before the unsmearing procedure is applied to the data p_{T}^{μ} distribution, it is tested on Monte Carlo distributions. A brief exposition of the terms that will be used is required:

- *real distribution* – The *real distribution* refers to the true ISAJET p_{T}^{μ} distribution. Bayesian unsmearing attempts to reproduce the real distribution from the measured distribution. Note that in all tests, each event in the real distribution must pass many quality cuts as well as the low energy central muon trigger (MU_1_CENT_LNR).

- *measured distribution* – The *measured distribution* refers to the transverse momentum spectrum of muons measured in the detector. In the Monte Carlo tests, the reconstructed spectrum from GEANTed and RECOed Monte Carlo serves as the measured distribution.

- *unsmeared distribution* – The output of the unsmearing procedure, the *unsmeared distribution* is taken to be our best estimate of the true muon transverse momentum spectrum. In the Monte Carlo tests, it is compared with the real distribution. When the data are unsmeared, the unsmeared distribution is considered to be the true muon spectrum.

- *smearing matrix* – The *smearing matrix* describes the bin-to-bin migration of events from the real distribution to the measured distribution. It is created from Monte Carlo events that have been passed through a full simulation of the DØ muon system. In terms of Bayes' Theorem, events with true transverse

momentum in bin i and reconstructed transverse momentum j correspond to the element $P\left(E_j|C_i\right)$.

- *unsmearing matrix* – The *unsmearing matrix*, which corresponds to $P(C_i \mid E_j)$ in the expressions above, is computed by the Bayesian code and used to obtain the unsmeared spectrum from the measured one.

Figure 7.4 depicts an example of the unsmearing method. The histogram represents the real distribution, the stars represent the measured distribution, and the closed circles represent the unsmeared spectrum. The smearing matrix was generated from the RECOed Monte Carlo events being unsmeared, so the unsmearing code reproduces the original spectrum after one iteration. The small error bars on the difference plot represent only the statistical errors described in the next section. The p_{T}^{μ} ranges corresponding to each bin are given in Table 5.2.

7.3 Errors on the Unsmearing

Use of the Bayesian method requires correct propagation of not only the statistical uncertainty on the measured distribution, but also the statistical uncertainty of the smearing matrix used by the Bayesian code. The statistical uncertainty on the measured (data) distribution is due to the number of events measured. The other statistical uncertainty arises from limited Monte Carlo statistics used in constructing the smearing matrix. Both errors are computed by the code and used to build the covariance matrix. Systematic uncertainties associated with the unsmearing procedure must be evaluated separately.

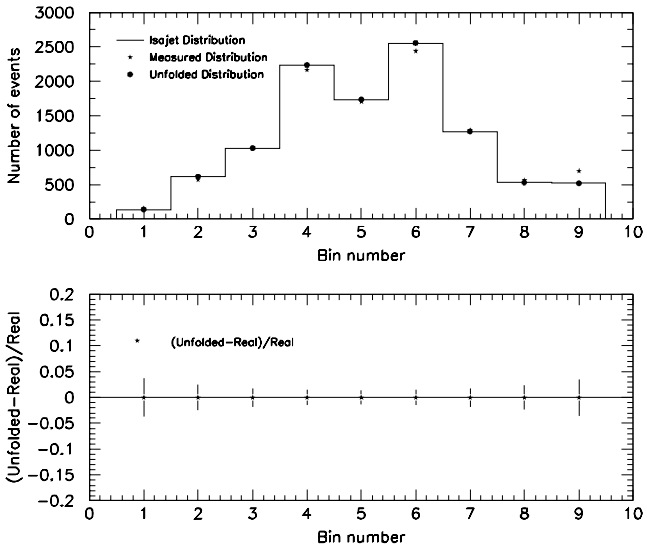

Figure 7.4: The measured Monte Carlo distribution has been unsmeared after one interation.

7.3.1 Systematic Uncertainties

While the Bayesian method unsmears a measured spectrum using the smearing matrix that produced it, a systematic variation of the input distributions, the smearing matrix, and the shape of the p_{T}^{μ} spectrum must be examined to determine the effect on the unsmeared results. The following subsections detail the studies of the systematic errors associated with Bayesian unsmearing.

Use of a Toy Monte Carlo

Because reconstruction of ISAJET Monte Carlo events is time-consuming and CPU-intensive, a toy Monte Carlo was written to generate a p_{T}^{μ} distribution modeled on a fit to a preliminary measurement of the b-produced muon spectrum from the inclusive muons channel. For each muon generated, the Monte Carlo calculates a smeared

momentum using the sigma and mean of the gaussians determined as in Figure 7.2. Note that the shoulder seen in the reconstructed Monte Carlo is not reproduced in the toy. Figure 7.5 depicts both the real spectrum and the smeared spectrum produced by the toy Monte Carlo.

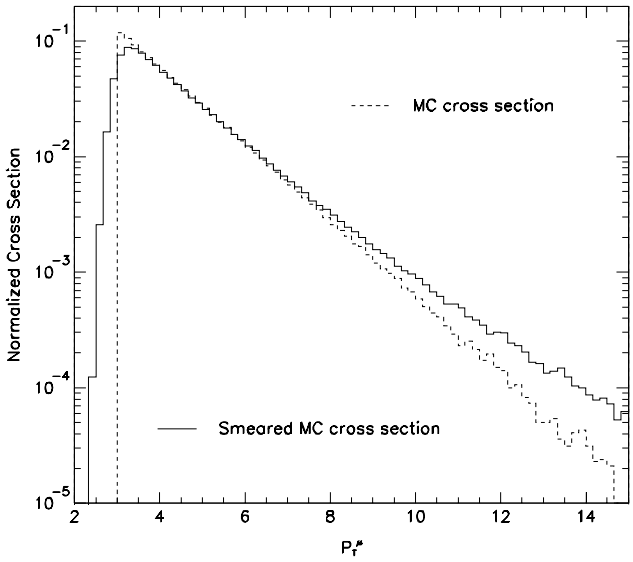

Figure 7.5: The toy Monte Carlo cross section (dashed line) has been smeared with 0.012 smearing and renormalized.

The goal of using the toy Monte Carlo is to understand the effect of a varying resolution on the unsmearing procedure. The Run 1 data exhibits 0.003 smearing, while the reconstructed Monte Carlo used to unsmear the momentum distribution exhibits 0.012 smearing. The toy Monte Carlo allows examination of the difference in the output of the Bayesian method for these two smearings.

Before examining the difference in the two smearings, it is imperative to ensure that the toy Monte Carlo, using the same smearing as the reconstructed Monte Carlo, unsmears the data in the same way. Figure 7.6 depicts this comparison. The toy

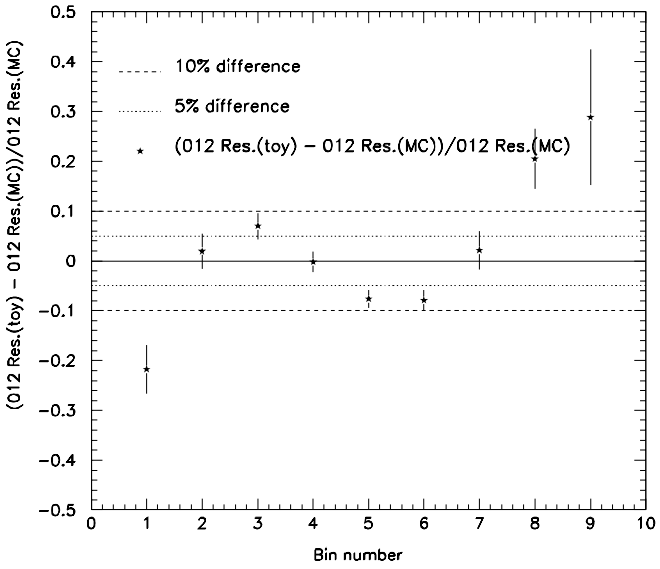

Figure 7.6: The difference between unfolding with the toy MC (0.012 smearing) and the reconstructed ISAJET.

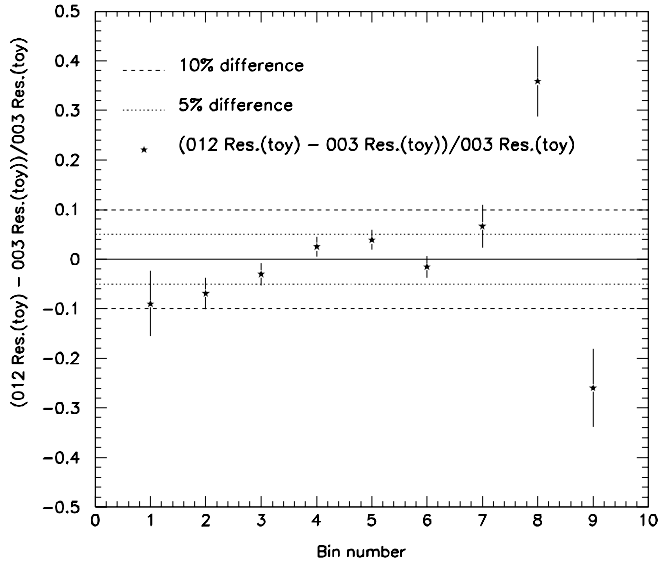

Figure 7.7: The toy MC is used to build two smearing matrices based on two different resolutions (0.003 and 0.012). The difference between unsmearing for the two resolutions is shown above.

reproduces the smearing of the reconstructed ISAJET fairly well, so the toy Monte Carlo can be employed to investigate the difference between unsmearing with 0.003 smearing and unsmearing with 0.012 smearing.

First, the toy Monte Carlo is used to build two smearing matrices for use with the Bayesian code. The code is run with the same initial guess and input distribution for both the 0.003 smearing and the 0.012 smearing. Figure 7.7 compares the results. This difference is taken to be the systematic uncertainty due to the difference in resolutions between the reconstructed Monte Carlo and the data.

Two additional effects must be evaluated to complete the evaluation of potential errors on the unsmearing due to the resolution. In Figure 7.2, the fully reconstructed Monte Carlo exhibits both an offset and a shoulder in the difference between the inverses of real and reconstructed transverse momentum. Because it is not known whether these effects occur in the data, they must be included in the systematic error for completeness. The toy Monte Carlo can be used to evaluate the effect of using a mean of 0 in the computation of the smeared momentum. This difference is depicted in Figure 7.8. In addition, using the reconstructed Monte Carlo with a cut of 0.1 on $\left|\left(\frac{1}{p^{\mu}_{\mathrm{ISAJET}}} - \frac{1}{p^{\mu}_{\mathrm{reco}}}\right)\right|$ to build the smearing matrix allows examination of the effect of the shoulder on unsmearing (Figure 7.9). Note that the systematic effect of removing the offset in the mean when smearing the momentum dominates the systematic error at low p^{μ}_{T}.

Shape Dependence

The Bayesian technique should depend only on the bin-to-bin migration of the events, not on the shape of the distribution being unsmeared. How the procedure unsmears

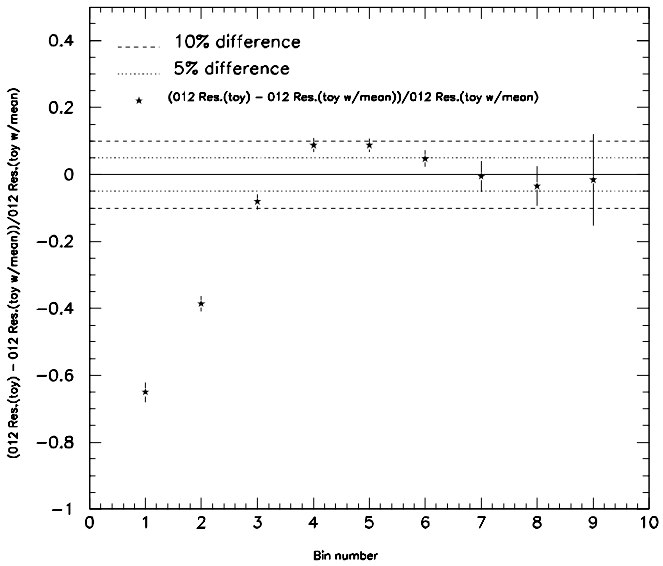

Figure 7.8: The effect of removing the offset in calculating the smeared momentum.

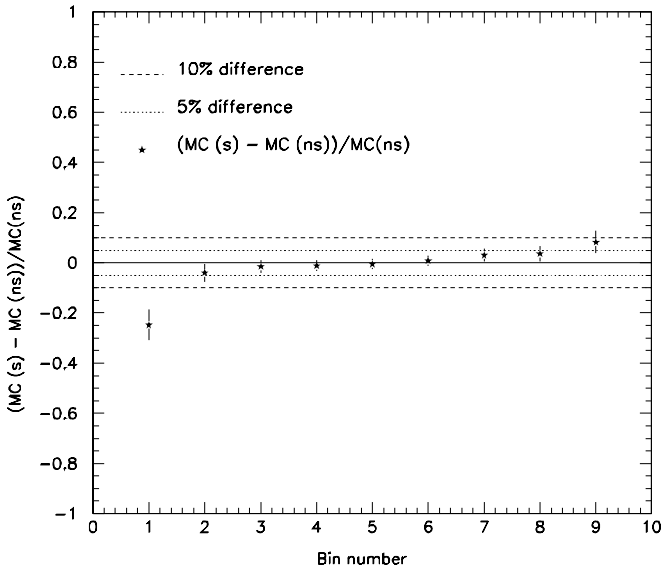

Figure 7.9: The effect the shoulder on $\Delta\left(\frac{1}{\mathrm{p}^{\mu}}\right)$.

spectra that exhibit different shapes must be investigated. To begin with, the toy Monte Carlo can be employed to examine the effect of weighting the momentum distribution with a very steep function. Figure 7.10 shows the effect of weighting the original momentum spectrum by $1/\left(p_{\mathrm{T}}^{\mu}-1.5\right)^{3}$ and renormalizing.

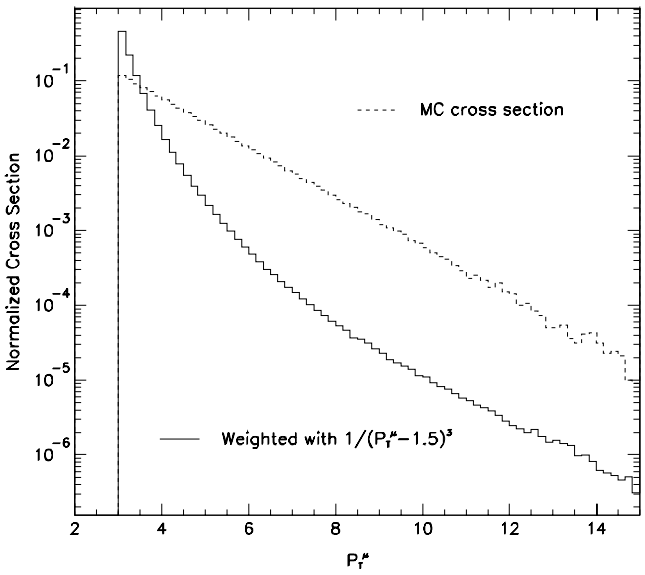

Figure 7.10: The toy MC momentum distribution weighted with a steep function and renormalized.

The original reconstructed Monte Carlo p_{T}^{μ} spectrum is compared to both the data and the weighted Monte Carlo spectrum in Figure 7.11. The data histogram lies between the two sets of points. The assumption is that if the Bayesian code can unsmear the steep distribution correctly, it can also unsmear the data distribution. The original reconstructed Monte Carlo is used to build the smearing matrix. The difference between the real weighted distribution and the unsmeared distribution is given in Figure 7.12.

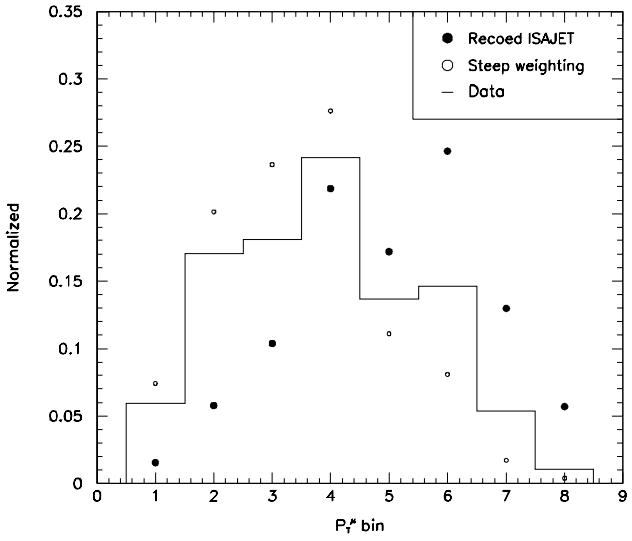

Figure 7.11: Fully reconstructed ISAJET (solid circles) and weighted ISAJET (open circles). The data (histogram) lies between them.

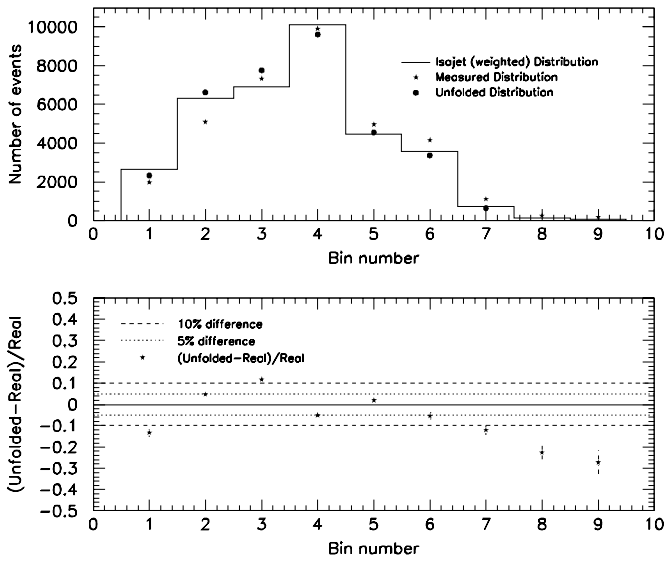

Figure 7.12: Unsmearing a steeply weighted MC distribution.

Variation in Initial Guess

While the Bayesian method should provide a reasonable unsmearing of the data given a completely flat initial spectrum, best results are obtained when the initial guess approximates the real distribution. When unsmearing, the initial guess is usually taken to be the real p_{T}^{μ} spectrum from the reconstructed Monte Carlo. Variation of the initial guess to steeper (Figure 7.13) and shallower (Figure 7.14) distributions yields a slightly different unsmeared spectrum. As an example, the steep initial guess is provided by the points in Figure 7.11.

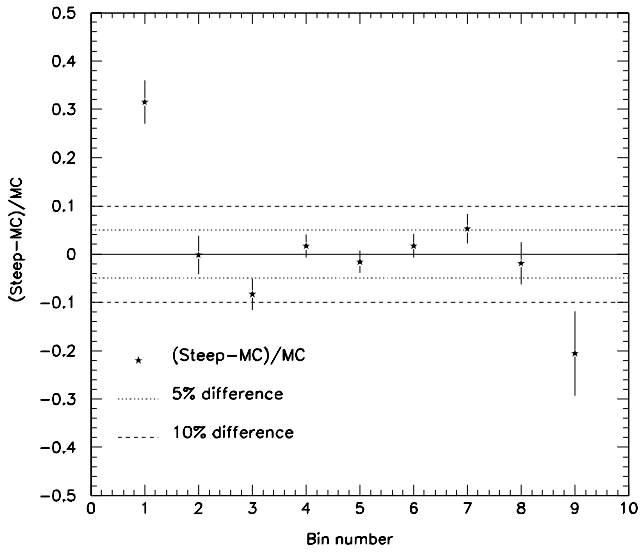

Figure 7.13: Effect of the initial guess on the unsmearing.

7.3.2 Combination of the Errors

The contributions to the total systematic error as a function of muon transverse momentum bin are shown in Table 7.1. The contributions to the total uncertainty come from variation of the initial guess to steeper (Δ^{0}_{steep}) and shallower ($\Delta^{0}_{shallow}$)

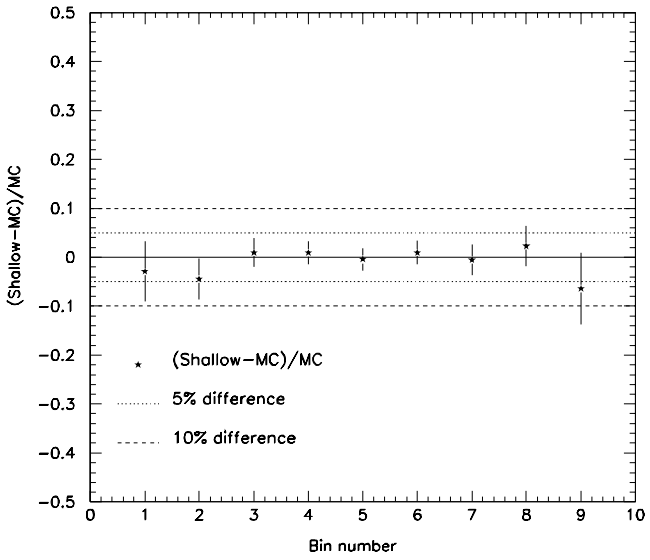

Figure 7.14: The difference between unsmearing with a more shallow initial guess and the real MC distribution.

spectra as well as the uncertainty associated with unsmearing a more steeply-falling true transverse momentum spectrum (Δ_{steep}). The total systematic also includes uncertainties due to the difference between the toy Monte Carlo and smeared ISAJET (Δ_{res1}) and the use of different resolutions in the Monte Carlo compared to that measured in samples of Run 1A data (Δ_{res2}). The uncertainty accounts also for effects seen in the Monte Carlo that may or may not be in the data sample (Δ_{off}, Δ_{shoul}).

All contributions to the uncertainty on the unsmearing procedure are added in quadrature (total systematic error) and are plotted as a function of p_{T}^{μ} in Figure 7.15. The large error on the outermost points is dominated at the low end by the mean shift in the resolution function, and at the high end by potential variations in resolution.

$p_{\mathrm{T}}^{\mu}\left(\frac{GeV}{c}\right)$	Δ^{0}_{steep}	$\Delta^{0}_{shallow}$	Δ_{res1}	Δ_{res2}	Δ_{steep}	Δ_{off}	Δ_{shoul}	Δ_{syst}
$4-4.5$	8.2	1.0	6.9	3.1	12	8.2	1.5	17
$4.5-5.5$	1.7	0.9	0.2	2.5	5.1	8.7	1.2	11
$5.5-6.5$	1.6	0.4	7.6	3.8	1.9	8.7	0.5	10
$6.5-9$	1.8	1.0	7.9	1.5	5.4	4.6	0.9	7.6
$9-12$	5.3	0.5	2.1	6.6	12	0.6	3.1	15
$12-15$	1.9	2.3	20	35	22	3.4	3.6	42

Table 7.1: Contributions to the unsmearing factor systematic (expressed in percent).

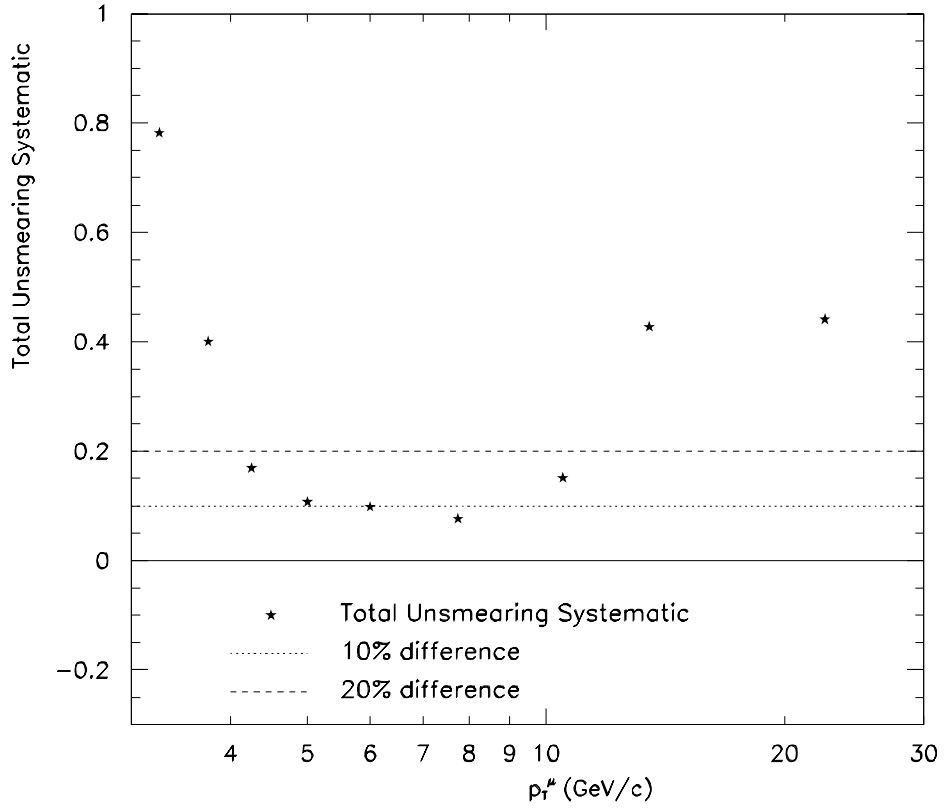

Figure 7.15: The combined systematic error on the unfolding. The first two bins and the last bin are not used to calculate the final results.

$p_{\mathrm{T}}^{\mu}\left(\frac{GeV}{c}\right)$	f_{uns}	Δ_{stat}	Δ_{syst}	Δ_{total}
$4-4.5$	1.17	9.2	17	19
$4.5-5.5$	.91	9.4	11	14
$5.5-6.5$	.90	11	10	15
$6.5-9$	.85	13	8	15
$9-12$	.67	23	15	27
$12-15$	.46	37	43	57

Table 7.2: The unsmearing correction obtained using the Bayesian unfolding procedure along with uncertainties (expressed in percent).

7.4 Unsmearing the Data

Using the Bayesian technique describe in the preceding sections, the data spectrum has been unsmeared (Figure 7.16). The distribution unsmears as expected physically; the muon transverse momentum spectrum becomes steeper and softer. In the figure, the spectrum has been divided by the width of the transverse momentum bins. Figure 7.17 shows the ratio of the two distributions. This ratio, called the *unsmearing factor* or f_{uns}, is the correction factor applied to the data distribution to make final cross sections. The unsmearing factors as a function of muon transverse momentum bin are shown in Table 7.2. Only the systematic uncertainty shown is used to compute the systematic uncertainties on the final cross section.

As a cross-check to the unsmearing factor, the steeply weighted spectrum from Figure 7.12 was smeared. The ratio of the real spectrum to the smeared spectrum is shown with the data in Figure 7.17. This ratio is in agreement within errors to the unsmearing factor obtained using the Bayesian technique in the data.

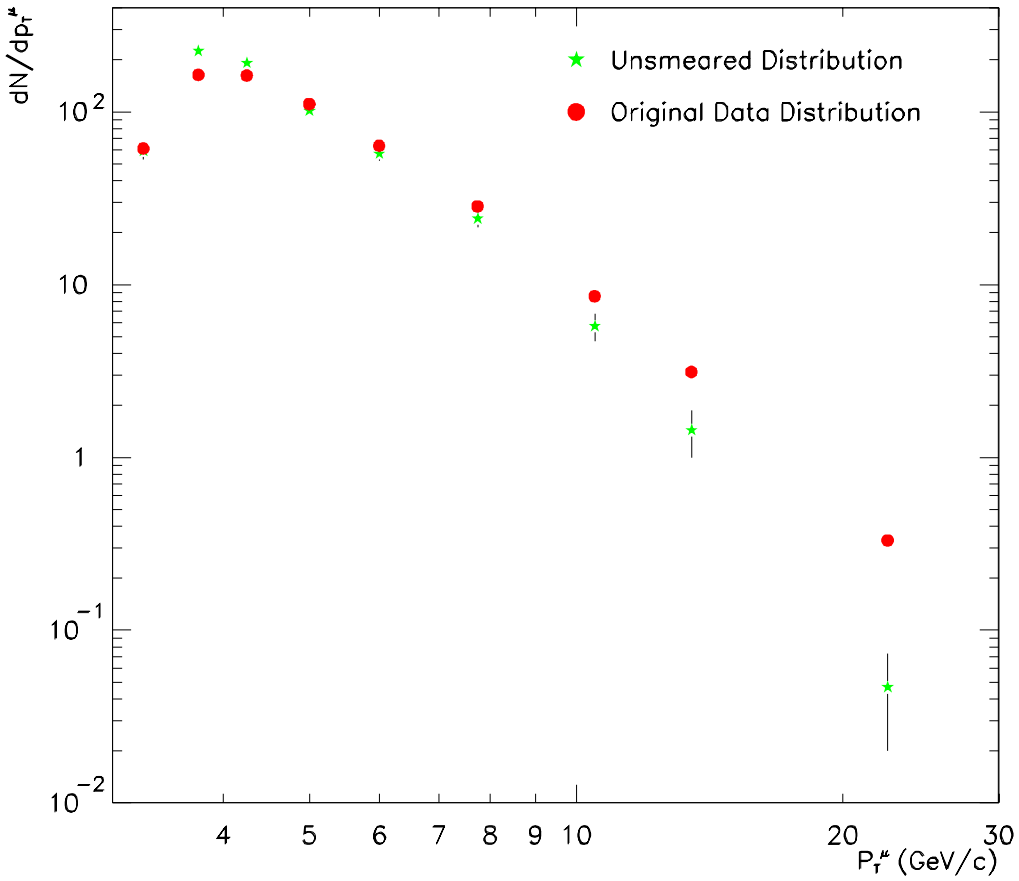

Figure 7.16: The muon transverse momentum spectrum in the data has been unsmeared using Bayes' method. Only statistical errors propagated through the unsmearing matrix are shown.

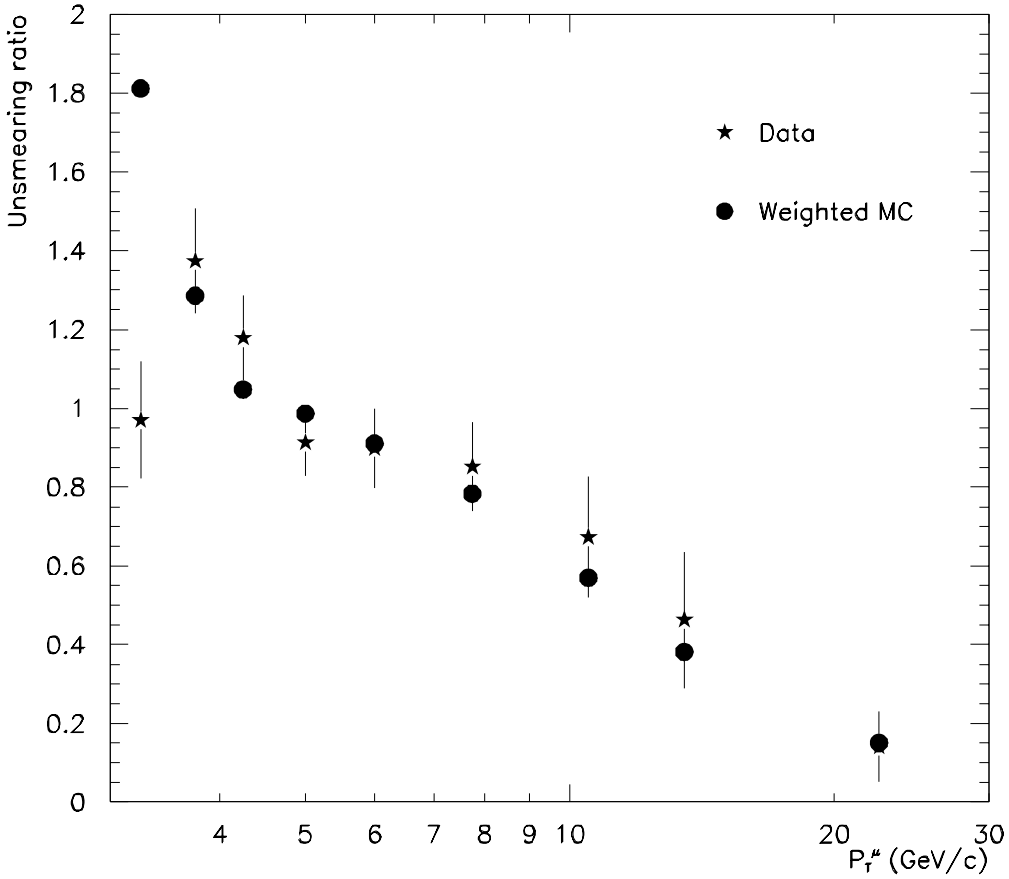

Figure 7.17: The unsmearing correction to the data obtained with Bayes' method. The MC points come from the ratio of real to smeared spectra for a steeply weighted distribution.

CHAPTER 8

CROSS SECTIONS

With the factors obtained using the methods described in the preceding chapters, the b-quark produced muon cross section and the bottom quark production cross section can be obtained. The muon cross section presented in this section is compared to the next-to-leading order (NLO) QCD produced by HVQJET Monte Carlo. The bottom quark production cross section is compared to the direct calculation of the Mangano, Nason, and Ridolfi [15].

All factors used to compute the bottom-produced muon cross section are given in Table 8.1. The systematic errors contributing to the uncertainty on the measured b-produced muon cross section (Figure 8.1) are listed in Table 8.2. Values for both the muon and bottom quark cross sections are listed in Table 8.4. Finally, the systematic error on the bottom quark production cross section (Figure 8.4) is given in Table 8.3.

8.1 Differential b-Produced Muon Cross Section

The differential muon cross section is obtained from the data using the expression

$$\frac{d\sigma^b_\mu}{dp^\mu_{\rm T}} = \frac{1}{\Delta p^\mu_{\rm T}\Delta\eta}\cdot\frac{N_\mu\cdot f_{NC}\cdot f_b\cdot f_{uns}}{A_\phi\cdot\varepsilon\cdot\int\mathcal{L}\cdot dt}, \tag{8.1}$$

where N_μ represents the number of observed muons, f_{NC} is the fraction of muons coming from non-cosmic sources (Figure 6.5), f_b is the fraction of muons originating from the decay of a bottom quark (Figure 6.19), and f_{uns} is the unsmearing factor from Figure 7.17. The correction for the azimuthal acceptance is denoted $A_\phi = 1/4.5$,

p_{T}^{μ} (GeV/c)	N_{μ}	f_{NC}	f_b	f_{uns}	$\int \mathcal{L} \cdot dt \left(\frac{1}{cm^2 s}\right)$	ε	A_{ϕ}
$4 - 4.5$	229	.99	.46	1.17	364	.07	.22
$4.5 - 5.5$	295	.98	.47	.91	364	.094	.22
$5.5 - 6.5$	172	.98	.46	.90	364	.13	.22
$6.5 - 9$	163	.97	.52	.85	364	.14	.22
$9 - 12$	57	.96	.55	.67	364	.17	.22
$12 - 15$	20	.92	.55	.46	364	.22	.22

Table 8.1: Factors used to compute the muon cross section.

while the product of efficiencies from Figure 5.12 is shown in Equation 8.1 as ε. The expression is also scaled by the integrated luminosity $\left(\int \mathcal{L} \cdot dt\right)$, the pseudorapidity region of interest ($\Delta\eta = 1.6$), and the p_{T}^{μ} bin width ($\Delta p_{\mathrm{T}}^{\mu}$). Table 8.1 summarizes the values of the various factors, and the values for the differential b-produced muon cross section are given in Table 8.4.

8.1.1 Systematic Uncertainties on the Muon Cross Section

The systematic uncertainties on the various components that are used to compute the b-produced muon cross section are summarized in Table 8.2. All uncertainties are taken to be uncorrelated and are added in quadrature to obtain the total systematic uncertainty (Δ_{tot}). The uncertainties on the background subtraction techniques (taken from Chapter 6) are denoted Δf_{NC} and Δf_b for the uncertainties on the fraction of non-cosmic muons and the b-fraction respectively. The uncertainty on the unsmearing (Chapter 7) is denoted Δf_{uns}, and the uncertainty on the total overall efficiency (Chapter 5) is denoted $\Delta\varepsilon$. A detailed description of the determination of the 3% uncertainty on the luminosity, labeled $\Delta\mathcal{L}$, can be obtained from [52] and [53]. An additional uncertainty on the measured muon cross section due to the jet energy scale $\left(\Delta E_T^{jet}\right)$ merits further discussion here.

$p_{\rm T}^{\mu}$ (GeV/c)	Δf_{NC}	Δf_b	Δf_{uns}	$\Delta\mathcal{L}$	$\Delta\varepsilon$	ΔE_T^{jet}	Δ_{total}
$4-4.5$	0.2	10	17	3	18	19.7	34
$4.5-5.5$	0.3	9.2	11	3	10	19.7	27
$5.5-6.5$	0.3	11	10	3	13	19.7	28
$6.5-9$	0.3	9.7	8	3	10	19.7	26
$9-12$	0.4	14	15	3	12	19.7	31
$12-15$	0.8	22	43	3	24	19.7	57

Table 8.2: Systematic errors contributing to the uncertainty on the muon cross section. All errors are expressed in percent.

Because the transverse energy of the jet is used in the selection of the sample of muons with associated jets, an incorrect jet energy scale can introduce an uncertainty on the number of muons (N_μ) measured in each $p_{\rm T}^{\mu}$ bin. To examine the effect of the jet energy scale on the final muon cross section, the E_T^{jet} threshold for muon selection was varied to simulate a 10% variation in the jet energy scale. The fractional difference in the number of muons selected in each bin is taken to be the uncertainty on the bottom-produced muon cross section due to the uncertainty in the jet energy scale. An uncertainty of approximately $\Delta E_T^{jet} = 20\%$ (flat in $p_{\rm T}^{\mu}$) is added in quadrature with the other uncertainties on the muon cross section.

8.1.2 Theoretical Prediction and Uncertainties

The central value of the next-to-leading order QCD calculation was obtained using the HVQJET Monte Carlo generator. HVQJET, an implementation of the NLO MNR calculation, is discussed in more detail in Section 3.1.6 and in reference [25]. The central value of the prediction was obtained using the following parameters:

- The mass of the bottom quark (pole mass) is set to $m_b = 4.75$ GeV/c^2.

- The factorization and renormalization scales are set equal and assigned a value of $\mu = \mu_0 = \sqrt{m_b^2 + p_T^2}$.

- The QCD scales, Λ_4 and Λ_5, are taken to be 344 and 237 MeV respectively.

- The Peterson fragmentation parameter takes a value $\varepsilon_b = 0.006$.

- The parton distribution function MRSR2 is chosen for comparison because of an enhancement of bottom production predicted over MRSA'.

The uncertainties on the prediction are obtained by varying the mass of the bottom quark between 4.5 and 5.0 GeV/c^2 and varying the factorization and renormalization scales between $\mu_0/2$ and $2\mu_0$. In addition, the parton distribution function was varied to MRSA', and the Peterson fragmentation parameter ε_b between 0.003 and 0.009. The uncertainty also includes contributions from varying the branching fraction and the decay table used. Interested readers are directed to consult [25] for further details on the uncertainty on the muon cross section.

8.1.3 Comparison of Data to Theoretical Predictions

The differential b-produced muon cross section obtained from the data and the HVQJET theoretical prediction are shown in Figure 8.1. The inner error bars represent the statistical error $\left(1/\sqrt{N_\mu}\right)$, while the larger error bars represent the total systematic and statistical uncertainties added in quadrature. The data exhibit qualitative agreement in shape with the NLO QCD predictions, but lie systematically above the central value of the theoretical prediction. The values and uncertainties plotted for the measured muon cross section are presented in Table 8.4. To facilitate comparison

with theory, Figure 8.2 shows the ratio data/theory. The error band, as well as the measured points and associated errors, have been simply divided by the MNR prediction. A fit of a constant to the ratio points shown in Figure 8.2 yields a value of 2.9 ± 0.4.

8.2 Inclusive b-quark Production Cross Section

The inclusive bottom quark production cross section is calculated from the data using the expression

$$\sigma^b\left(p_{\mathrm{T}}^b > p_{\mathrm{T}}^{\mathrm{min}}\right) = \frac{1}{2}\sigma_b^\mu\left(p_{\mathrm{T}}^{\mu_1}, p_{\mathrm{T}}^{\mu_2}\right)\frac{\sigma_{MC}^b}{\sigma_{MC}^\mu}\Delta\eta, \tag{8.2}$$

where $\sigma_b^\mu\left(p_T^{\mu_1}, p_T^{\mu_2}\right)$ is the measured muon cross section from Equation 8.1 integrated between $p_{\mathrm{T}}^{\mu_1} < p_{\mathrm{T}}^\mu < p_{\mathrm{T}}^{\mu_2}$, σ_{MC}^b represents the total inclusive b-quark cross section for $p_{\mathrm{T}}^b > p_{\mathrm{T}}^{\mathrm{min}}$, and σ_{MC}^μ is the cross section for production of bottom quarks that decay to muons within the p_{T}^μ interval with $p_{\mathrm{T}}^b > p_{\mathrm{T}}^{\mathrm{min}}$. The quantity $p_{\mathrm{T}}^{\mathrm{min}}$ is defined as that value of the b-quark p_{T} for which 90% of the accepted b-quarks (i.e., $b \to \mu$, $|\eta_\mu| < 0.8$, $p_{\mathrm{T}}^{\mu_1} < p_{\mathrm{T}}^\mu < p_{\mathrm{T}}^{\mu_2}$) have transverse momentum greater than $p_{\mathrm{T}}^{\mathrm{min}}$ (Figure 8.3). The factor of two corrects the data, which contains muons originating from both b and $\overline{b}$ decays, to a cross section of bottom quarks only. This method of representing the cross section is the method employed by UA1 [5].

8.2.1 Systematic Uncertainties on the Bottom Quark Production Cross Section

The systematic uncertainties propagated through to the final bottom quark production cross section are shown in Table 8.3. The factor σ_b/σ_μ used to convert from the

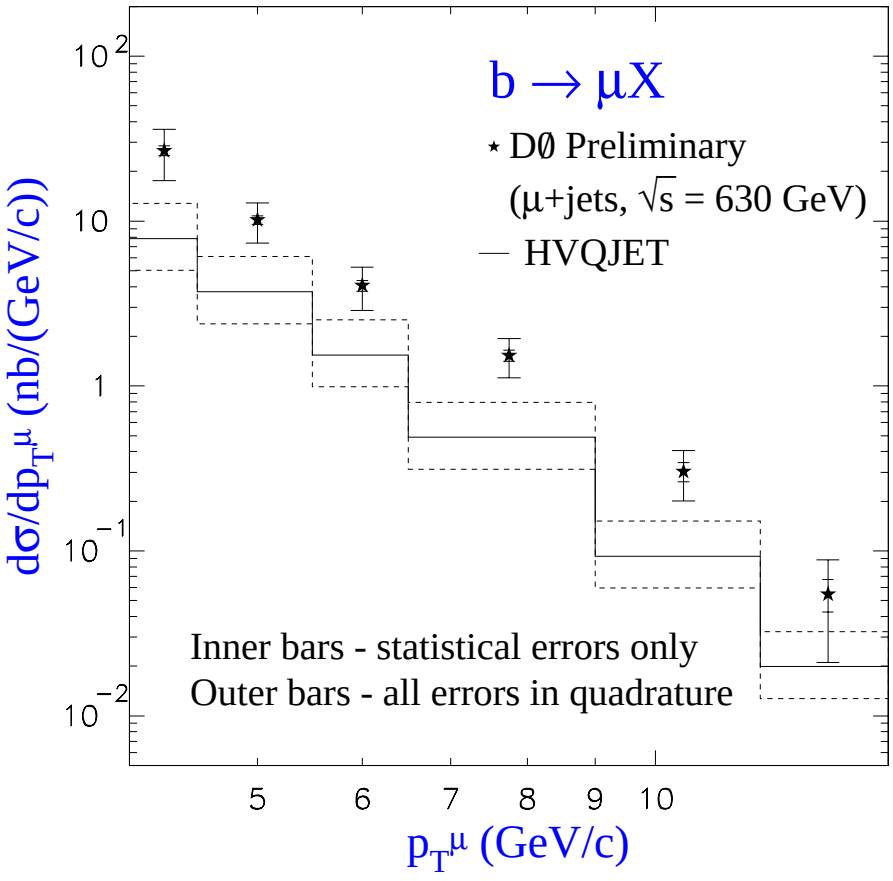

Figure 8.1: The bottom quark produced muon cross section per unit η for muons with $|\eta| < 0.8$ compared to HVQJET predictions. The uncertainties on the measured points are statistical (inner) and statistical and systematic added in quadrature (outer).

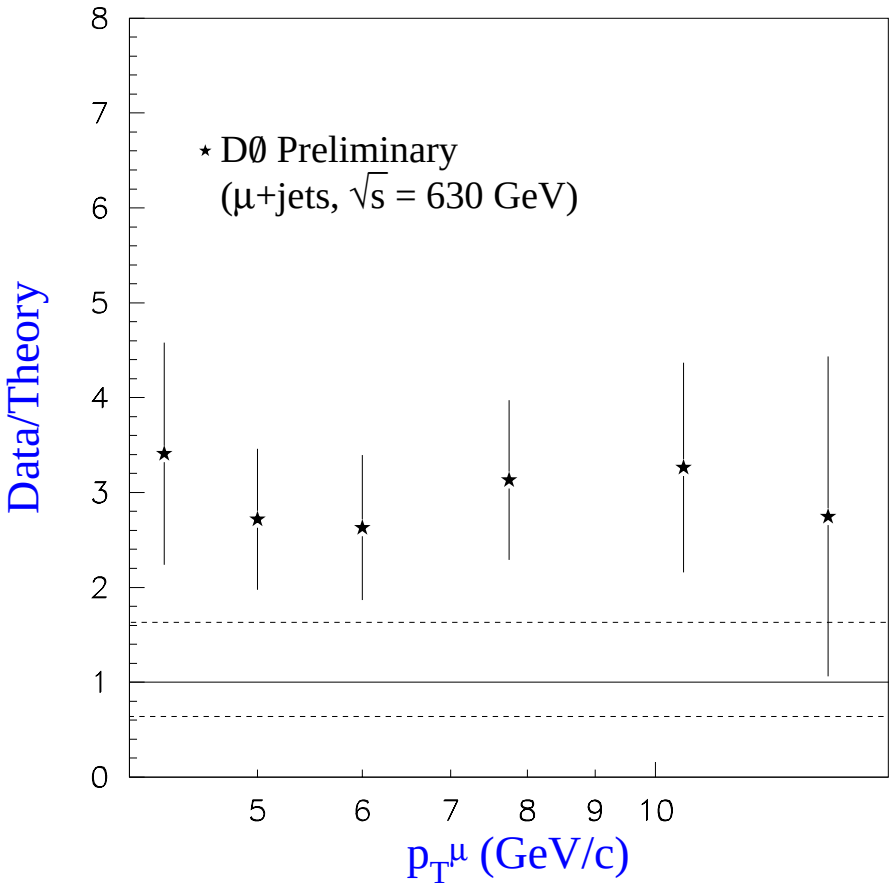

Figure 8.2: The ratio data/theory for the b-quark produced muon cross section as a function of muon transverse momentum. All quantities from the previous plot have been divided by the central value of the NLO prediction. Overall, the data lie a factor of 2.9 above the theoretical prediction.

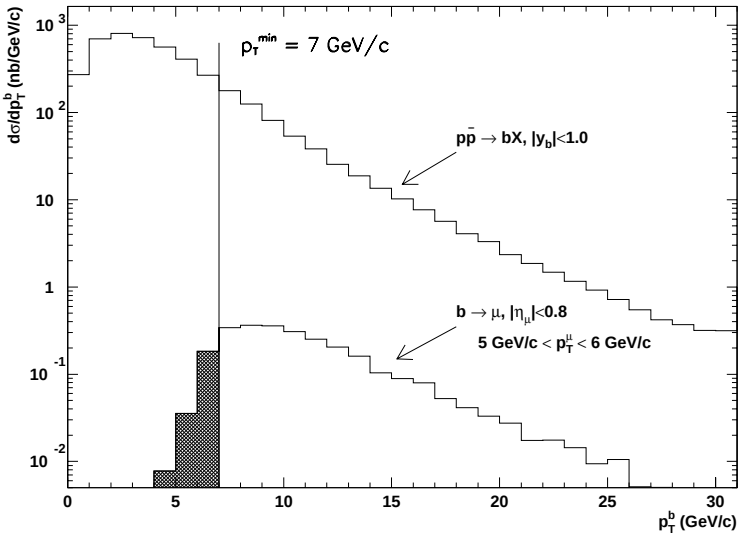

Figure 8.3: Determination of $p_{\mathrm{T}}^{\mathrm{min}}$ (see text for description).

muon cross section to the bottom quark cross section also introduces uncertainties. The quantities varied to obtain the uncertainty on the conversion factors ($\Delta\sigma_b/\sigma_\mu$) include the b mass ($\sim$ 4%), the μ scale ($\sim$ 2%), the parton distribution function ($\sim$ 2%), the $b \rightarrow \mu$ branching fraction ($\sim$ 4%), the Peterson fragmentation parameter ($\sim$ 10%), and the B meson decay table ($\sim$ 28%). The parameter variations are the same as those used in the determination of the uncertainties on the NLO QCD calculation of the b-produced muon cross section. Further details of the uncertainty calculation can also be found in [25]. The total uncertainty on the bottom quark production cross section is obtained by combining the relative systematic uncertainties on the b-produced muon cross section and the uncertainties on the conversion factors in quadrature.

p_{T}^{μ} (GeV/c)	$p_{\mathrm{T}}^{\mathrm{min}}\left(\frac{\mathrm{GeV}}{\mathrm{c}}\right)$	Δ_{total}	$\Delta\sigma_b/\sigma_\mu$	$\Delta\sigma^b$
$4-4.5$	5.5	34	30	45
$4.5-5.5$	6.6	27	30	40
$5.5-6.5$	8	28	30	41
$6.5-9$	10.1	26	30	39
$9-12$	13.4	31	30	43
$12-15$	19	57	30	64

Table 8.3: Uncertainty on the final bottom quark cross section due to the systematic uncertainty in the muon cross section and the conversion factors. All errors are expressed in percent.

8.2.2 NLO QCD Prediction and Uncertainties

The theoretical calculation of the bottom quark production cross section is somewhat simpler than that for the b-produced muon cross section, because there are no uncertainties introduced by decaying the produced b-quark to a muon. The central value of the NLO prediction for the bottom quark production cross section was obtained using the HVQJET Monte Carlo event generator and the MRSR2 parton distribution function. In addition, we use a bottom quark mass $m_b = 4.75$ GeV/c^2 (pole mass) and a factorization/renormalization scale of $\mu_0 = \sqrt{m_b^2 + p_{\mathrm{T}}^2}$.

The uncertainties on the theoretical calculation of the bottom quark production cross section shown in Figure 8.4 originate from varying the mass of the bottom quark and the factorization and renormalization scale. The upper curve is obtained with the values $m_b = 4.5$ GeV/c^2 and $\mu = \mu_0/2$, while the lower uncertainty is obtained using $m_b = 4.5$ GeV/c^2 and $\mu = 2\mu_0$.

8.2.3 Comparison of Data to Theoretical Predictions

The bottom quark production cross section obtained from the data is compared to the HVQJET prediction in Figure 8.4. The inner error bars represent the statistical error

p_{T}^{μ} $\left(\frac{GeV}{c}\right)$	$p_{\mathrm{T}}^{\min}$ $\left(\frac{GeV}{c}\right)$	$\frac{d\sigma_b^{\mu}}{dp_{\mathrm{T}}^{\mu}}$ $\left[\mathrm{nb}\cdot\left(\frac{GeV}{c}\right)^{-1}\right]$	$\sigma_{MC}^{b}/\sigma_{MC}^{\mu}$	$\sigma^{b}\left(p_{\mathrm{T}}^{b} > p_{\mathrm{T}}^{\min}, \lvert y\rvert < 1\right)$ (nb)
$4 - 4.5$	5.5	$26.8 \pm 1.8 \pm 9.0$	327 ± 98.1	$3504 \pm 231 \pm 1581$
$4.5 - 5.5$	6.6	$10.1 \pm .59 \pm 2.7$	226 ± 67.8	$1839 \pm 107 \pm 737$
$5.5 - 6.5$	8	$4.06 \pm .31 \pm 1.1$	321 ± 96.3	$1045 \pm 78 \pm 428$
$6.5 - 9$	10.1	$1.53 \pm .12 \pm .39$	193 ± 57.9	$590 \pm 46 \pm 233$
$9 - 12$	13.4	$.303 \pm .040 \pm .09$	304 ± 91.2	$221 \pm 29 \pm 95$
$12 - 15$	19	$.055 \pm .012 \pm .031$	345 ± 103.5	$45 \pm 10 \pm 29$

Table 8.4: A summary of the cross section results. For the cross section results, the first error is statistical; the second is systematic.

$\left(1/\sqrt{N_{\mu}}\right)$, while the larger error bars represent the total systematic and statistical uncertainties added in quadrature. The data exhibit qualitative agreement in shape with the NLO QCD predictions, but lie systematically above the central value of the theoretical prediction. The values and uncertainties plotted for the measured bottom quark production cross section are presented in Table 8.4. To facilitate comparison with theory, Fig. 8.5 shows the ratio data/theory for the bottom quark cross section. The error band, as well as the measured points and associated errors, have been simply divided by the MNR prediction. A fit of a constant to the ratio points shown in Figure 8.5 yields a value of 2.4 ± 0.5.

A careful reader will notice the discrepancy between the excess observed in the muon cross section and the excess found in the bottom quark production cross section. While the bottom cross section is compared directly to the MNR calculation, the muon cross section is compared to the HVQJET prediction. HVQJET predicts a smaller bottom quark production cross section than the actual MNR calculation by 10 to 20 percent [25]. The effect cancels in the ratio σ_b/σ_{μ}, however, so our comparison to the bottom quark cross section is the value we report.

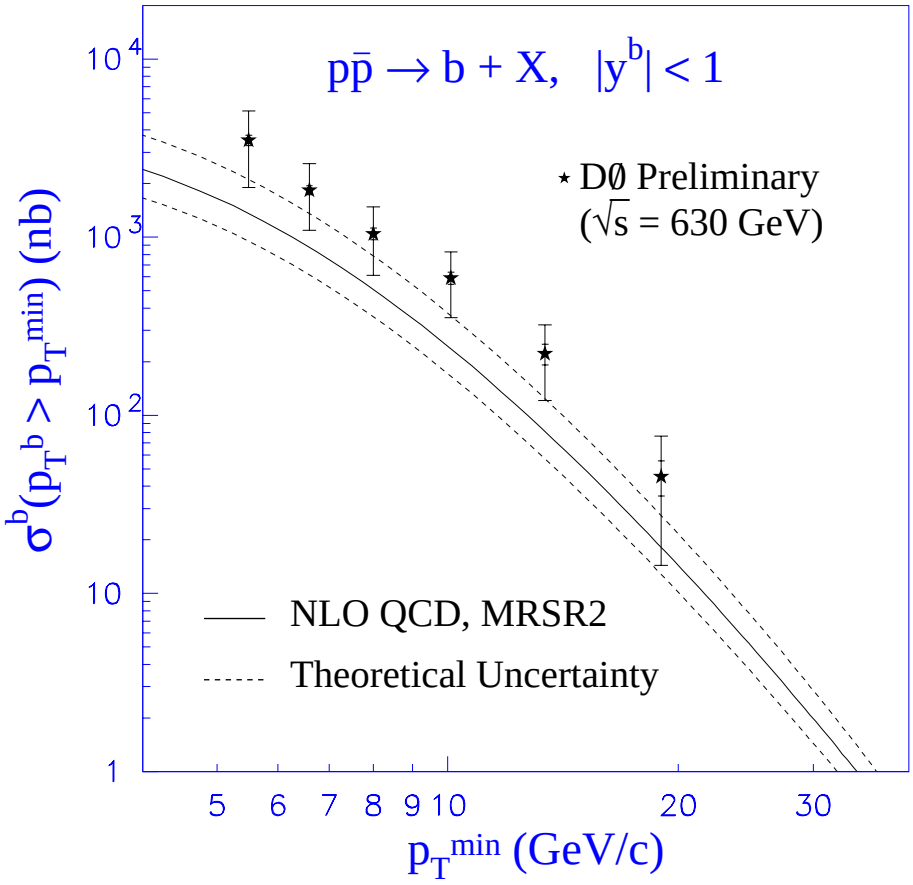

Figure 8.4: The inclusive bottom quark production cross section for $|y_b| < 1$ at $\sqrt{s} = 630$ GeV compared to NLO QCD predictions. The uncertainties on the measured points are statistical (inner) and statistical and systematic added in quadrature (outer). The uncertainty on the HVQJET predictions arise from variation of the b-quark mass and the factorization and renormalization scales.

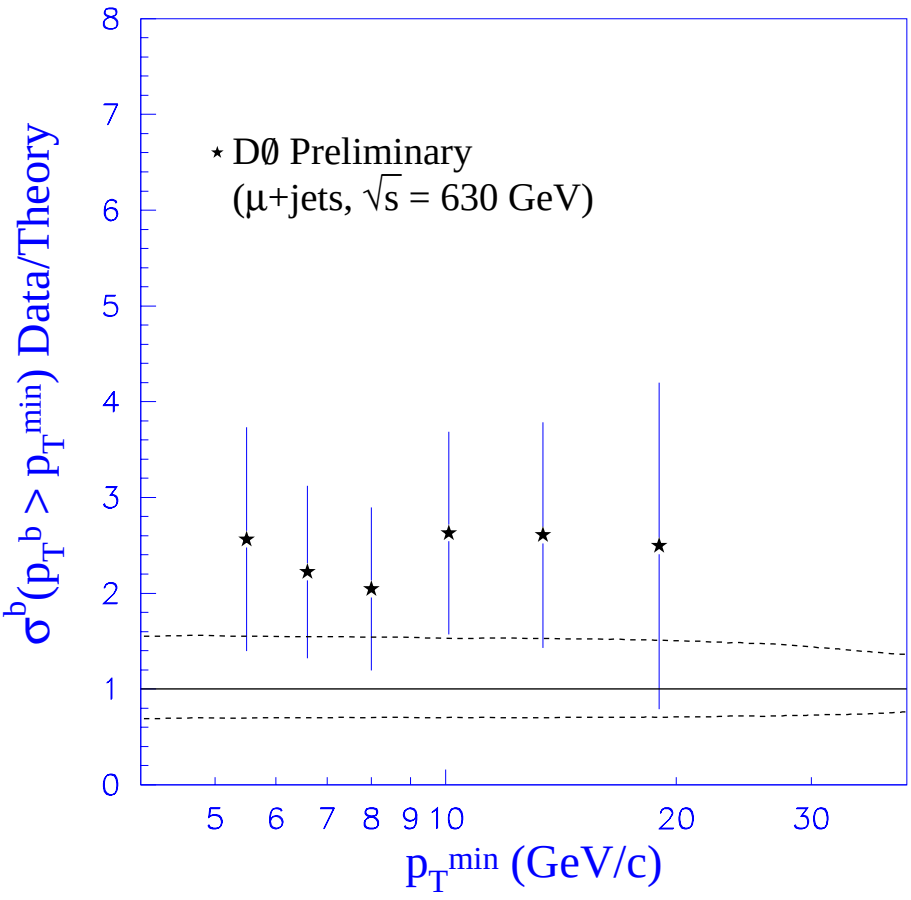

Figure 8.5: The ratio data/theory for the b-quark production cross section as a function of $p_{\mathrm{T}}^{\mathrm{min}}$. All quantities from the previous plot have been divided by the central value of the NLO prediction. Overall, the data lie a factor of 2.4 above the theoretical prediction.

8.3 Summary

This chapter summarizes the measurement of the bottom-produced muon cross section and the inclusive bottom quark production cross section. Both measurements exhibit qualitative shape agreement with NLO QCD predictions. The measured data, however, exhibit a systematic normalization excess above the predictions. In the next chapter, these measurements are compared to other measurements, both from the inclusive muon analysis at DØ and measurements made by other experiments.

CHAPTER 9

DISCUSSION OF RESULTS

This dissertation provides a measurement of bottom quark production at a center of mass energy of $\sqrt{s} = 630$ GeV. The data, collected using the DØ detector at the Tevatron $p\overline{p}$ collider at Fermilab in December of 1995, correspond to an integrated luminosity of 364 nb^{-1}.

The muon sample used in this analysis was collected using a trigger requiring a single central muon with transverse momentum greater than 3 GeV/c. In addition, each event was subjected to a set of offline selection criteria designed to enrich the muon sample in muons originating from the decay of a b-quark and reduce the background due to cosmic rays and detector noise. The requirement of a nearby jet with transverse energy greater than 12 GeV removes contributions from Υ decay, Drell-Yan production, and cosmic ray muon contamination, because these processes generally produce isolated muons. The jet requirement also allows a determination of the fraction of muons from bottom quark decays from the data sample.

The contribution of cosmic rays to the observed number of muons is estimated using timing information from scintillators installed during the 1994-95 Tevatron Collider run. The difference between the measured and expected times-of-flight through the detector is used to determine the amount of cosmic contamination as a function of muon transverse momentum.

Requiring the muon to be associated with a jet with $E_T > 12$ GeV jet also provides a way of discriminating b-produced muons from those originating from π/K in-flight

decay or the decay of a charm quark. The distribution of the muon momentum relative to the jet axis $\left(p_{\mathrm{T}}^{rel}\right)$ is used to separate the bottom produced muon signal from the charm and π/K background. The distributions of signal and background are used as input to a maximum-likelihood fit that determines the fraction of muons in the sample coming from bottom decays. The b-fraction obtained in this manner is compatible with ISAJET Monte Carlo predictions for heavy quark and π/K decay.

After obtaining the background-subtracted muon spectrum, the spectrum is unsmeared for detector resolution effects using a Bayesian statistical technique. After obtaining the real b-produced muon transverse momentum spectrum, the spectrum is corrected for selection and trigger efficiencies and acceptances, as well as the integrated luminosity. The measured b-produced muon cross section is then compared with NLO QCD predictions. The measured spectrum exhibits good qualitative shape agreement with theoretical predictions. The normalization exceeds the predictions, however, by a factor of 2.9 ± 0.4.

To obtain the bottom quark production cross section, HVQJET Monte Carlo is used to generate factors $\sigma_{MC}^{b}/\sigma_{MC}^{\mu}$ used to convert the b-produced differential muon cross section to the b-quark cross section, $\sigma^{b}\left(p_{\mathrm{T}}^{b} > p_{\mathrm{T}}^{\mathrm{min}}, |y| < 1.0\right)$. The quantity $p_{\mathrm{T}}^{\mathrm{min}}$ is defined as the value of the b-quark p_T for which 90% of the b-quarks producing muons passing kinematic selection criteria have a transverse momentum greater than $p_{\mathrm{T}}^{\mathrm{min}}$. The bottom quark production cross section also exhibits good qualitative agreement with NLO predictions, while the excess for the bottom quark production cross section normalization is 2.4 ± 0.5. The following sections discuss this result in the context of other measurements of bottom quark production.

9.1 Comparison to the Inclusive Muon Analysis

DØ has also made a measurement of the bottom quark production cross section at $\sqrt{s} = 630$ GeV using a sample of single muons [45]. This section serves to briefly describe the analysis and compare the results to those presented in Chapter 8.

Significantly more cosmic ray muon contamination is present in the single muon analysis, because the muons are not associated with a jet. The cosmic ray muon background is removed using scintillator timing information, similar to the procedure outlined in in Chapter 6. The remainder of the background selection is handled quite differently. The contribution from pion and kaon decay is first removed using ISAJET Monte Carlo tuned to CDF and UA1 charged particle data, and the b-fraction is taken from ISAJET TWOJET Monte Carlo.

The unsmearing of the muon momentum spectrum is obtained by taking the ratio of generated to reconstructed muon p_T spectra. The unsmearing factor obtained in this manner is compatible within errors to the unsmearing factor obtained using the Bayesian method outlined in Chapter 7.

Once the bottom-produced muon cross section is obtained for the single muon analysis, factors are obtained using HVQJET to convert the muon cross section to an inclusive bottom quark production cross section. The procedure is identical to that described in Chapter 8. The bottom quark production cross section for the single muon analysis is shown with the results from Chapter 8 in Figure 9.1. The two measurements agree quite well over the range of bottom quark p_{T} sampled.

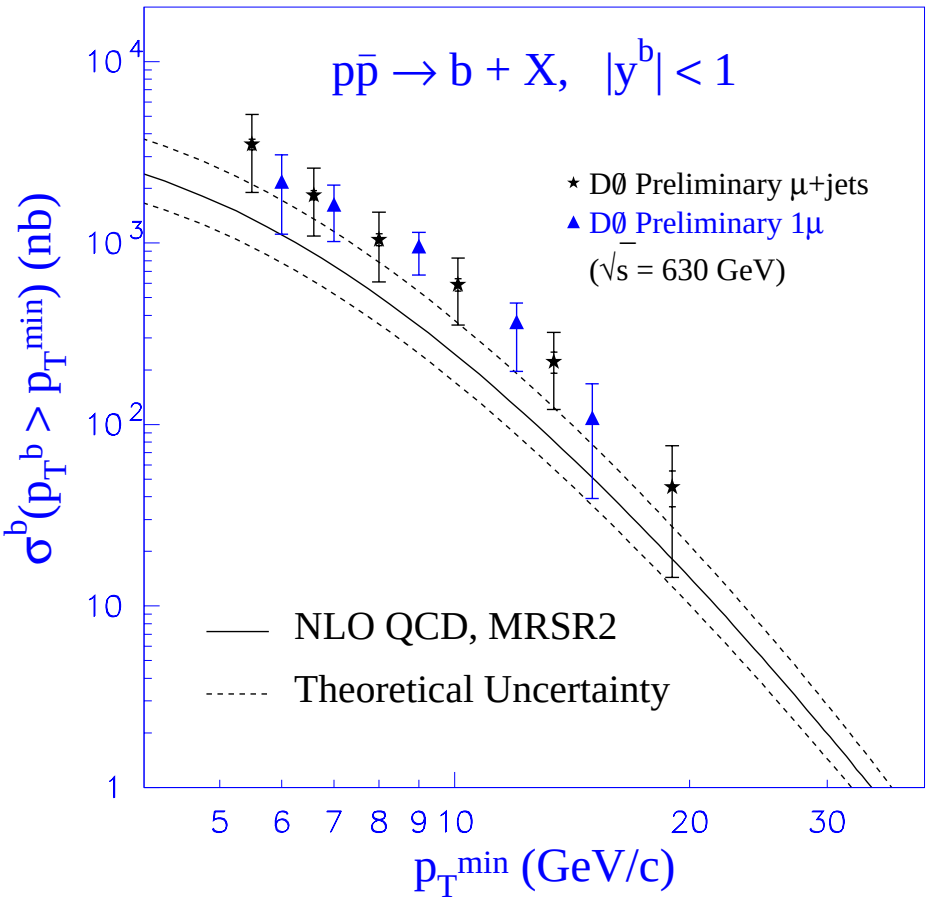

Figure 9.1: Inclusive bottom quark production cross section for both the single muon analysis and the muon plus jets analysis. The inner error bars are statistical. The outer error bars are statistical and systematic added in quadrature. The NLO QCD prediction and its associated errors are described in detail in Chapter 8.

9.2 Comparison to UA1 and CDF Measurements

Other measurements of the bottom quark production cross section at $\sqrt{s} = 630$ GeV have been made by the UA1 collaboration [54] and, more recently, the CDF collaboration [55]. This section serves to compare the results of all three collaborations on a single plot.

An analysis of 4.7 pb^{-1} of muon data recorded by the UA1 collaboration during 1988-89 at a center of mass energy of $\sqrt{s} = 630$ GeV exhibited somewhat better agreement with theoretical predictions available at the time. These measurements come from an analysis of bottom production via four independent decay channels, including muon-jet data, and use a similar technique of signal extraction using the variable p_{T}^{rel}. The UA1 muon-jet data sample requires a muon with a transverse momentum above 10 GeV/c and a jet E_T greater than 10 GeV.

Because UA1 measures the b-quark production cross section for $|y_b| < 1.5$, the UA1 measurements can not be directly compared to the results of this analysis. Instead, the data presented in the preceding sections must be corrected for the rapidity difference before a fair comparison may be made. First, HVQJET events are generated to obtain the cross section predictions for $\sigma^b\left(p_{\mathrm{T}}^b > p_{\mathrm{T}}^{\mathrm{min}}, |y| < 1.0\right)$ and $\sigma^b\left(p_{\mathrm{T}}^b > p_{\mathrm{T}}^{\mathrm{min}}, |y| < 1.5\right)$ as a function of $p_{\mathrm{T}}^{\mathrm{min}}$. The ratio is then fit with a third degree polynomial (Figure 9.2) and evaluated at each $p_{\mathrm{T}}^{\mathrm{min}}$ value to obtain a multiplicative factor $f_{1.5/1.0}$.

The CDF collaboration at Fermilab has also measured the inclusive bottom quark production cross section at 630 GeV. They use a sample of muons with transverse momenta above 6.2 GeV/c. Because CDF has a central magnetic field and silicon vertex detector, no jets are required in the sample. CDF exploits the relatively long

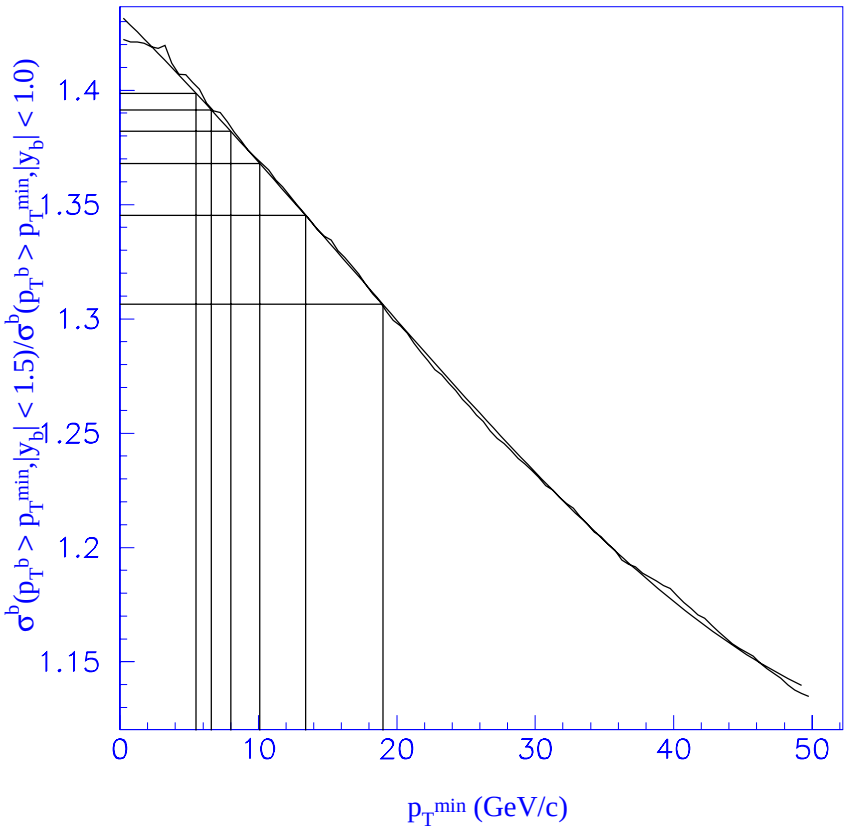

Figure 9.2: MNR predictions for the ratio of bottom production with $|y_b| < 1.5$ to that with $|y_b| < 1.0$. The lines show the evaluated values for the corresponding values of p_T^{min}.

lifetime of the bottom quark and performs impact parameter fits to determine their bottom quark signal. CDF corrects their measurement to correspond to the same rapidity range as the UA1 measurement.

In Figure 9.3, the bottom quark production cross section recomputed using the rapidity correction (presented in Table 9.1) is directly compared to both the UA1 and CDF measurements of the inclusive bottom quark production cross section at $\sqrt{s} = 630$ GeV. The MNR prediction shown in the figure is the HVQJET prediction for $|y_b| < 1.5$. The uncertainty on the theoretical prediction is estimated varying the mass of the bottom quark and the factorization and renormalization scales as in Chapter 8.

The DØ muon plus jets measurement is in good agreement with the CDF measurement; both Tevatron measurements lie approximately a factor of 2.5 above the central value of the NLO QCD predictions. The central values of the UA1 measurement lie along the upper uncertainty band on the prediction. While the measurements agree within error, the difference in the central values deserves comment here.

The discrepancy between the UA1 measurements and the Tevatron measurements can be explained at least in part by recent experimental data on B hadron decays made by the CLEO collaboration. When the most recent measurements are included in theoretical predictions, the cross section for muons with $p_{\mathrm{T}}^{\mu} > 3.0$ GeV/c is reduced by 40%. This modification has the effect of inflating the conversion factors $\sigma_{MC}^{b}/\sigma_{MC}^{\mu}$ by about 60%. The increase in conversion factors would tend to increase the UA1 measurement of the bottom quark production cross section. It is not simply enough to multiply the UA1 measured points by a factor of 1.6, however, because different measurement channels may be affected differently. In summary, then, we contend

$p_{\mathrm{T}}^{\mathrm{min}}$ $\left(\frac{GeV}{c}\right)$	$\sigma^b\left(p_{\mathrm{T}}^b > p_{\mathrm{T}}^{\mathrm{min}}, \lvert y\rvert < 1\right)$ (nb)	$f_{1.5/1.0}$	$\sigma^b\left(p_{\mathrm{T}}^b > p_{\mathrm{T}}^{\mathrm{min}}, \lvert y\rvert < 1.5\right)$ (nb)
5.5	$3504 \pm 231 \pm 1614$	1.399	$4901 \pm 323 \pm 2257$
6.6	$1839 \pm 107 \pm 757$	1.391	$2559 \pm 149 \pm 1053$
8	$1045 \pm 78 \pm 444$	1.382	$1445 \pm 110 \pm 614$
10.1	$590 \pm 46 \pm 245$	1.368	$807 \pm 63 \pm 336$
13.4	$221 \pm 29 \pm 108$	1.345	$298 \pm 39 \pm 146$
19	$45 \pm 10 \pm 34$	1.306	$59 \pm 13 \pm 44$

Table 9.1: A summary of the cross section results. The first error is statistical; the second is systematic.

that all measurements at 630 GeV agree within errors.

9.3 Bottom Quark Production Cross Section at 1.8 TeV

The bottom quark production cross section has also been measured in $p\overline{p}$ collisions at the Tevatron for a center-of-mass energy $\sqrt{s} = 1.8$ TeV. DØ measurements in both the inclusive muon and the dimuon channel are shown in Figure 9.4. Both measurements are made for $|y^b| < 1.0$ using muons in the central region of the detector. As in the 630 GeV analyses, the cross sections for both data samples agree in shape with the next-to-leading order QCD predictions, but exceed the central value of the theory by a factor of 2.5.

The observed excess suggests that while the absolute normalization predicted by the MNR calculation does not describe inclusive bottom quark production as a function of $p_{\mathrm{T}}^{\mathrm{min}}$, the energy dependence may be correctly predicted by the theory. This observation also suggests a natural extension to this analysis: a measurement of the energy dependence of the bottom quark production cross section.

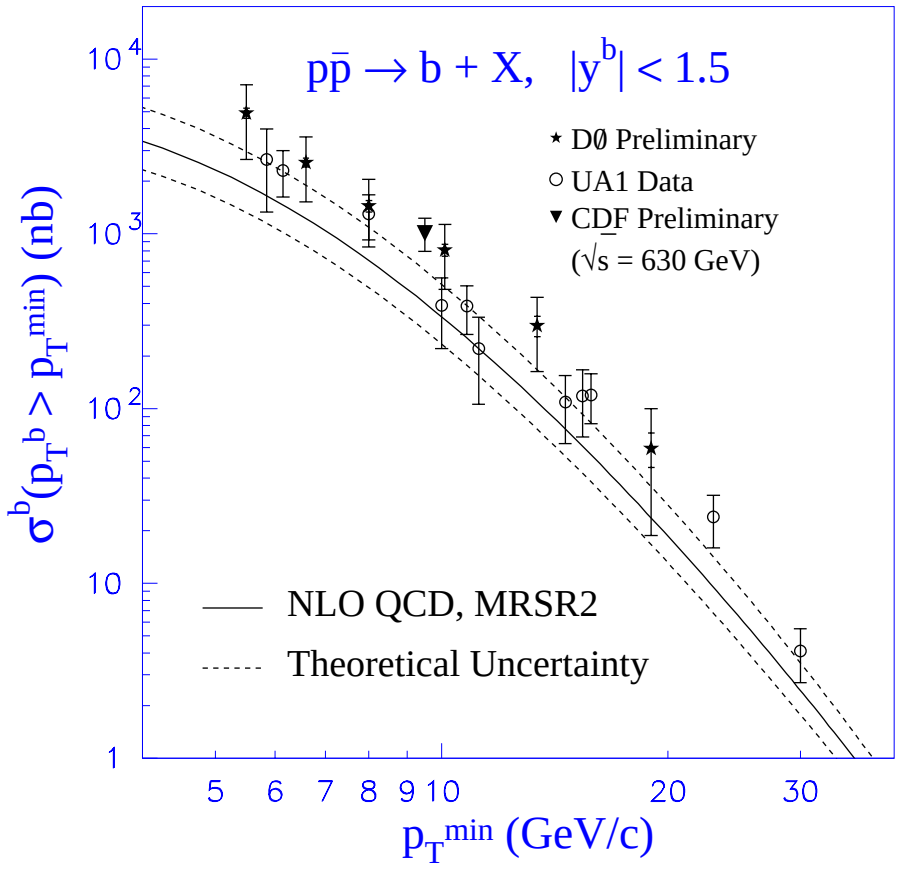

Figure 9.3: Measurement of the bottom quark production cross section for $\sqrt{s} = 630$ GeV and $|y_b| < 1.5$ for DØ, CDF, and UA1.

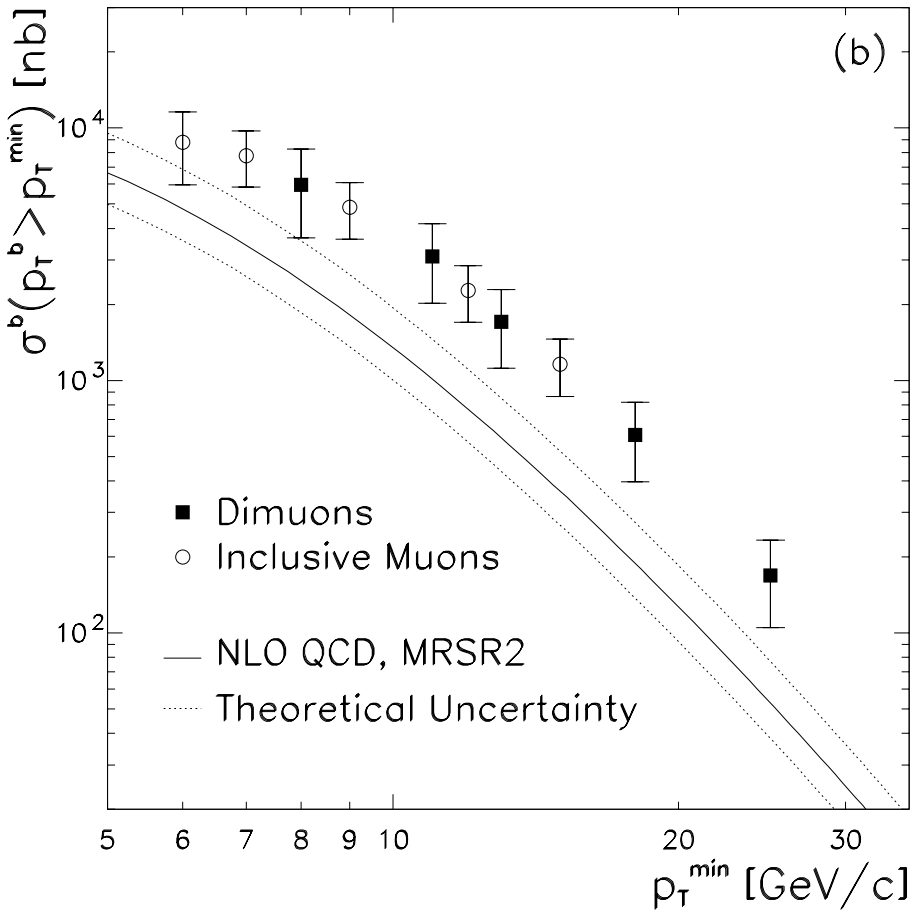

Figure 9.4: The bottom quark production cross section for $\sqrt{s} = 1.8$ TeV in the dimuon and inclusive muon channels. The theoretical curve shown is the MNR prediction from HVQJET.

9.3.1 Energy Dependence of the Bottom Quark Production

A natural extension to the analysis presented in this dissertation would involve measuring the bottom quark production cross section using a sample of muons plus associated jets obtained at a center-of-mass energy of 1.8 TeV. Such a measurement permits a precision study of the energy dependence of bottom production. In the ratio of 630 and 1800 GeV cross sections, completely and partially correlated systematic uncertainties can cancel, reducing the overall systematic uncertainty on the ratio. This measurement has already been performed for the inclusive muons analysis at DØ, and is shown with a similar measurement for CDF in Figure 9.5. The measured ratio of cross section agrees well with the central value of the NLO predictions and the CDF measurement, although no errors have been cancelled in this plot.

9.4 Current State of Theoretical Calculations

The inclusive bottom quark production cross section, both at 1.8 TeV and 630 GeV, is measured to be a factor of 2.5 higher than NLO calculations of perturbative QCD. This discrepancy is well established and has plagued heavy quark theorists for over ten years.

Naively, one might expect that perhaps a NNLO (next-to-next-to-leading order) calculation might help resolve the discrepancy between experiment and theory, because in the absence of significant higher order corrections to the cross section, the choice of scale should be a free parameter. A full NNLO QCD calculation for bottom quark production, however, is currently unavailable.

The answer does not lie in the choice of parton distribution function, either.

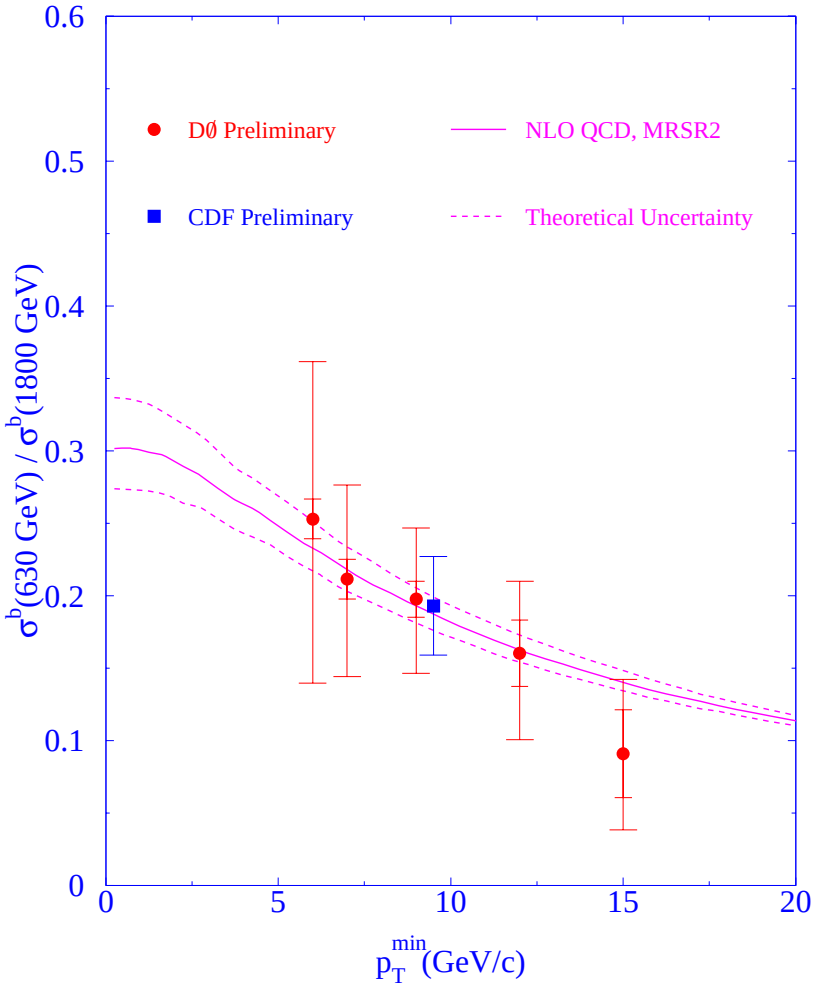

Figure 9.5: The ratio $\sigma^b_{630}/\sigma^b_{1800}$ for the single muon analysis. The data exhibit good agreement with the CDF measurement. The measurement also agrees well with the central value of the NLO QCD prediction.

Calculations of the effect of varying the parton distribution function [25] suggest that, within the choices that best describe current experimental data from other sources, one observes at most a 20% variation in the measured cross section.

Furthermore, a measurement of forward bottom quark production [57] made at DØ using muons detected in the rapidity range $2.4 < |\eta^{\mu}| < 3.2$ indicates an excess of a factor of 4 over central theoretical predictions (Figure 9.6). No phenomenon of perturbative origin (higher order corrections, for example) can explain this discrepancy [56].

A study of b-quark jets at DØ, the results of which are still preliminary and not publicly available, suggest that at larger values of b-quark p_{T}, theory and experiment may converge (Figure 9.7). If the results are correct, the discrepancy between theory and experiment could be an artifact of trying to predict the cross section at transverse momentum values that are too low for the theory. Run II of the Tevatron, scheduled to begin in early 2001, should increase the statistics and extend the reach of this measurement in bottom quark p_{T} to allow a more definite statement to be made.

9.5 Summary and Future Prospects

The measurement of the inclusive bottom quark production cross section at $\sqrt{s} = 630$ GeV presented in this thesis agrees with both the UA1 and CDF measurements. The overall shape of the cross section agrees well with that predicted by the NLO MNR calculation. The normalization differs by roughly a factor of 2.5, compatible with the excess observed at 1800 GeV. No satisfactory explanation currently exists for this normalization discrepancy. This final section presents a look to the future, with an

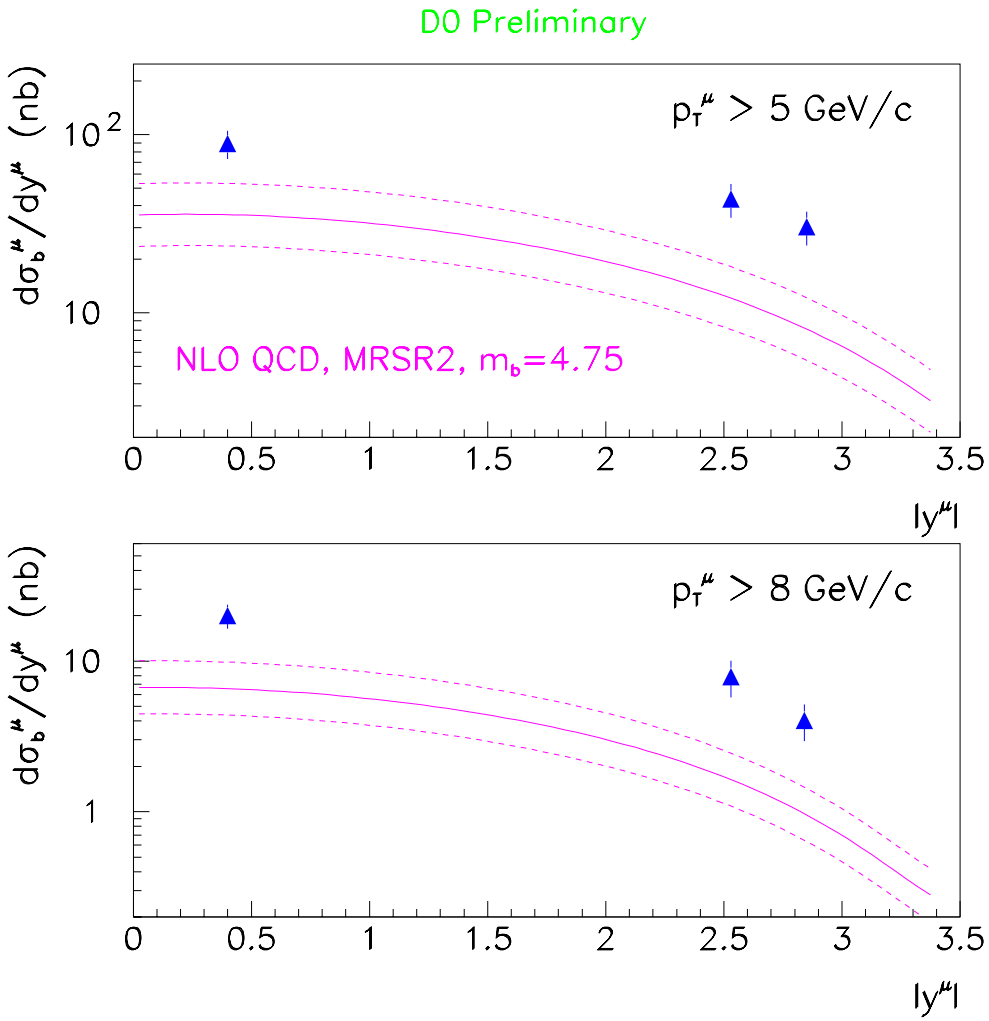

Figure 9.6: DØ measurements of rapidity dependence of the bottom quark production cross section at $\sqrt{s} = 1.8$ TeV. The curves shown in the figure are the HVQJET predictions of the NLO QCD calculation.

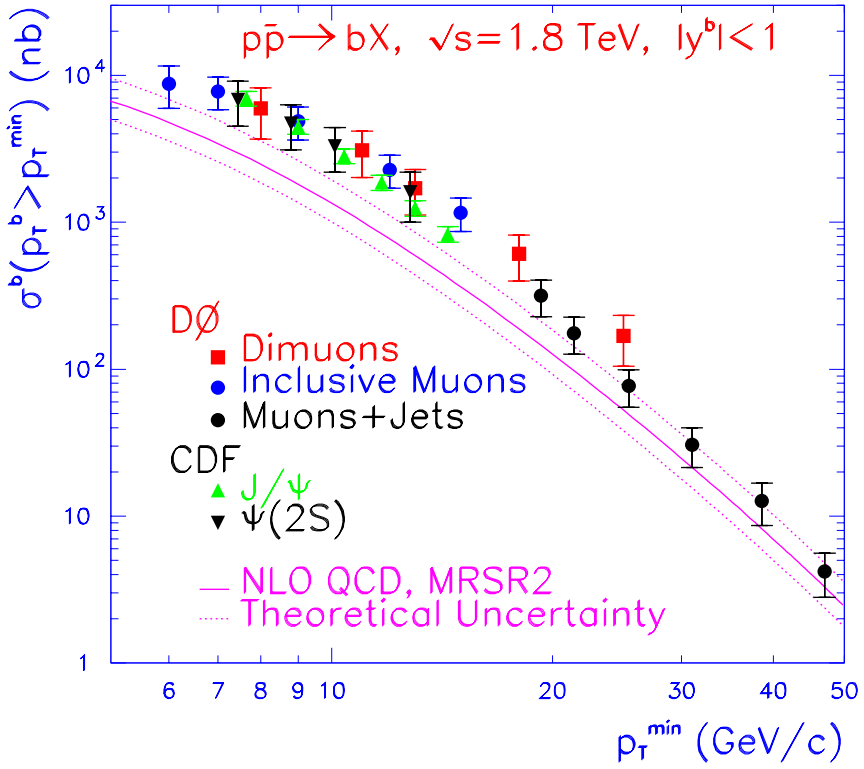

Figure 9.7: Preliminary measurement of the bottom quark production cross section using b-jets at $\sqrt{s} = 1.8$ TeV. The figure also serves to compare Tevatron measurements of bottom quark production.

emphasis on bottom quark physics at DØ.

9.5.1 Tevatron, Take Two

The Fermilab Tevatron is currently scheduled to begin running in collider mode for data taking sometime in November 2001. During this running period, called Run II, the Tevatron will operate at a center-of-mass energy of 2 TeV with an instantaneous luminosity of $2 \times 10^{32}\ cm^{-2}s^{-1}$ (implying the production of $10^{11}\ b\bar{b}$ pairs per year of operation). The DØ collaboration is currently in an upgrade phase, preparing for the start of Run II. The upgraded DØ detector will be better suited to making precision bottom quark measurements.

First, the upgraded DØ detector will have a central magnetic field. A 2 tesla solenoid, combined with all new tracking in the central detector, will provide improved particle momentum resolution for all charged particles. From the value of the field integral and the precision provided by the central tracking detectors, the momentum resolution should be [58]:

$$\frac{\Delta p_{\mathrm{T}}}{p_{\mathrm{T}}^2} = 0.002, \tag{9.1}$$

thereby decreasing the uncertainty in the momentum measurement and reducing the systematic error associate with muon momenum spectrum unsmearing.

Second, DØ is installing a silicon vertex detector around the interaction region. The vertex detector, consisting of silicon disks and barrels, will provide coverage for particles out to $|\eta| < 3$. The silicon vertex detector will allow a precise determination of secondary vertex position to 10 μm in $x - y$, and 30 μm in z. Knowledge of the secondary vertex position allows bottom quark tagging without the use of the variable p_{T}^{rel}, by exploiting the relatively long lifetime of the B hadrons.

Last, the DØ upgrade includes a vastly improved muon system. Triggering in the central muon system ($|\eta| < 1$) is aided by the addition of scintillation counters, and the efficiency of the central tracking chambers will be maintained. In the forward ($1 < |\eta| < 2.5$) muon system, improved tracking will be realized with the addition of 1 cm $\times$ 1 cm tracking chambers. In the forward region, triggering will be improved with three layers of pixel scintillator counters (segmentation $0.1 \times 4.5^\circ$ in $\eta - \phi$). All new triggering electronics will enable collection of very large single and dimuon data sets for use in bottom quark studies.

9.5.2 Future Measurements

The Run II physics program will continue to include tests of perturbative QCD calculations such as the one presented in this dissertation. DØ will measure the inclusive bottom quark production cross section in a variety of channels (J/ψ, single leptons, dimuons) as well as correlations (dilepton $\Delta\phi$, muon+jet, forward-central), which are sensitive to various NLO production mechanisms. The upgraded detector, however, facilitates a variety of new bottom quark measurements at DØ.

In Run II, the Tevatron will produce all species of B hadrons, including the B_c, recently observed by the CDF collaboration [59]. DØ will be able to do B spectroscopy to identify the various flavors of B mesons, providing measurements of exclusive bottom quark decay modes.

With improved particle identification and momentum resolution, DØ will also be able to directly probe the kinematics of the B mesons produced, facilitating a measurement of the differential bottom quark production cross section as a function of b-jet E_{T}. Such a measurement can be converted using NLO QCD predictions into

an integrated inclusive production cross section that probes large values of bottom quark p_{T}, perhaps out to 100 GeV/c.

In addition to the various aspects of bottom quark production, DØ will also have the ability to make measurements of mixing in the neutral B-meson system and constrain the CKM matrix parameters. For example, DØ is expected to reduce the uncertainty on $\sin(2\beta)$ to $\sigma(sin(2\beta)) \sim 0.07$.

Run II of the Fermilab Tevatron presents a great opportunity for studying bottom quark physics. Perhaps precision tests of perturbative QCD made at DØ will elucidate the discrepancy between the current experimental data and theoretical predictions in the measurement of the inclusive bottom quark production cross section.

APPENDIX A

THE DØ COORDINATE SYSTEM

The DØ experiment uses a right-handed coordinate system defined with the $+z$-axis in the direction of the proton beam, the $+y$-axis perpendicular to the plane of the Tevatron ring, and the $+x$-axis in the plane of the Tevatron, pointing outward from the center of the ring. The coordinate system was designed so that $(x, y, z) = (0, 0, 0)$ is at the center of the detector.

Often more convenient coordinate systems are used. At DØ, cylindrical (r, ϕ, z) and spherical (r, ϕ, θ) coordinates can be used as well. In cylindrical coordinates, the z-coordinate remains the same, while $r = \sqrt{x^2 + y^2}$ and ϕ is the azimuthal angle so that $\phi = 0$ lies along the $+x$-axis. In spherical coordinates, $r = \sqrt{x^2 + y^2 + z^2}$, ϕ is the azimuthal angle defined above, and θ describes the polar angle, oriented so $\theta = 0$ along the direction of the proton beam ($+z$-axis) and $\theta = \pi/2$ along the $+y$-axis.

Often, instead of the polar angle, it is beneficial to use the pseudorapidity, η, defined as

$$\eta = -\ln \tan \frac{\theta}{2} \tag{A.1}$$

The pseudorapidity approximates the true rapidity, y, defined as

$$y = \frac{1}{2} \ln \frac{E + p_z}{E - p_z} \tag{A.2}$$

in the limit that the mass is vanishingly small compared to the energy ($m/E \to 0$, where m is the invariant mass $m^2 = E^2 - p^2$). Because differences in rapidity are

Lorentz-invariant quantities, pseudorapidity is often used as a substitute for the polar angle, θ.

In addition to the coordinates introduced here, transverse quantities are often used. Because the momentum of a colliding particle perpendicular (transverse) to the beam is small compared to the longitudinal momentum, we can apply conservation of momentum and energy in the transverse plane. To obtain the transverse momentum, one projects the momentum vector onto a plane perpendicular to the beam axis using the polar angle:

$$p_{\mathrm{T}} = p \sin\theta \tag{A.3}$$

In the case of jets, one often defines the 'transverse energy' of the jet. When treated as a vector, the direction of $\mathrm{E_T}$ should be taken as that of the p_{T} vector.

APPENDIX B

ERROR PROPAGATION

Understanding the errors associated with any given measurement can be the most difficult, but necessary, component of the analysis. It is often as important to know the uncertainty on a measurement as knowing the central value of the quantity being measured. This appendix begins with a brief, general introduction to uncertainties and subsequently touches on the types of error analysis involved in this analysis.

B.1 Propagation of Errors and the Covariance Matrix

The general formula for propagating errors for $f(a, b, c...)$ is given by

$$\begin{aligned}(\delta f)^2 &= \left(\frac{\partial f}{\partial a}\right)^2 (\delta a)^2 + \left(\frac{\partial f}{\partial b}\right)^2 (\delta b)^2 + \left(\frac{\partial f}{\partial c}\right)^2 (\delta c)^2 + ... \\ &+2\rho_{ab}\left(\frac{\partial f}{\partial a}\right)\left(\frac{\partial f}{\partial b}\right)\delta a\delta b + 2\rho_{ac}\left(\frac{\partial f}{\partial a}\right)\left(\frac{\partial f}{\partial c}\right)\delta a\delta c \\ &+2\rho_{bc}\left(\frac{\partial f}{\partial b}\right)\left(\frac{\partial f}{\partial c}\right)\delta b\delta c + ...,\end{aligned} \tag{B.1}$$

where δa represents the one sigma variances in the parameters and ρ_{ij} represents the correlation between parameters i and j. Figure B.1 gives a graphic description of correlation. When two parameters a and b are completely correlated $\left(\rho_{ij} = 1\right)$, a one sigma shift in the mean value of a requires a one sigma shift in the mean value of b in the *same* direction. Complete anticorrelation $\left(\rho_{ij} = -1\right)$ implies that if a changes by one sigma, b must change by one sigma in the *opposite* direction. If the variables are uncorrelated $\left(\rho_{ij} = 0\right)$, Equation B.1 simplifies significantly to

$$(\delta f)^2 = \left(\frac{\partial f}{\partial a}\right)^2 (\delta a)^2 + \left(\frac{\partial f}{\partial b}\right)^2 (\delta b)^2 + \left(\frac{\partial f}{\partial c}\right)^2 (\delta c)^2 + ... \tag{B.2}$$

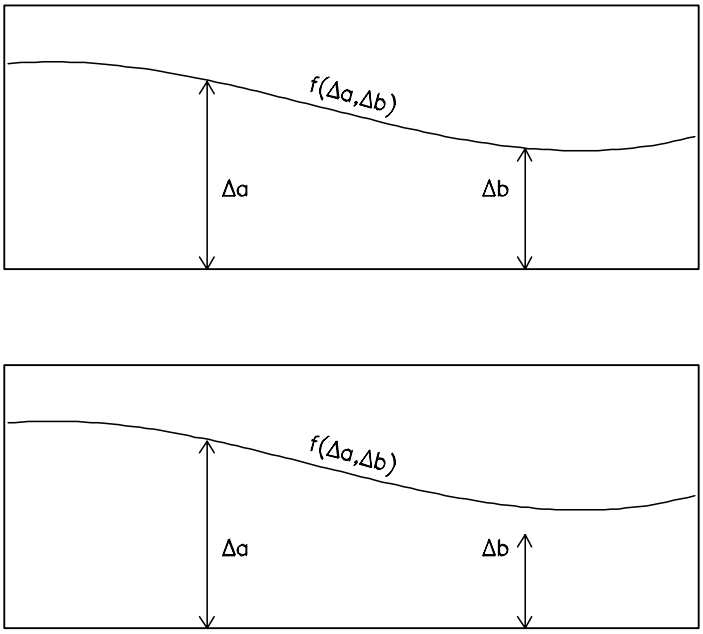

Figure B.1: Cartoon example of correlated (top) and partially correlated (bottom) variables.

Another important consequence of Equation B.1 occurs when the variances are completely correlated $(\rho_{ij} = 1)$. The generalized error expression simplifies to

$$\begin{aligned}(\delta f)^2 &= \left(\frac{\partial f}{\partial a}\right)^2 (\delta a)^2 + \left(\frac{\partial f}{\partial b}\right)^2 (\delta b)^2 + \left(\frac{\partial f}{\partial c}\right)^2 (\delta c)^2 + ... \\ &\quad +2\left(\frac{\partial f}{\partial a}\right)\left(\frac{\partial f}{\partial b}\right)\delta a\delta b + 2\left(\frac{\partial f}{\partial a}\right)\left(\frac{\partial f}{\partial c}\right)\delta a\delta c + 2\left(\frac{\partial f}{\partial b}\right)\left(\frac{\partial f}{\partial c}\right)\delta b\delta c + ...\end{aligned} \tag{B.3}$$

If a function can be expressed as a sum of terms with completely correlated errors (i. e. $f = \sum_1^N a_i$), the partial derivatives in B.1 become unity, and the error on f simplifies to

$$\begin{aligned}(\delta f)^2 &= (\delta a_1)^2 + (\delta a_2)^2 + (\delta a_3)^2 + ... + 2\delta a_1\delta a_2 + 2\delta a_1\delta a_3 + 2\delta a_2\delta a_3 + ... \\ &= (\delta a_1 + \delta a_2 + \delta a_2 + ... + \delta a_N)^2.\end{aligned} \tag{B.4}$$

Most fitting packages used in high energy physics afford the user access to the *covariance matrix*. The covariance matrix contains the information necessary to obtain the error on the function based on the fit parameter errors. The standard form of the covariance matrix for a three-parameter fit is

$$\mathrm{V} = \begin{pmatrix} c_{11} & c_{12} & c_{13} \\ c_{12} & c_{22} & c_{23} \\ c_{13} & c_{23} & c_{33} \end{pmatrix} = \begin{pmatrix} (\delta a_1)^2 & \rho_{12}\delta a_1 \delta a_2 & \rho_{13}\delta a_1 \delta a_3 \\ \rho_{12}\delta a_1 \delta a_2 & (\delta a_2)^2 & \rho_{23}\delta a_2 \delta a_3 \\ \rho_{13}\delta a_1 \delta a_3 & \rho_{23}\delta a_2 \delta a_3 & (\delta a_3)^2 \end{pmatrix}. \tag{B.5}$$

The general form of the covariance matrix can be expanded to N parameters simply. The terms along the diagonal are called the *variances*, and include the correlations ρ_{ii}, which are unity by definition. The off-diagonal elements of the covariance matrix are termed the *covariances*.

B.2 Example - Poisson Statistics and Binomial Errors

The error on a simple counting error measurement observing N events is simply $\sqrt{N}$, with a fractional error $\sqrt{N}/N$. Often, N events are each weighted by some weights w_i. In a weighted scheme, then, the central value becomes $\sum_{i=1}^{N} w_i$, and the error on that central value becomes $\sqrt{\sum_{i=1}^{N} w_i^2}$. For any quantity derived from the number of events, the fractional error must remain the same. If, for example, the number of events observed must be increased by a factor of two, the new quantity is $2N$, while the error in the quantity is $2\sqrt{N}$. In a cross section measurement, the number of events in each momentum bin must be modified by the luminosity, momentum bin width, and efficiencies (see Section 8.1).

Efficiency errors can be calculated with the prescription in Equation B.1. An

efficiency is usually thought of as some number of events a that satisfy a certain condition divided by the total number of events N. Expressed mathematically

$$\epsilon = \frac{a}{N}. \tag{B.6}$$

Here a and N are correlated variables. It is convenient to frame the problem slightly differently for error calculations.

Consider an experiment in which a events are measured and satisfy a certain condition, while b events are measured that do not. The efficiency can then be rewritten in terms of the uncorrelated variables a and b as

$$\epsilon = \frac{a}{a+b}. \tag{B.7}$$

The general error prescription for uncorrelated variables (Equation B.2) indicates that the error on ϵ is

$$(\delta\epsilon)^2 = \left(\frac{\partial\epsilon}{\partial a}\right)^2 (\delta a)^2 + \left(\frac{\partial\epsilon}{\partial b}\right)^2 (\delta b)^2 \tag{B.8}$$

where

$$\left(\frac{\partial\epsilon}{\partial a}\right) = \frac{b}{(a+b)^2}; \qquad \left(\frac{\partial\epsilon}{\partial b}\right) = -\frac{a}{(a+b)^2}. \tag{B.9}$$

Substituting yields

$$(\delta\epsilon)^2 = \frac{1}{(a+b)^4}\left(b^2(\delta a)^2 + a^2(\delta b)^2\right). \tag{B.10}$$

The errors on a and b are $\sqrt{a}$ and $\sqrt{b}$ respectively, so the expression becomes

$$\begin{aligned}(\delta\epsilon)^2 &= \frac{1}{(a+b)^4}\left(b^2 a + a^2 b\right) \\ &= \frac{ab}{(a+b)^3}.\end{aligned} \tag{B.11}$$

Using the definition of efficiency above,

$$(\delta\epsilon)^2 = \frac{\left(\frac{a}{N}\right)\left(\frac{N-a}{N}\right)}{N}$$

$$= \frac{\epsilon\,(1-\epsilon)}{N}, \tag{B.12}$$

so the error on the efficiency is given by

$$\delta\epsilon = \sqrt{\frac{\epsilon\,(1-\epsilon)}{N}}. \tag{B.13}$$

This formula for the statistical error on the efficiency is called the *binomial error formula*. The error band of the efficiency must be physical, so the band is bounded by the interval $[0, 1]$.

B.3 Hyperbolic Tangent Fit

In Section 5.3.8, to smooth out the values for the trigger efficiencies from the Monte Carlo, we employ a hyperbolic tangent of the form

$$\varepsilon_{trig} = p_1 \cdot \tanh\left(p_2 \cdot p_{\mathrm{T}}^{\mu} + p_3\right). \tag{B.14}$$

This function is fit to the Monte Carlo points using the MINUIT pacakge from within PAW. The MINUIT pacakge also supplies the covariance matrix for the fit. As an example of the use of the covariance matrix, we'll start with the expression for the total error on the fitted efficiency function:

$$\begin{aligned}(\delta\varepsilon)^2 &= \left(\frac{\partial\varepsilon}{\partial p_1}\right)^2(\delta p_1)^2 + \left(\frac{\partial\varepsilon}{\partial p_2}\right)^2(\delta p_2)^2 + \left(\frac{\partial\varepsilon}{\partial p_3}\right)^2(\delta p_3)^2 + \\ &\quad +2\left(\frac{\partial\varepsilon}{\partial p_1}\right)\left(\frac{\partial\varepsilon}{\partial p_2}\right)\rho_{p_1p_2}\delta p_1\delta p_2 + 2\left(\frac{\partial\varepsilon}{\partial p_1}\right)\left(\frac{\partial\varepsilon}{\partial p_3}\right)\rho_{p_1p_3}\delta p_1\delta p_3 \\ &\quad +2\left(\frac{\partial\varepsilon}{\partial p_2}\right)\left(\frac{\partial\varepsilon}{\partial p_3}\right)\rho_{p_2p_3}\delta p_2\delta p_3\ .\end{aligned} \tag{B.15}$$

Using the c_{ij} parametrization of the covariance matrix, one can rewrite this expression as

$$(\delta\varepsilon)^2 = \left(\frac{\partial\varepsilon}{\partial p_1}\right)^2 c_{11} + \left(\frac{\partial\varepsilon}{\partial p_2}\right)^2 c_{22} + \left(\frac{\partial\varepsilon}{\partial p_3}\right)^2 c_{33} +$$

$$+2\left(\frac{\partial\varepsilon}{\partial p_1}\right)\left(\frac{\partial\varepsilon}{\partial p_2}\right)c_{12}+2\left(\frac{\partial\varepsilon}{\partial p_1}\right)\left(\frac{\partial\varepsilon}{\partial p_3}\right)c_{13} \tag{B.16}$$
$$+2\left(\frac{\partial\varepsilon}{\partial p_2}\right)\left(\frac{\partial\varepsilon}{\partial p_3}\right)c_{23}\ .$$

From Equation B.14 and the identity

$$\frac{\partial}{\partial x}\tanh(u)=\frac{\partial u}{\partial x}\left(\frac{1}{\cosh^2(u)}\right), \tag{B.17}$$

one can derive

$$\frac{\partial\varepsilon}{\partial p_1} = \tanh\left(p_2\cdot p_{\mathrm{T}}^{\mu}+p_3\right) \tag{B.18}$$
$$\frac{\partial\varepsilon}{\partial p_2} = \frac{p_1\cdot p_{\mathrm{T}}^{\upsilon}}{\cosh^2\left(p_2\cdot p_{\mathrm{T}}^{\mu}+p_3\right)} \tag{B.19}$$
$$\frac{\partial\varepsilon}{\partial p_3} = \frac{p_1}{\cosh^2\left(p_2\cdot p_{\mathrm{T}}^{\mu}+p_3\right)}. \tag{B.20}$$

The substitution into B.15 to obtain an expression for $\delta\varepsilon$ as a function of p_{T}^{μ} is left as a nasty algebraic nightmare for the reader. The dashed curves on Figure 5.7 represent $\varepsilon\pm\delta\varepsilon$ as a function of p_{T}^{μ}.

B.4 Weighted Average Calculation

For the associated jet correction in the data selection chapter, we use a weighted average of three ISAJET samples. The weighted average is designed to give more weight to more statistically significant samples. To compute the weighted average, we use the following for each muon transverse momentum bin:

$$x = \frac{\sum\left(\frac{1}{\sigma_{x_i}}\right)^2\cdot x_i}{\sum\left(\frac{1}{\sigma_{x_i}}\right)^2} \tag{B.21}$$

$$\sigma_x = \sqrt{\frac{1}{\sum \left(\frac{1}{\sigma_{x_i}}\right)^2}}, \tag{B.22}$$

where x_i and σ_i refer to the associated jet correction and the statistical error on the associated jet correction from Monte Carlo sample i.

B.5 Maximum Likelihood Calculation

The output of the maximum likelihood fit (Section 6.2.1) is a single parameter, p_1, and its associated uncertainty. The obtain the weight for each event, the variables p_{T}^{μ} and p_{T}^{rel} are read in, and the weight is calculated to be

$$w_b = \frac{p_1 \cdot \rho_b \left(p_{\mathrm{T}}^{rel}, p_{\mathrm{T}}^{\mu}\right)}{p_1 \cdot \rho_b \left(p_{\mathrm{T}}^{rel}, p_{\mathrm{T}}^{\mu}\right) + (1 - p_1) \cdot \rho_c \left(p_{\mathrm{T}}^{rel}, p_{\mathrm{T}}^{\mu}\right)}, \tag{B.23}$$

where ρ_b is the normalized probability distribution for bottom quarks and ρ_c is the distribution for background. Using the prescription outlined in the early sections of this chapter, one finds

$$\delta w_b^2 = \left(\frac{\rho_b \cdot \rho_c}{\left(p_1 \cdot (\rho_b - \rho_c) + \rho_c\right)^2}\right)^2 \delta p_1^2. \tag{B.24}$$

To obtain f_b for a single muon transverse momentum bin, the weights of all events are summed and divided by the total number of events:

$$f_b = \frac{\sum w_b}{N}. \tag{B.25}$$

Because the uncertainty on a single events depends linearly on the error on the MINUIT parameter, the error on all the event weights are nearly completely correlated. From expression B.4, then, the error on f_b is given by

$$\delta f_b^2 = \left(\frac{\sum w_b}{N}\right)^2. \tag{B.26}$$

APPENDIX C

CODE DESCRIPTION

In the course of an analysis such as the one described in this dissertation, a lot of code is generated that is not necessary for the meat of the analysis. This code can originate from failed side tests, dead ends, parallel ideas with various subsets of the data, etc. This Appendix is designed to indicate to the deeply interested reader the location and bits of code used in each step of this analysis. This list should be used with caution however, as it is not exhaustive. Only the main pieces of code are listed.

The information is all contained on d0chb.fnal.gov on the /projects/764 disk. Because much of the code was copied directly from VMS during the DØ migration to unix, a great deal of the code still references files in the VMS format. All directories here are listed in unix format. Any references to the directory structure below TMP$ROOT201:[DAVIS.LNR] in the VMS filename convention map identically to that below ~kpdavis/lnr/lnr/, so filename translation is simple.

C.1 Data Selection

Before any measurement can be made, data must be selected. The data is selected by FORTRAN routines and written to a text output file that is used by the maximum likelihood code and the code that creates the b-produced muon vectors. The code can be found in ~kpdavis/lnr/lnr/nt_read/data/.

C.2 Efficiencies

To obtain the efficiencies in Chapter 5, a PAW kumac loops over a FORTRAN selection function to fill histograms. The kumac then takes a ratio of the histograms to obtain an efficiency. Many of the routines producing the plots in chapter are in the directories listed below.

- Trigger Efficiency - ~kpdavis/lnr/lnr/effic/reco/ contains not only the code to obtain the trigger efficieny, but also the function used to fit the MC points.

- Reconstruction Efficiency - ~kpdavis/lnr/lnr/effic/reco/ contains the routines needed to obtain the reconstruction efficiency

- Associated Jet Cut Efficiency - ~kpdavis/lnr/lnr/effic/ajet/ contains associated jet cut efficiency routines, including the kumac that obtains the weighted average of three MC samples.

- Quality Cut Efficiency - ~kpdavis/lnr/lnr/effic/other/ contains the relevant routines.

C.3 Cosmic Background Estimation

The cosmic ray muon background is estimated using a PAW kumac. The kumac calls a selection function to fill scintillator time of flight histograms. The cosmic fraction is fit within PAW and the resulting functions are written to a FORTRAN routine. The code for the cosmic background estimation is given in ~kpdavis/lnr/lnr/cos_rej/.

C.4 Maximum Likelihood Code

The maximum likelihood fit is an integral, but complicated, component of this analysis. Its subcomponents, each of which may be fairly sophisticated, are located in a number of places. For each major subcomponent, the main working directory is listed. Many of the components are simple FORTRAN, but some involve running PAW kumacs between running pieces of code.

C.4.1 Obtaining the Sequential/Direct Ratio

To begin with, the ratio of sequential to direct decays is obtained. The code for obtaining this ratio is given in ~kpdavis/lnr/lnr/bfrac/corr/.

C.4.2 Creating p_{T}^{rel} Fits

The p_{T}^{rel} fits are created mainly by hand, but the kumac that creates the histograms to be fitted and obtains normalizations of functions once the fit is performed is located in ~kpdavis/lnr/lnr/ptrel_fits/onebin/mc/.

C.4.3 The Maximum Likelihood Fit

Once the probability functions are obtained, they are normalized and put in the directory ~kpdavis/lnr/lnr/ptrel_fits/functions/3dfmc/. The maximum likelihood code, found in ~/kpdavis/lnr/lnr/max_like/3dfd/ uses these functions as input distributions.

C.4.4 Viewing Maximum Likelihood Fit Results

The kumac used to view the quality of the fit obtained in the maximum likelihood code is given in ~kpdavis/lnr/lnr/kumacs/contrib_ptrel/.

C.4.5 Obtaining the *b*-fraction

The code that takes the results of the maximum likelihood fit and transforms it into usable vectors contained in ~kpdavis/lnr/lnr/make_hists/3dfd/.

C.4.6 Cross-checking the *b*-fraction

The kumac that compares the *b*-fraction obtained in the data to that found in the MC is contained in the directory ~kpdavis/lnr/lnr/bfrac/3dfd/.

C.5 Unsmearing

The Bayesian unsmearing is another notable feature of the analysis. The code that prepares the smearing matrix is located in ~kpdavis/lnr/lnr/unfold2/, and the code that actually performs the unsmearing is located in the same directory.

C.5.1 Results of the Unsmearing

The kumac located in ~kpdavis/lnr/lnr/plot_mupt/ plots the results of the unsmearing. This kumac also calculates the unsmearing factor used in the cross section calculations.

C.5.2 Unsmearing Uncertainties

The uncertainties associated with the unsmearing of the muon transverse momentum spectrum are obtained by running the code in ~kpdavis/lnr/lnr/unfold2/ under slightly different conditions. The vectors are save and combined with the kumac in ~kpdavis/lnr/lnr/unfold/.

C.6 Cross Sections

The cross section measurements in Chapter 8 are created by pulling vectors in from many different directories and combining them with the plot_mu_incl.kumac in the directory ~kpdavis/lnr/lnr/kumacs/muon_cross/.

C.7 Other Code

Many of the theoretical plots and illustrative cartoons used in this thesis are created by kumacs in the directory ~kpdavis/lnr/lnr/kumacs/random/.

REFERENCES

[1] S. Abachi, *et al.* (DØ Collaboration), Phys. Rev. Lett. **74**, 3548 (1995).

[2] S. Abachi, *et al.* (DØ Collaboration), Phys. Lett. B **370**, 239 (1996).

[3] F. Abe, *et al.* (CDF Collaboration), Phys. Rev. Lett. **71**, 2396 (1993).

[4] F. Abe, *et al.* (CDF Collaboration), Phys. Rev. Lett. **53**, 1051 (1996).

[5] C. Albajar, *et al.* (UA1 Collaboration), Z. Phys. **61**, 41 (1994).

[6] M. Gell-Mann, Phys. Lett. **8**, 214 (1964).

[7] J. C. Street and E. C. Stevenson, Phys. Rev. **52**, 1003 (1937).

[8] M. L. Perl *et al.*, Phys. Rev. Lett. **35**, 1489 (1975).

[9] E. Fermi, Zeit. Phys. **88**, 161 (1934).

[10] The Super-Kamiokande Collaboration, Phys. Rev. Lett. **81,** 1562 (1998).

[11] S. Abachi *et al.* (DØ Collaboration), Phys. Rev. Lett. **74**, 2632 (1995).

[12] F. Abe *et al.* (CDF Collaboration), Phys. Rev. Lett. **74**, 2626 (1995).

[13] F. Halzen, A. Martin, *Quarks & Leptons*, Wiley (1984).

[14] P. W. Higgs, Phys. Lett. **12**, 132 (1964).

[15] M. Mangano, P. Nason, and G. Ridolfi, Nucl. Phys. **B 373** 295 (1992).

[16] W. A. Bardeen, *et al.*, Phys. Rev. D **18**, 3998 (1978).

[17] P. Nason, S. Dawson, and R. K. Ellis, Nucl. Phys. **B327**, 49 (1989).

[18] P. Nason, S. Dawson, and R. K. Ellis, Nucl. Phys. **B303**, 607 (1988).

[19] F. Paige and S. Protopopescu, Fermilab Computing Division **PM0059** (1992).

[20] E. James, Ph.D. Thesis, University of Arizona, (1995).

[21] G. Fox and S. Wolfram, Nucl. Phys. **B 168** 285 (1980).

[22] R. D. Field and R. P. Feynman, Nucl. Phys. **B 136** 1 (1978).

[23] C. Peterson *et al.* Phys. Rev. D **27**, 105 (1986).

[24] S. Squarcia, CERN **PPE/94-69** (1994).

[25] F. Stichelbaut, DØ Internal Note 3633.

[26] S. Abachi *et al.* (DØ Collaboration), Phys.Rev.Lett. **77**, 3309 (1996).

[27] J. Thompson, DØ Internal Note **2367** (1994).

[28] B. Webber, Fermi National Accelerator Operations Bulletin **719** (1979).

[29] S. Abachi *et al.* (DØ Collaboration), Nucl. Instr. Meth. **A 338**, 185 (1994).

[30] A. R. Clark *et al.*, Nucl. Instr. Meth. **A 315**, 193 (1992).

[31] NiCoTin is an alloy of 38.8% Co, 19.3% Cr, 15.6% Ni, 13.3% Fe, and 11.4% Mo.

[32] J. Kadyk, Nucl. Instr. Meth. **A 300**, 436 (1991).

[33] V. L. Ginzberg and I. M. Frank, JETP **16**, 15 (1946).

[34] "Etude d'un Detecteur a Rayonnement de Transition pour l'Experience DØ au FNAL," Fabrice Feinstein, Ph. D. Thesis, A l'Universite de Paris-Sud, Centre d'Orsay, December 1987 (unpublished).

[35] Thomas Ferbel, *Experimental Techniques in High Energy Physics*, Addison Wesley (1987), p. 391.

[36] A. R. Clark *et al.*, Nucl Instr. Meth. A **279**, 243 (1989).

[37] R. Avery *et al.*, "Results from a Beam Test of the DØ Forward Drift Chamber," IEEE Trans. Nucl. Science (1992).

[38] D. Hedin, DØ Internal Note **1738** (1993).

[39] N. Grossman, DØ Internal Note **1527** (1992).

[40] Bicron Corporation, 12345 Kinsman Road, Newbury, OH 44065-9677

[41] T. Marshall and H. Haggerty, DØ Internal Note **2556** (1995).

[42] R. Astur, DØ Internal Note **1662** (1993).

[43] T. Sjostrand, Computer Physics Commun. **82** (1994) 74.

[44] D. Fein, University of Arizona, private communication.

[45] F. Stichelbaut, DØ Internal Note **3632** (1992).

[46] D. Fein, Ph. D. Thesis, University of Arizona, (1995).

[47] A. Maciel, Northern Illinois University, private communication.

[48] R.M. Barnett, *et al.*, Particle Physics Booklet **200** (1996).

[49] D. Vititoe, Ph. D. Thesis, University of Arizona, (1996).

[50] C. Gerber *et al.*, DØ Internal Note **2140** (1994).

[51] G. D'Agostini, DESY **94-099** (1994).

[52] J. Krane, J. Bantly, D. Owen, Fermilab Technical Memorandum 2000, 1997.

[53] J. Krane, Ph. D. Thesis, University of Nebraska, 1998.

[54] C. Albajar, *et al.* (UA1 Collaboration), Phys. Lett. **B256**, 121 (1991).

[55] http://www-cdf.fnal.gov/physics/new/bottom/cdf3694/cdf3694.html

[56] M. Mangano, "Two Lectures on Heavy Quark Production in Hadronic Collisions", CERN-TH/97-328, 1997.

[57] S. Abachi, *et al.* (DØ Collaboration), "Small angle muon and b quark production at sqrt(s) = 1.8 TeV", hep-ex/9907029, submitted to PRL.

[58] http://www-d0.fnal.gov/~mostafa/solenoid/

[59] F. Abe, *et al.* (CDF Collaboration), Phys. Rev. D **58**, 112004 (1998).